



ulm university universität
uulm



Annual Report 2016

Institute of Optoelectronics

Cover photo:

The photo shows a setup for measuring the chemical sensing function of a GaN/GaN heterostructure. Here, green laser light was used, whereas in real experiments, an invisible ultraviolet laser excites the photoluminescence of the sensor structure mounted on the metal block at the left side. The excitation light and the sensor photoluminescence light are separated by a dichroic mirror in the center. See the related articles on pages.

Contents

Staff	II
Preface	1
Articles	
VCSEL With Thermally Induced Birefringence	3
Parallel-Driven VCSELs With Optically Controlled Current Confinement	9
Optical Modes in VCSELs	15
Background Doping in Semipolar GaN	23
Functionalization of GaN Surfaces for Biosensing	29
Optimizing InGaN Heterostructures for High Biosensitivity	37
Gas Sensing Using InGaN QWs	45
AlGaN/AlN Heterostructures	51
Investigation of AlBN Grown by MOVPE	59
Intra-Cavity Frequency Tripling of OPSDLs	67
Lists of Publications	
Ph.D. Thesis	75
Master Theses	76
Bachelor Theses	77
Talks and Conference Contributions	78
Publications	81





- | | | |
|---------------------|-----------------------------|-------------------------|
| 1: Hildegard Mack | 2: Oliver Rettig | 3: Rainer Blood |
| 4: Ferdinand Scholz | 5: Vignesh Devaki Murugesan | 6: Karl Joachim Ebeling |
| 7: Thomas Zwosta | 8: Markus Polanik | 9: Martin Schneidereit |
| 10: Sven Bader | 11: Tobias Pusch | 12: Rainer Michalzik |
| 13: Susanne Menzel | 14: Jürgen Mähniß | 15: Markéta Zíková |
| 16: Peter Unger | 17: Rudolf Rösch | 18: Jassim Bin Shahbaz |

Not on the photo:

Markus Daubenschütz, Sükran Kilic, Irene Lamparter, Eva Nüßle, Ilona Schwaiger

Ulm University Institute of Optoelectronics

Albert-Einstein-Allee 45, 89081 Ulm, Germany
 URL: <http://www.uni-ulm.de/opto>
 Fax: +49-731/50-260 49
 Phone: +49-731/50-

Head of Institute

Prof. Dr. Karl Joachim Ebeling -2 60 51 karljoachim.ebeling@uni-ulm.de

Deputy Heads

Prof. Dr. Ferdinand Scholz -2 60 52 ferdinand.scholz@uni-ulm.de

Prof. Dr. Peter Unger -2 60 54 peter.unger@uni-ulm.de

Group Leader

apl. Prof. Dr.-Ing. Rainer Michalzik -2 60 48 rainer.michalzik@uni-ulm.de

Cleanroom Management

Dr.-Ing. Jürgen Mähnbß -2 60 53 juergen.maehnss@uni-ulm.de

Secretaries

Sükran Kilic -2 60 59 suekran.kilic@uni-ulm.de

Hildegard Mack -2 60 60 hildegard.mack@uni-ulm.de

Eva Nüßle -2 60 50 eva.nuessle@uni-ulm.de

Visiting Scientist

Dr. Markéta Zíková -2 60 36 zikova@fzu.cz

Research Staff

M. Sc. Sven Bader -2 60 37 sven.bader@uni-ulm.de

Dipl.-Ing. Marian Caliebe* -2 60 39 marian.caliebe@uni-ulm.de

M. Sc. Markus Daubenschütz -2 60 38 markus.daubenschueuz@uni-ulm.de

M. Sc. Vignesh Devaki Murugesan -2 60 38 vignesh.devaki@uni-ulm.de

Dipl.-Phys. Dominik Heinz* -2 60 39 dominik.heinz@uni-ulm.de

M. Sc. Markus Polanik -2 60 46 markus.polanik@uni-ulm.de

M. Sc. Tobias Pusch -2 60 37 tobias.pusch@uni-ulm.de

M. Sc. Oliver Rettig -2 60 36 oliver.rettig@uni-ulm.de

M. Sc. Martin Schneidereit -2 60 39 martin.schneidereit@uni-ulm.de

M. Sc. Jassim Bin Shahbaz -2 60 39 jassim.shahbaz@uni-ulm.de

Technical Staff

Rainer Blood -2 60 44 rainer.blood@uni-ulm.de

Gerlinde Meixner* -2 60 41 gerlinde.meixner@uni-ulm.de

Irene Lamparter -2 60 57 irene.lamparter@uni-ulm.de

Susanne Menzel -2 60 41 susanne.menzel@uni-ulm.de

Rudolf Rösch -2 60 57 rudolf.roesch@uni-ulm.de

Ilona Schwaiger⁺ -2 60 36 ilona.schwaiger@uni-ulm.de

Thomas Zwosta -2 60 36 thomas.zwosta@uni-ulm.de

* Is an alumnus of the Institute meanwhile

⁺ Currently on parental leave

Preface

During 2016, the Institute of Optoelectronics continued its successful research in the fields of vertical-cavity surface-emitting lasers (VCSELs), GaN-based optoelectronics, and semiconductor disk lasers.

The VCSELs and Optical Interconnects Group has been prolific in the electro-thermal and optical modeling of VCSELs and the fabrication and analysis of novel VCSEL structures. Optically controlled current confinement has been accomplished with integrated photo-transistors and a new world record of 45 GHz was established for the reversible thermal tuning range of the birefringence splitting in single-mode VCSELs. On July 1st, results from VCSEL research were presented to distinguished guests during a boat trip with MS Sonnenkönigin on Lake Constance as part of the 66th Lindau Nobel Laureate Meeting. In late September, the *Highlights of Physics* event sponsored by the Federal Ministry of Education and Research (BMBF) and the German Physical Society (DPG) took place in Ulm and attracted more than 60.000 visitors. For five days the VCSEL Group hosted a very-well-received exhibition booth on “Microlasers in everyday life” next to majestic Ulm Minster.

In 2016, the sensor activities in the GaN group have been strengthened by two new Ph.D. students. One of them participates in our DFG-funded inter-faculty Graduate School “PulmoSense” (Micro- and Nano-Scale Sensors for the Lung) involving groups from engineering, physics, chemistry, and medicine of Ulm University. Our studies towards AlGaIn-based heterostructures for deep-UV LEDs have been successfully continued. First boron-containing AlGaIn layers have been grown which may help to reduce strain-related problems in such devices. These activities have been assisted by Tomáš Hubáček, a guest scientist from the Czech Academy of Science, who joined our Institute for about 6 months.

In the High-Power Semiconductor Laser Group, 23 mW of ultraviolet laser emission at a wavelength of 327 nm has been achieved in a semiconductor disk laser system using a sum frequency mixing of the fundamental wavelength of 982 nm and the frequency-doubled second-harmonic radiation at 491 nm.

A snapshot of several Ph.D. students of our Institute working in the cleanroom was selected for the title page of the Annual Report of Ulm University 2015 (DOI 10.18725/OPARU-4188) that was published in Oct. 2016. Finally we are very happy to welcome Irene Lamparter in our team of technicians, who is reviving the much-needed mechanical workshop of the Institute.

Karl Joachim Ebeling
Rainer Michalzik
Ferdinand Scholz
Peter Unger

Ulm, March 2017

Vertical-Cavity Surface-Emitting Laser With Thermally Induced Birefringence

Tobias Pusch and Eros La Tona

Birefringent vertical-cavity surface-emitting lasers offer a new opportunity to generate high polarization modulation dynamics. By inducing spin-polarized carriers, the device can be excited to oscillations in the degree of circular polarization with an oscillation frequency nearly equal to the birefringence splitting. A mechanism for frequency tuning of the oscillations directly integrated on the chip is desirable for future applications. With asymmetric heating we demonstrate a reversible tuning of the birefringence splitting of 45 GHz with a decrease of the laser output power of less than 3 dB.

1. Introduction

Vertical-cavity surface-emitting lasers (VCSELs) are used extensively today for optical sensing and data transmission [1]. While most sensing applications impose only very moderate requirements on the device dynamics, VCSELs in data transmission systems are optimized for high bandwidth. Digital data transmission at a data rate of 50 Gb/s using a bit pattern generator [2] and at 71 Gb/s with a dedicated electronic driver chip employing transmitter equalization [3] have been published. Recently as much as 150 Gb/s were generated with a commercial 850 nm wavelength VCSEL with 23 GHz bandwidth that was modulated with a spectrally efficient 13-level signal (modified duobinary 4-level pulse amplitude modulation). Offline digital signal processing was required to determine bit error ratios [4]. To reduce the system complexity and increase the energy efficiency, laser devices with substantially higher bandwidth are needed for future optical interconnects with data rates exceeding 100 Gb/s. The polarization dynamics in VCSELs offers benefits to overcome the limitations of intensity modulation. Here the birefringence splitting, namely the frequency difference between the two linearly polarized modes, plays an important role. By injection of spin-polarized carriers into a birefringent VCSEL, an oscillation in the degree of circular polarization can be generated, while the average emitted power remains constant [5]. This oscillation can be switched off in an extremely short time interval [6]. Fast polarization oscillations based on induced spin were shown [7]. The oscillation frequency is nearly equal to the birefringence splitting. A measured birefringence splitting of more than 250 GHz shows the potential of this approach [8].

2. New VCSEL Concept for Asymmetric Heating

A high birefringence splitting in VCSELs can be obtained using the elasto-optic effect. External strain can induce a lattice anisotropy which results in an anisotropic change of

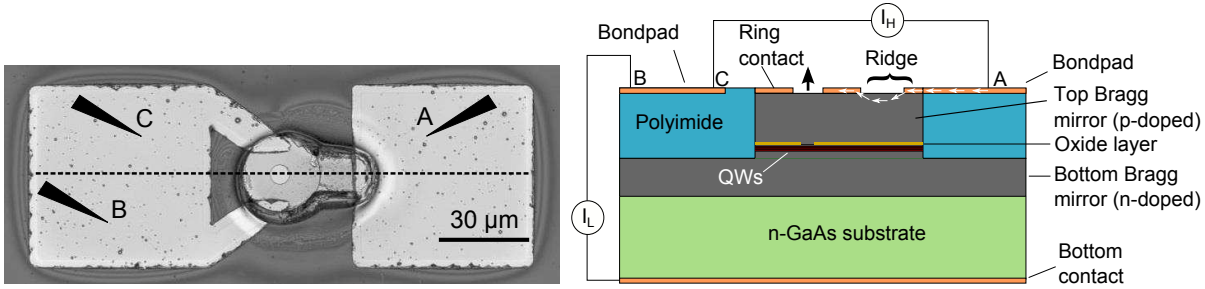


Fig. 1: Photograph of a fabricated device (left). Cross-section of the VCSEL structure along the dotted line on the left with the two electrical circuits (right). The path of the heating current is partly indicated with white arrows. A, B, and C mark the contact points of the probe needles.

the refractive index. With this approach Panajotov et al. [9] reported a birefringence splitting of 80 GHz in a VCSEL packaged in a TO-can. Direct mechanical bending of a VCSEL array has resulted in the present record of $B = 259$ GHz birefringence splitting [8]. For mechanically induced strain, a custom-made bending device is needed. This limits the miniaturization of the laser sub-system as well as later commercial applicability. Alternatively the birefringence splitting can be induced thermally. Jansen van Doorn et al. [10, 11] used a 770 nm Ti:sapphire laser to generate a hotspot approximately $30 \mu\text{m}$ next to the emission window of an 850 nm VCSEL. With a laser output power of 27 mW a reversible birefringence tuning of $B < 3$ GHz was measured [10] and a much higher power of 200 mW led to a change of the birefringence to $B = 23$ GHz accompanied by surface damage [11], which is unacceptable for practical use. After the heating power was shut off, a few percent of the birefringence change reached by exposure remained [11].

The approach reported in this article is based on the same idea of asymmetric heating. However, we replace the external optical power source by an integrated electrical heater. Such a one-chip device combines very small size, ease of handling, and fine-tuning capability of the birefringence splitting. A top view of the fabricated VCSEL structure and a schematic cross-section are shown in Fig. 1. Wafer material for standard oxide-confined AlGaAs-based 850 nm VCSELs was used, which was grown on a n-doped (001)-oriented GaAs substrate by Philips Technologie GmbH, U-L-M Photonics. It consists of a p-i-n structure with 23 top Bragg mirror pairs in the p-region and 37.5 bottom mirror pairs in the n-region. The inner one-wavelength-thick cavity has three GaAs quantum wells (QWs). An adjacent 30 nm thick AlGaAs layer in the p-region serves for current confinement after mesa etching and wet-thermal oxidation. In contrast to conventional VCSELs the mesa is not circular but resembles the shape of a keyhole. The orientation is along the $[110]$ or $[\bar{1}10]$ crystal axis, which are the preferred orthogonal polarization directions of standard GaAs VCSELs [1]. The etching with a depth of $4.8 \mu\text{m}$ extends well into the n-region. The VCSEL mesa has a diameter of $26 \mu\text{m}$ and the connected ridge has a length and width of $16 \mu\text{m}$ and $12 \mu\text{m}$, respectively. The oxidation step produces a fully oxidized ridge and an aperture of $4\text{--}5 \mu\text{m}$ diameter for transverse single-mode emission of the laser. The top p-ring contact on the mesa made of TiPtAu has an opening of $8 \mu\text{m}$. The bottom contact metalization is GeAuNiAu. The two bondpads in Fig. 1 are placed on polyimide which is necessary for electrical insulation and planarization. They are connected to the

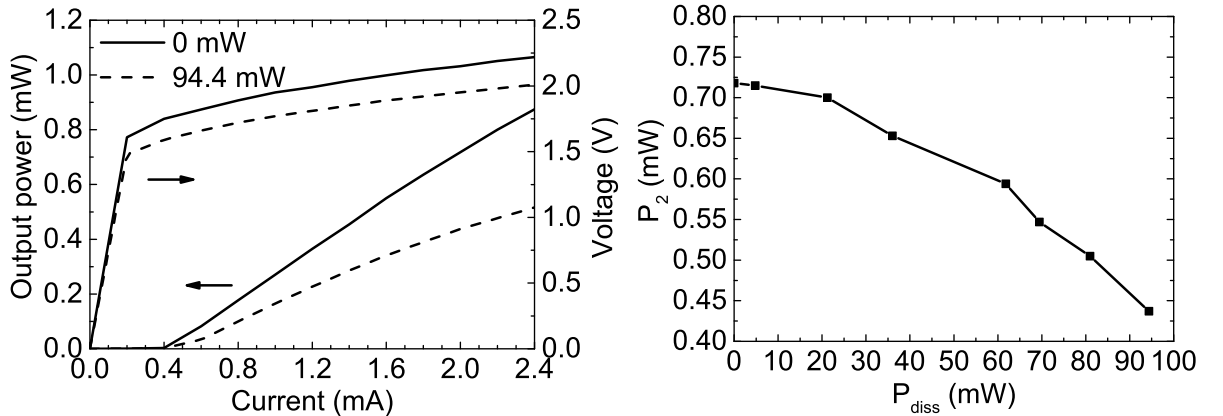


Fig. 2: LIV curves of the VCSEL at 0 mW and 94.4 mW heating power (left). Laser output power $P_2 = P(I_L = 2 \text{ mA})$ versus dissipated power $P_{\text{diss}} = I_H \cdot V_H$ in the heater (right).

p-ring contact on one side and a short contact metalization (not covering the entire ridge, see Fig. 1(right)) at the edge of the ridge on the other side. Two electrical circuits provide a high heating current I_H and a low VCSEL operating current I_L simultaneously. As sketched in Fig. 1(right) the heating current flows from the right bondpad through the ridge to the VCSEL ring contact and the left bondpad. The metalization gap forces the current to enter the semiconductor ridge material with much reduced conductivity. This is where the majority of heat generation takes place. The positions of the contact needles are marked with A and C in Fig. 1. The fully oxidized ridge area is necessary to prevent current flow through the ridge to the bottom contact. The second current path through the VCSEL aperture to the bottom contact (contact point B) is used for laser operation.

3. Measurement Results

The measured light-current-voltage (LIV) characteristics for VCSEL operation without heating are shown in Fig. 2(left). The threshold current is $I_{\text{th}} = 0.42 \text{ mA}$ at a voltage of $V_{\text{th}} = 1.76 \text{ V}$. The slope efficiency is 0.46 W/A , corresponding to a differential quantum efficiency of 31%. Figure 3 depicts the optical spectrum of the unheated VCSEL at a current of $I_L = 2.3 \text{ mA}$. It has two peaks at wavelengths of 848.00 nm and 848.04 nm. These are the orthogonal polarization states of the fundamental mode. Actually the spectrum was measured with a polarizer suppressing the longer-wavelength mode by about 28 dB. Otherwise, caused by the resolution of the optical spectrum analyzer of 0.015 nm, only this peak would be visible and the initial birefringence splitting couldn't be determined. The observed wavelength difference $\Delta\lambda = 0.04 \text{ nm}$ of the polarization modes corresponds to a birefringence splitting $B = \Delta\nu = c\Delta\lambda/\lambda^2 = 17 \text{ GHz}$, where c is the vacuum velocity of light. The next-order transverse mode at $\lambda \approx 847 \text{ nm}$ is not seen in the spectrum. The side-mode suppression ratio of the VCSEL (without polarizer) is about 26 dB at the given operating point.

In what follows the device is characterized for different amounts of heating up to a current $I_H = 33 \text{ mA}$. This maximum value is chosen in order to prevent contact damage. Figure

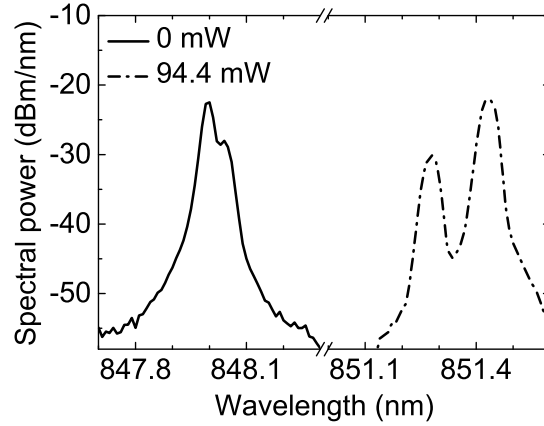


Fig. 3: Measured optical spectra without heating and for $P_{\text{diss}} = 94.4 \text{ mW}$. A polarizer has suppressed the long-wavelength peak at 848.04 nm and the short-wavelength peak at 851.28 nm. The laser current is $I_L = 2.3 \text{ mA}$.

2(left) shows the LIV curves for the peak dissipated power $\hat{P}_{\text{diss}} = \hat{I}_H \cdot \hat{V}_H = 33 \text{ mA} \cdot 2.86 \text{ V} = 94.4 \text{ mW}$. The purpose of heating is the creation of anisotropic strain in the laser cavity by means of the elasto-optic effect. While doing so, the laser necessarily experiences a parasitic temperature increase, which is known to decrease both the achievable output power and the operating voltage [1]. In the given device the slope efficiency decreases from 0.46 W/A at $I_H = 0$ to 0.30 W/A at $I_H = 33 \text{ mA}$. The effect of the dissipated power P_{diss} on the output power at a laser current of $I_L = 2 \text{ mA}$ is displayed in Fig. 2(right). The decrease from initially 0.72 mW to 0.44 mW for maximum heating amounts to less than 40% and is thus well acceptable. Most importantly the birefringence splitting of the fundamental mode in the optical spectrum in Fig. 3 has become much larger. The measured wavelength difference of $\Delta\lambda = 0.15 \text{ nm}$ corresponds to $B = 62 \text{ GHz}$ and thus the VCSEL can be tuned by as much as $\Delta B = (62 - 17) \text{ GHz} = 45 \text{ GHz}$. The spectrum of the heated device in Fig. 3 was measured with the polarizer rotated by 90° versus the case $I_H = 0$. Obviously now the short-wavelength polarization mode at $\lambda = 851.28 \text{ nm}$ dominates. The underlying polarization switch was found to occur at $I_H \approx 30 \text{ mA}$. Figure 4 plots the birefringence splitting as a function of the dissipated power. There is a continuous increase of B with increasing P_{diss} with an apparent change of the slope around $P_{\text{diss}} = 60 \text{ mW}$, which is in the vicinity of the polarization switching point.

4. Conclusion

In summary we have presented a novel VCSEL device with electrical tunability of the birefringence splitting via asymmetric heating. A record-high thermally induced tuning range of 45 GHz was shown at a moderate reduction of the laser output power. Even higher values should be achievable with a more robust contact design allowing higher heating currents. Fully reversible behavior without a remanent birefringence change was observed. The detailed birefringence tuning behavior close to a polarization switching point is a topic for further studies. The integrated heating approach can be combined with

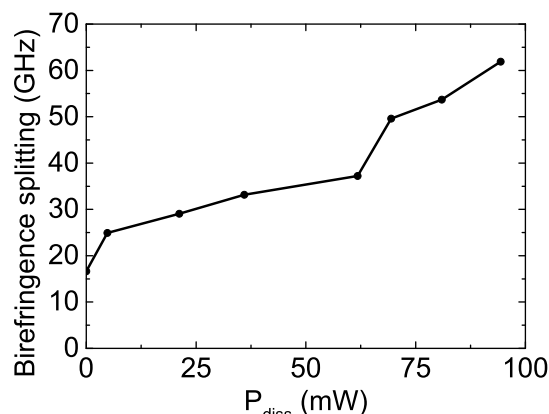


Fig. 4: Birefringence splitting of the VCSEL versus dissipated power of the integrated heater.

mechanical or piezoelectric birefringence generation to obtain high polarization oscillation frequencies with fine and wide-range tuning capability.

5. Acknowledgment

The authors thank Dr. Philipp Gerlach from Philips Technologie GmbH, U-L-M Photonics for fruitful discussions about the VCSEL design. This work has been supported by the German Research Foundation (DFG) grant “Ultrafast Spin Lasers for Modulation Frequencies in the 100 GHz Range”.

References

- [1] R. Michalzik (Ed.), *VCSELs — Fundamentals, Technology and Applications of Vertical-Cavity Surface-Emitting Lasers*, Springer Series in Optical Sciences, vol. 166, Berlin: Springer-Verlag, 2013.
- [2] P. Moser, J.A. Lott, P. Wolf, G. Larisch, H. Li, and D. Bimberg, “Error-free 46 Gbit/s operation of oxide-confined 980 nm VCSELs at 85°C”, *Electron. Lett.*, vol. 50, pp. 1369–1371, 2014.
- [3] D.M. Kuchta, A.V. Rylyakov, F.E. Doany, C.L. Schow, J.E. Proesel, C.W. Baks, P. Westbergh, J.S. Gustavsson, and A. Larsson, “A 71-Gb/s NRZ modulated 850-nm VCSEL-based optical link”, *IEEE Photon. Technol. Lett.*, vol. 27, pp. 577–580, 2015.
- [4] T. Zuo, L. Zhang, J. Zhou, Q. Zhang, E. Zhou, and G.N. Liu, “Single lane 150-Gb/s, 100-Gb/s and 70-Gb/s 4-PAM transmission over 100-m, 300-m and 500-m MMF using 25-G class 850nm VCSEL”, in *Proc. Europ. Conf. on Opt. Commun., ECOC 2016*, pp. 974–976. Düsseldorf, Germany, Sep. 2016.
- [5] N.C. Gerhardt, M.Y. Li, H. Jähme, H. Höpfner, T. Ackemann, and M.R. Hofmann, “Ultrafast spin-induced polarization oscillations with tunable lifetime in vertical-cavity surface-emitting lasers”, *Appl. Phys. Lett.*, vol. 99, pp. 151107-1–3, 2011.

- [6] H. Höpfner, M. Lindemann, N.C. Gerhardt, and M.R. Hofmann, “Controlled switching of ultrafast circular polarization oscillations in spin-polarized vertical-cavity surface-emitting lasers”, *Appl. Phys. Lett.*, vol. 104, pp. 022409-1–4, 2014.
- [7] K. Panajotov, B. Nagler, G. Verschaffelt, A. Georgievski, H. Thienpont, J. Danckaert, and I. Veretennicoff, “Impact of in-plane anisotropic strain on the polarization behavior of vertical-cavity surface-emitting lasers”, *Appl. Phys. Lett.*, vol. 77, pp. 1590–1592, 2000.
- [8] M. Lindemann, T. Pusch, R. Michalzik, N.C. Gerhardt, and M.R. Hofmann, “Frequency tuning of polarization oscillations: toward high-speed spin-lasers”, *Appl. Phys. Lett.*, vol. 108, pp. 042404-1–4, 2016.
- [9] T. Pusch, M. Lindemann, N.C. Gerhardt, M.R. Hofmann, and R. Michalzik, “Vertical-cavity surface-emitting lasers with birefringence splitting above 250 GHz”, *Electron. Lett.*, vol. 51, pp. 1600–1602, 2015.
- [10] A.K. Jansen van Doorn, M.P. van Exter, and J.P. Woerdman, “Elasto-optic anisotropy and polarization orientation of vertical-cavity surface-emitting semiconductor lasers”, *Appl. Phys. Lett.*, vol. 69, pp. 1041–1043, 1996.
- [11] A.K. Jansen van Doorn, M.P. van Exter, and J.P. Woerdman, “Tailoring the birefringence in a vertical-cavity semiconductor laser”, *Appl. Phys. Lett.*, vol. 69, pp. 3635–3637, 1996.
- [12] M. Daubenschütz and R. Michalzik, “Parameter extraction from temperature-dependent light–current–voltage data of vertical-cavity surface-emitting lasers”, in *Semiconductor Lasers and Laser Dynamics VII*, K.P. Panajotov, M. Sciamanna, A.A. Valle, R. Michalzik (Eds.), Proc. SPIE 9892, pp. 98920R-1–8, 2016.

Parallel-Driven VCSELs With Optically Controlled Current Confinement

Sven Bader

We present vertical-cavity surface-emitting lasers (VCSELs) with integrated phototransistor (PT) layers, arranged as four parallel-driven mesas in one row connected by thin ridges. Detailed studies about the turn-on process of the device are shown, as well as a direct visualization of the optically controlled current confinement. Light-current-voltage (LIV) operation curves with hysteresis loops were measured and simultaneous camera images were taken from the back side of the structure to record the turn-on/-off order of this device.

1. Introduction

VCSELs are widely known for their low threshold current [1] which requires a high current density in the active layers. Therefore, current spreading in the semiconductor material must be prevented by either mesa etching [2] or current-blocking layers, e.g., by proton implantation [3]. Epitaxial solutions with regrowth steps are also applicable [4]. Nowadays in most commercially available VCSELs, buried Al_xO_y oxide apertures funnel the pump current into the middle of the mesa [5]. The wet-thermal processing of these insulating layers depends on parameters like temperature and pressure which must be strictly controlled to obtain reproducible devices. Moreover, the volume of the aperture layers shrinks during oxidation. This results in a potentially problematic built-in strain near the light-emitting quantum wells (QWs) of the active zone of the VCSEL [6]. A novel oxide-free and regrowth-free approach uses the generated spontaneous light in the laser resonator in association with an epitaxially integrated PT for an optical definition of the current path through the device [7]. Initially, the PT, which is configured as an optical switch, acts as an insulating barrier layer. Only leakage current generates some spontaneous emission in the active zone, which is partly absorbed in a thin InGaAs quantum well (α -QW) embedded between the base and the collector layers. The resulting photocurrent takes the role of a base current and turns the most illuminated part of the PT layers conductive after exceeding a certain threshold base current, depending on the PT's current gain and the layer structure of the VCSEL. Hence, the current-voltage operation curve shows a negative differential resistance (NDR) region when the PT opens and the resistance decreases. Once opened, the current aperture remains stable in diameter, thus lasing starts after reaching the threshold current density. The advantages of this method are a less complex and accelerated manufacturing process and in addition, due to the lack of the oxide aperture, a reduced strain near the active zone. Ultimately, the PT-VCSEL is intended to exhibit improved reliability and efficiency compared to present oxidized VCSELs.

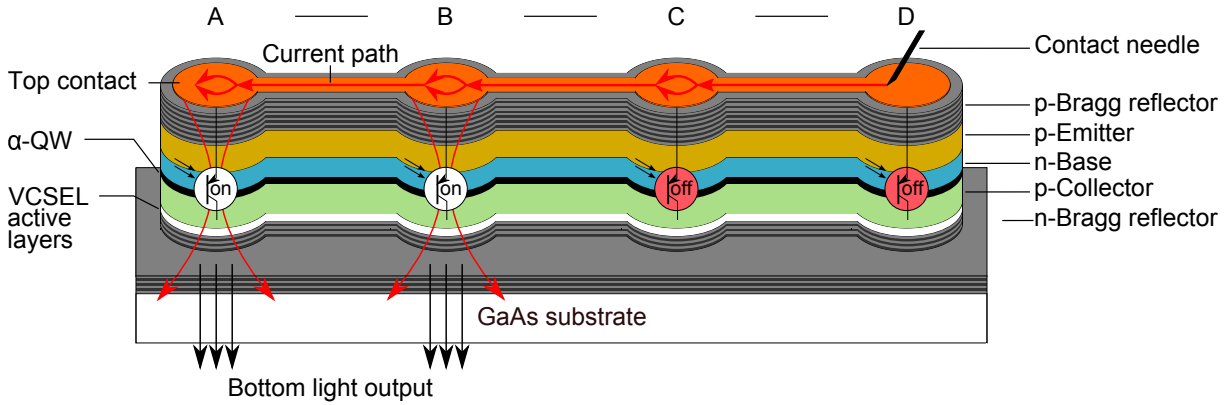


Fig. 1: Layout and operation principle of the four parallel-driven bottom-emitting VCSELs with integrated phototransistor layers for optically controlled current confinement. Initially, the phototransistor with the lowest voltage drop during dark-current operation begins to open and becomes conductive. The resulting spontaneous photons reach the neighboring mesas through the thin ridges and switch them on successively.

2. Device Structure

Bottom-emitting PT-VCSELs were grown on a n-type GaAs substrate by molecular beam epitaxy (MBE). The resonator is formed by p- and n-doped AlGaAs/GaAs Bragg mirrors consisting of 29 and 26.5 layer pairs, respectively. The simulated lossless reflectivities are $R_{\text{top}} = 99.91\%$ (including the top metal) and $R_{\text{bottom}} = 99.87\%$, while the estimated threshold gain is 1520 cm^{-1} . The active zone with three InGaAs QWs for lasing and the pnp-structure of the PT with a calculated current gain of only ≈ 2 are placed inside the cavity. The 6 nm thin α -QW, embedded between base and collector, has an absorption coefficient of $\approx 3500\text{ cm}^{-1}$. Owing to its small thickness and the low current gain, the PT requires high photon densities to switch its layers conductive. We have arranged four InGaAs/AlGaAs-based PT-VCSELs in one row which were reactive ion etched to the bottom reflector (see Fig. 1). Each mesa with a diameter of $45\text{ }\mu\text{m}$ is connected with a $60\text{ }\mu\text{m}$ long and $20\text{ }\mu\text{m}$ wide ridge. The Ti/Pt/Au metal contact is placed on the top reflector and extends over the whole structure. The back side of the substrate was kept free from metal to guarantee an unobstructed view at the light output pattern of the PT-VCSEL. Instead, a large-area n-contact is established between the sample and a Au-coated vacuum holder.

3. Experimental

The sample holder has a center opening for transmission of the bottom-emitted light. In addition to optical power measurements, the setup allows to take CCD camera images from the bottom side of the wafer and obtain new insights about the turn-on/-off process of the laser structure. The current source is connected to the sample holder and to a tungsten needle which contacts the metalization of the PT-VCSEL. After a measurement, the needle is moved to a different mesa to judge the influence of the contact position. The measured

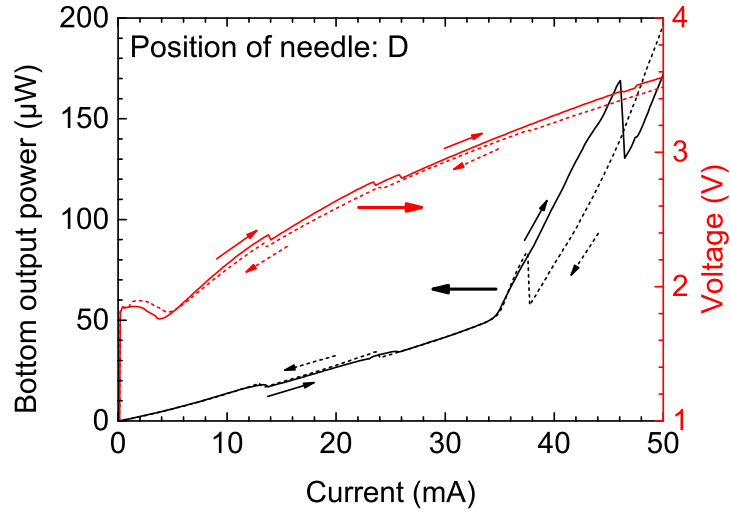


Fig. 2: Measured continuous-wave operation curves of the four parallel-driven PT-VCSELs. Each kink indicates a turn-on/-off point of a PT. The turn-off order of the PTs is different from that during turn-on, hence hysteresis loops exist.

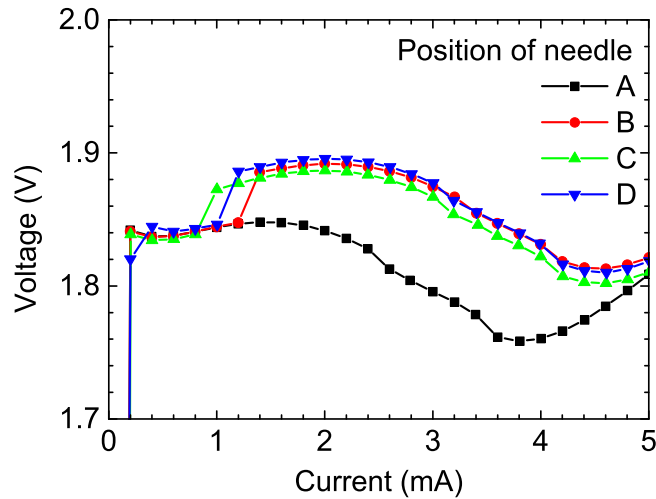


Fig. 3: Current-voltage measurements of the leakage current in the dark-current region for all contact positions of Fig. 1. For each trace, the pump current is reduced from 50 mA to zero to ensure the needle-contacted PT turns off last. Only the range from 0 to 5 mA is shown here. The voltage drop of the left mesa (position A) is less than of the others. Hence, due to the highest initial photon density, this PT always begins to turn on first.

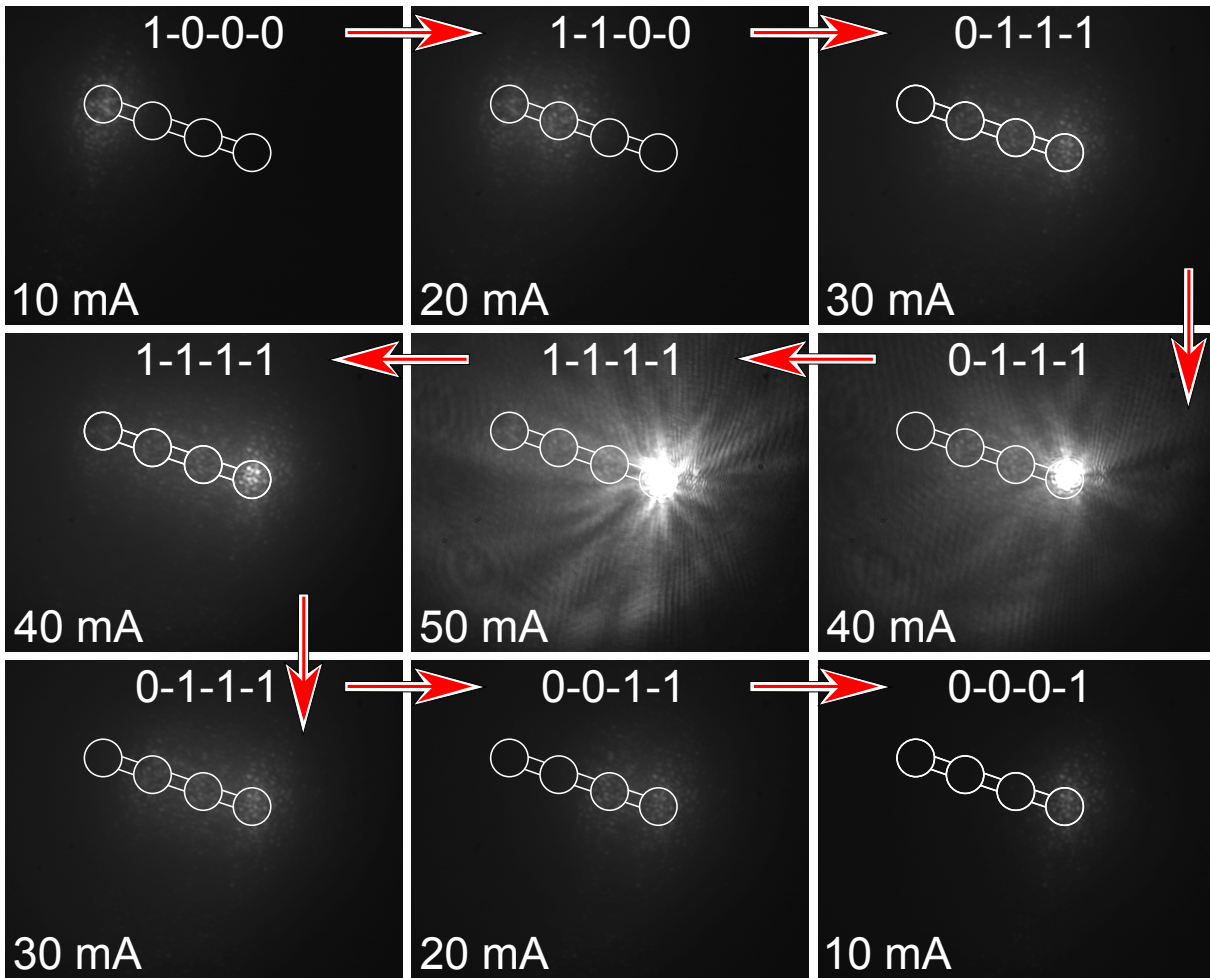


Fig. 4: Camera images of the bottom side of the PT-VCSEL arrangement at different currents during turn-on and -off. The four parallel-driven mesas are highlighted in white. “0” and “1” represent the off-/on-state of the PT in each mesa. The needle contacts the right mesa (position D in Fig. 1).

LIV curves when contacting the right mesa (see Fig. 1) are shown in Fig. 2. Ramping up the current from zero to 50 mA, each NDR region indicates the turn-on of a PT in one mesa. Owing to reflections of spontaneous photons at the etched walls, the whole mesa area becomes conductive. Initially, the PT with the lowest voltage drop during dark-current operation (see Fig. 3) begins to open, independent of the position of the needle. In the investigated structure it is the left mesa (see Fig. 4 (top left)) where the highest leakage current, respectively spontaneous emission, of the base-collector junction is to be expected. Subsequently, while further increasing the current, spontaneous emission reaches through the ridges to the neighboring mesas and successively turns these PTs on. The output power drops due to the decreased current density in the mesas. Lasing always starts at the needle-contacted mesa where the highest current density is expected owing to lateral ohmic losses. This leads to confinement effects where distant PTs can even switch off again, namely here while increasing the current from 20 to 30 mA (from switching state 1-1-0-0 to 0-1-1-1). In the NDR region around $I = 23$ mA, the light

output as an exception raises slightly due to the turn-off of the left PT, whereas the PT at position C opens. The NDR region at 26 mA originates from the turn-on of the right mesa. Only while further increasing the current, the left PT is able to open again because of the increasing current density, respectively the spontaneous emission, which reaches again the left mesa. While decreasing the pump current, the distant PTs switch off first, thus the turn-off order of the PTs is different from that during turn-on, as long as the needle does not contact the mesa which opens first. Therefore, hysteresis loops occur while the output power and voltage rise at each turn-off of a PT. The needle-contacted PT always turns off last, hence it is possible to characterize the leakage current (see Fig. 3) of each mesa separately.

4. Conclusion

In summary, we have presented a PT-VCSEL arrangement with four parallel-driven mesas connected with thin ridges, which experimentally demonstrates the process of optically controlled current confinement. Measured operation curves could be identified with camera images which illustrate the turn-on/-off behavior of the mesas. It is thus understood that each NDR region represents a new opening of a PT area owing to spontaneous photons traveling through the ridges. The leakage current has a major influence during the initial turn-on. The different sequence of the PT's switching points also represents the impact of non-negligible lateral ohmic losses in the layer structure. Lessons learned will be transferred to future generations of solitary device which will be optimized with respect to the degree of confinement (depending on the parameters of the PT, in particular the current gain), threshold current, and electro-optic efficiency.

Acknowledgment

The author thanks Philips Technologie GmbH, U-L-M Photonics for the project support and the MBE growth of the PT-VCSEL wafer. Furthermore the author is grateful to Dr.-Ing. Philipp Gerlach for many great discussions and the fruitful cooperation. The technical assistance of Susanne Menzel and Rudolf Rösch is highly appreciated.

References

- [1] R. Michalzik (Ed.), *VCSELs — Fundamentals, Technology and Applications of Vertical-Cavity Surface-Emitting Lasers*, Springer Series in Optical Sciences, vol. 166, Berlin: Springer-Verlag, 2013.
- [2] J.L. Jewell, A. Scherer, S.L. McCall, Y.H. Lee, S. Walker, J.P. Harbison, and L.T. Florez, “Low-threshold electrically pumped vertical-cavity surface-emitting micro-lasers”, *Electron. Lett.*, vol. 25, pp. 1123–1129, 1989.
- [3] M. Orenstein, A.C. Von Lehmen, C. Chang-Hasnain, N.G. Stoffel, J.P. Harbison, L.T. Florez, E. Clausen, and J.E. Jewell, “Vertical-cavity surface-emitting InGaAs/GaAs lasers with planar lateral definition”, *Appl. Phys. Lett.*, vol. 56, pp. 2384–2386, 1990.

- [4] M. Ortsiefer, W. Hofmann, J. Roskopf, and M.C. Amann, “Long-Wavelength VCSELs with Buried Tunnel Junction”, Chap. 10 in *VCSELs*, R. Michalzik (Ed.), pp. 321–351, Berlin: Springer-Verlag, 2013.
- [5] D.L. Huffaker, D.G. Deppe, K. Kumar, and T.J. Rogers, “Native-oxide defined ring contact for low threshold vertical-cavity lasers”, *Appl. Phys. Lett.*, vol. 65, pp. 97–99, 1994.
- [6] B.M. Hawkins, R.A. Hawthorne III, J.K. Guenter, J.A. Tatum, and J.R. Biard, “Reliability of various size oxide aperture VCSELs”, in Proc. *52nd Electron. Comp. and Technol. Conf., ECTC 2002*, pp. 540–550. San Diego, CA, USA, May 2002.
- [7] S. Bader, P. Gerlach, and R. Michalzik, “Optically controlled current confinement in vertical-cavity surface-emitting lasers”, *IEEE Photon. Technol. Lett.*, vol. 28, pp. 1309–1312, 2016

Computation of Transverse Optical Modes in Vertical-Cavity Surface-Emitting Lasers

Markus Daubenschütz

We present a finite-difference-based eigenvalue method for the computation of optical modes in waveguides with cylindrical symmetry. This approach is combined with the effective index method to determine the transverse modes in the resonator of vertical-cavity surface-emitting lasers (VCSELs) and to investigate the thermal guiding and the guiding provided by the buried oxide layers. We introduce the mathematical fundamentals of the finite difference method which is first applied to a step-index waveguide structure that allows a comparison with analytical solutions. Field distributions and polarizations of the modes are shown. Afterwards, multi-step and graded refractive index profiles as they arise in VCSELs are analyzed and the influence of the oxide width on the guiding is investigated.

1. Introduction

VCSELs are key optoelectronic devices for data communication in high-performance computing, data centers, and in-building networks [1, 2]. The performance of such lasers depends on numerous design parameters that influence the current flow, the heat generation inside the device, and the optical characteristics. To develop and optimize next-generation VCSELs with data rates of 28 Gbit/s and above [3, 4] or to enable new applications, an accurate prediction of the influence of design changes is inevitable. Therefore we have established a quasi-three-dimensional simulation framework to compute the electro-thermal characteristics of different epitaxial and geometrical designs [5, 6]. The simulations are based directly on the epitaxial design protocols. Beside the electrical and thermal characteristics, the knowledge of the optical properties is a major aspect. To complete our tool we have implemented a set of algorithms to compute the transverse modes inside the cavity. In Sect. 2 we show the mathematical foundation of the eigenvalue method based on finite differences and we compare the results with analytical solutions of step-index optical fiber structures. The next section extends the technique to VCSEL structures with rotational symmetry and a more complex refractive index profile.

2. Finite Difference Method

The implementation of the mode solver is based on the finite difference method (FDM). The underlying refractive index distribution is obtained by approximating the laser cavity by a longitudinally homogeneous waveguide structure. The mathematical approach of the FDM is the separation of electric and magnetic fields and the computation of

transverse fields by finite differences while analytical expressions are available in the direction of propagation. The generalized transmission line (GTL) equations derived from Maxwell's equations in cylindrical coordinates describe the relations between the electric and magnetic fields by [7]

$$-i\epsilon_r \begin{bmatrix} E_r \\ E_\phi \end{bmatrix} = \frac{\partial}{\partial \bar{z}} \begin{bmatrix} \bar{H}_\phi \\ -\bar{H}_r \end{bmatrix} + \begin{bmatrix} -\frac{1}{\bar{r}} \frac{\partial}{\partial \phi} \\ \frac{\partial}{\partial \bar{r}} \end{bmatrix} \bar{H}_z, \quad (1)$$

$$-i\mu_r \begin{bmatrix} \bar{H}_\phi \\ -\bar{H}_r \end{bmatrix} = \frac{\partial}{\partial \bar{z}} \begin{bmatrix} E_r \\ E_\phi \end{bmatrix} - \begin{bmatrix} \frac{\partial}{\partial \bar{r}} \\ \frac{1}{\bar{r}} \frac{\partial}{\partial \phi} \end{bmatrix} E_z, \quad (2)$$

where $i = \sqrt{-1}$ and ϵ_r and μ_r are the relative permittivity and permeability, respectively. We have normalized the coordinates $u = r, z$ with the free-space wavenumber $k = 2\pi/\lambda$ as $\bar{u} = uk$ and the magnetic field $\bar{H} = HZ_0$ with the free-space wave impedance $Z_0 = \sqrt{\mu_0/\epsilon_0}$. Applying Faraday's law

$$\bar{H}_z = i \frac{1}{\mu_r \bar{r}} \begin{bmatrix} -\frac{1}{\bar{r}} \frac{\partial}{\partial \phi} & \frac{\partial}{\partial \bar{r}} \bar{r} \end{bmatrix} \begin{bmatrix} \bar{r} E_r \\ E_\phi \end{bmatrix} \quad (3)$$

in (1) and Ampère's law for dielectric material

$$E_z = -i \frac{1}{\epsilon_r \bar{r}} \begin{bmatrix} \frac{\partial}{\partial \bar{r}} & \frac{\partial}{\partial \phi} \end{bmatrix} \begin{bmatrix} \bar{r} \bar{H}_\phi \\ -\bar{H}_r \end{bmatrix} \quad (4)$$

in (2), the GTL equations are rewritten as

$$\frac{\partial [H]_t}{\partial \bar{z}} = -i \mathbf{R}_E [E]_t, \quad \frac{\partial [E]_t}{\partial \bar{z}} = -i \mathbf{R}_H [H]_t \quad (5)$$

with the transverse field components

$$[E]_t = \begin{bmatrix} \bar{r} E_r \\ E_\phi \end{bmatrix}, \quad [H]_t = \begin{bmatrix} \bar{r} \bar{H}_\phi \\ -\bar{H}_r \end{bmatrix}. \quad (6)$$

The matrix elements \mathbf{R}_E and \mathbf{R}_H in (5) include the derivatives in \bar{r} - and ϕ -directions and the material parameters ϵ_r and μ_r of the structure. The two matrices have the form [8]

$$\mathbf{R}_E = \begin{bmatrix} \epsilon_r + \frac{1}{\bar{r}^2} \frac{\partial}{\partial \phi} \frac{1}{\mu_r} \frac{\partial}{\partial \phi} & -\frac{1}{\bar{r}} \frac{\partial}{\partial \phi} \frac{1}{\mu_r} \frac{\partial}{\partial \bar{r}} \bar{r} \\ -\frac{\partial}{\partial \bar{r}} \frac{1}{\mu_r \bar{r}^2} \frac{\partial}{\partial \phi} & \epsilon_r + \frac{\partial}{\partial \bar{r}} \frac{1}{\mu_r \bar{r}} \frac{\partial}{\partial \bar{r}} \bar{r} \end{bmatrix} \quad (7)$$

and

$$\mathbf{R}_H = \begin{bmatrix} \mu_r + \bar{r} \frac{\partial}{\partial \bar{r}} \frac{1}{\epsilon_r \bar{r}} \frac{\partial}{\partial \bar{r}} & \bar{r} \frac{\partial}{\partial \bar{r}} \frac{1}{\epsilon_r \bar{r}} \frac{\partial}{\partial \phi} \\ \frac{1}{\bar{r}^2} \frac{\partial}{\partial \phi} \frac{1}{\epsilon_r} \frac{\partial}{\partial \bar{r}} & \mu_r + \frac{1}{\bar{r}^2} \frac{\partial}{\partial \phi} \frac{1}{\epsilon_r} \frac{\partial}{\partial \phi} \end{bmatrix}. \quad (8)$$

The combination of the two equations in (5) leads to

$$\frac{\partial^2 [E]_t}{\partial \bar{z}^2} - \mathbf{Q}_E [E]_t = 0, \quad (9)$$

$$\frac{\partial^2 [H]_t}{\partial \bar{z}^2} - \mathbf{Q}_H [H]_t = 0, \quad (10)$$

where we used the operation matrices \mathbf{Q}_E and \mathbf{Q}_H that arise from the matrix products

$$\mathbf{Q}_E = -\mathbf{R}_H \mathbf{R}_E, \quad \mathbf{Q}_H = -\mathbf{R}_E \mathbf{R}_H. \quad (11)$$

Only the transverse field components are included in (9) and (10) and the derivatives in longitudinal \bar{z} and transverse ϕ - and \bar{r} -directions are separated. By replacing the derivatives in (7) and (8) by finite differences one can solve the system of equations by a transformation to principal axes

$$\mathbf{T}_E \mathbf{\Gamma}_E^2 \mathbf{T}_E^{-1} = \mathbf{Q}_E, \quad \mathbf{T}_H \mathbf{\Gamma}_H^2 \mathbf{T}_H^{-1} = \mathbf{Q}_H, \quad (12)$$

where the matrices $\mathbf{\Gamma}_{E,H}$ include the eigenvalues and the matrices $\mathbf{T}_{E,H}$ the eigenvectors of the $\mathbf{Q}_{E,H}$ matrices. The columns of eigenvectors correspond to the field distributions of the modes in the structure, whereas the principal axis of the eigenvalues $\mathbf{\Gamma}$ contains the propagation constants of the modes in the form

$$\bar{\gamma} = \sqrt{\mathbf{\Gamma}} = \bar{\kappa} + i\bar{n}_{\text{eff}}, \quad (13)$$

where $\bar{\kappa} = \alpha/(2k)$ is the amplitude attenuation coefficient normalized with k and \bar{n}_{eff} is the effective index such that the mode propagates with the propagation factor $\exp\{-\bar{\gamma}\bar{z}\} = \exp\{-\alpha\bar{z}/2\} \exp\{-i\bar{n}_{\text{eff}}kz\}$ for a wave traveling in $+z$ -direction. We assume structures with material parameters not depending on the ϕ -direction and a perfect cylindrical symmetry. One can then replace the ϕ -dependency with

$$E_r, \bar{H}_\phi \propto \cos(m\phi), \quad E_\phi, \bar{H}_r \propto \sin(m\phi) \quad (14)$$

or vice versa. Therefore we can simplify (7) and (8) to the forms

$$\mathbf{R}_E = \begin{bmatrix} \epsilon_r - m^2 \frac{1}{\mu_r \bar{r}^2} & -m \frac{1}{\mu_r} D_{\bar{r}} \bar{r} \\ m D_{\bar{r}} \frac{1}{\mu_r \bar{r}^2} & \epsilon_r + D_{\bar{r}} \frac{1}{\mu_r \bar{r}} D_{\bar{r}} \bar{r} \end{bmatrix}, \quad (15)$$

$$\mathbf{R}_H = \begin{bmatrix} \mu_r + \bar{r} D_{\bar{r}} \frac{1}{\epsilon_r \bar{r}} D_{\bar{r}} & m \bar{r} D_{\bar{r}} \frac{1}{\epsilon_r \bar{r}} \\ -m \frac{1}{\epsilon_r \bar{r}^2} D_{\bar{r}} & \mu_r - m^2 \frac{1}{\epsilon_r \bar{r}^2} \end{bmatrix}, \quad (16)$$

where we have substituted the derivative $\frac{\partial}{\partial \bar{r}}$ by a finite difference matrix $D_{\bar{r}}$ [7]. The related coordinate system for the discretization with finite differences is shown in Fig. 1. Worth to mention is the half-step shift $\Delta \bar{r}/2$ between the E_r, \bar{H}_ϕ and E_ϕ, \bar{H}_r fields, which is caused by the first-order derivative of the coupling between the field components in (15) and (16). As boundary conditions in the center at $\bar{r} = 0$ we use the Neumann condition $\frac{\partial F}{\partial \bar{r}} = 0$ for E_ϕ, \bar{H}_r and the Dirichlet condition $F = 0$ for $\bar{r} E_r, \bar{r} \bar{H}_\phi$. Due to the multiplication of E_r and \bar{H}_ϕ with \bar{r} the Dirichlet boundary condition is fulfilled without forcing the field component itself to zero.

The results of the finite difference computation are compared to an analytical solution for a weakly guiding step-index fiber with a refractive index $\bar{n}_{\text{co}} = 1.5$ in the core with

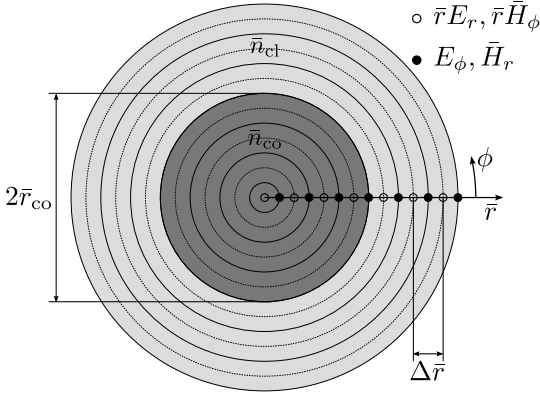


Fig. 1: Coordinate system for a finite difference discretization of a step-index fiber with rotational symmetry.

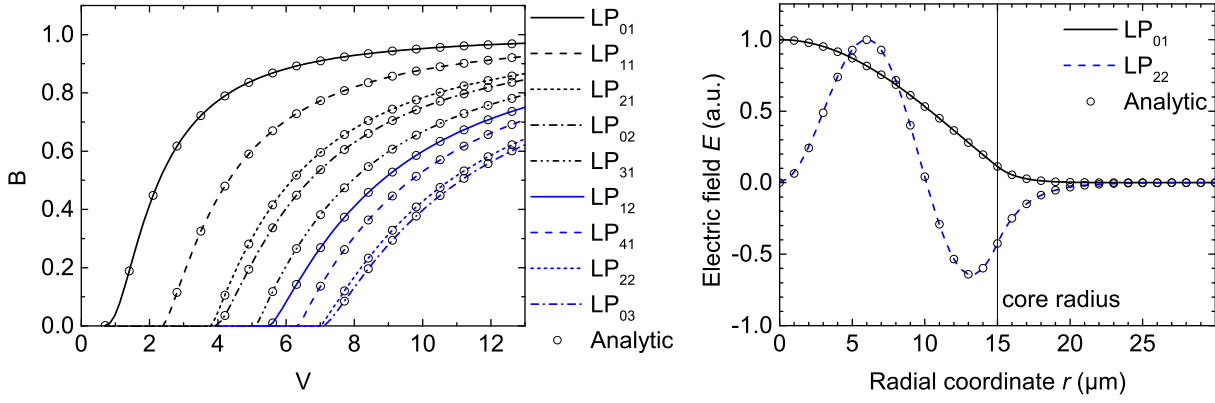


Fig. 2: Comparison of analytic and finite difference solutions of the phase parameter $B = (\bar{n}_{\text{eff}}^2 - \bar{n}_{\text{cl}}^2)/(\bar{n}_{\text{co}}^2 - \bar{n}_{\text{cl}}^2)$ and the frequency parameter $V = kr_{\text{co}}\sqrt{\bar{n}_{\text{co}}^2 - \bar{n}_{\text{cl}}^2}$ for the first nine LP modes of a step-index fiber (left) and two radial field distributions for refractive indices $\bar{n}_{\text{co}} = 1.5$ and $\bar{n}_{\text{cl}} = 1.497$ and a core radius $r_{\text{co}} = 15 \mu\text{m}$ (right). The radius of the simulation window is $80 \mu\text{m}$ and the discretization step width is $0.1 \mu\text{m}$

$0 \leq r \leq \bar{r}_{\text{co}}\lambda/(2\pi)$ and $\bar{n}_{\text{cl}} = 1.497$ in the cladding with $r > \bar{r}_{\text{co}}\lambda/(2\pi)$. The analytical solutions are found by solving the characteristic equation [9, 10]

$$\frac{u \cdot J_l(u)}{J_{l-1}(u)} = -\frac{w \cdot K_l(w)}{K_{l-1}(w)} \quad (17)$$

with the Bessel function J describing the field distribution in the core and the modified Hankel function K for the evanescent fields in the cladding. Solutions of the FDM are the so-called EH and HE modes. It is convenient to approximate the modes inside a VCSEL as a superposition of nearly degenerated EH and HE modes. These are the linearly polarized LP_{lp} modes in the combination $\text{EH}_{l-1,p}$ and $\text{HE}_{l+1,p}$ with the azimuthal order l and the radial order p [9]. In Fig. 2 (left) we plot the BV diagram of the fiber for the first nine LP modes. There is a perfect accordance of analytic and finite difference solutions. The radial field distributions of two modes in the same fiber with core radius $r_{\text{co}} = 15 \mu\text{m}$ are shown in Fig. 2 (right). To illustrate the origin of the LP modes we show in Fig. 3 the two-dimensional electric field profiles and the corresponding electric field polarizations of two quasi-degenerated EH_{01} and HE_{21} modes with an effective index $\bar{n}_{\text{eff}} = 1.4997$ for

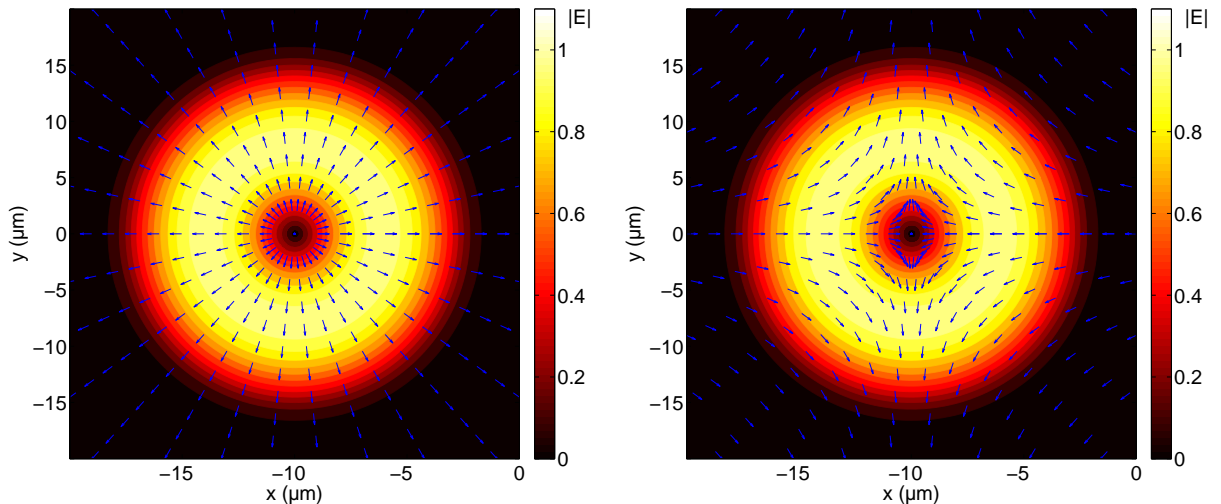


Fig. 3: Two-dimensional electric field profiles and electric field polarizations of the EH_{01} (left) and HE_{21} (right) modes in a step-index fiber with $\bar{n}_{\text{co}} = 1.5$, $\bar{n}_{\text{cl}} = 1.497$, and $r_{\text{co}} = 15 \mu\text{m}$.

$r_{\text{co}} = 15 \mu\text{m}$. The addition of these modes forms the linearly polarized LP_{11} mode that is shown in Fig. 4. It should be mentioned that this mode can occur in two orientations, namely $\sin \phi$ and $\cos \phi$, and two orthogonal linear polarizations.

3. VCSEL Modes

The FDM described in the previous section enables us to evaluate the influence of different design parameters on the optical guiding in VCSEL structures with more complex refractive index profiles compared to a simple step-index fiber. To determine the radial refractive index profile we combine our approach with the effective index method [11] that

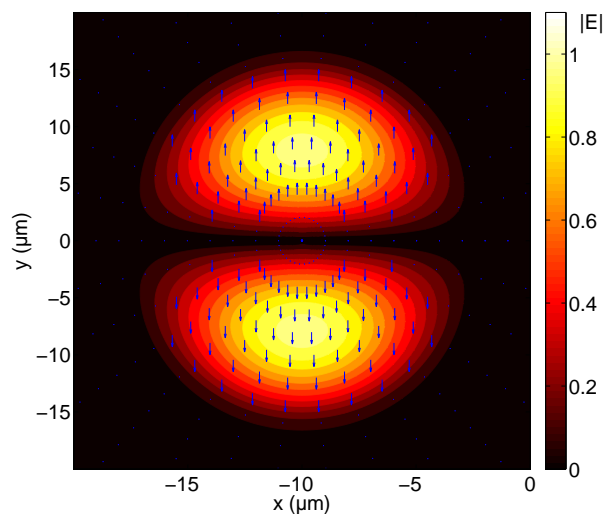


Fig. 4: Two-dimensional electric field profile and electric field polarization of the LP_{11} mode that originates from the addition of the EH_{01} and HE_{21} modes in Fig. 3.

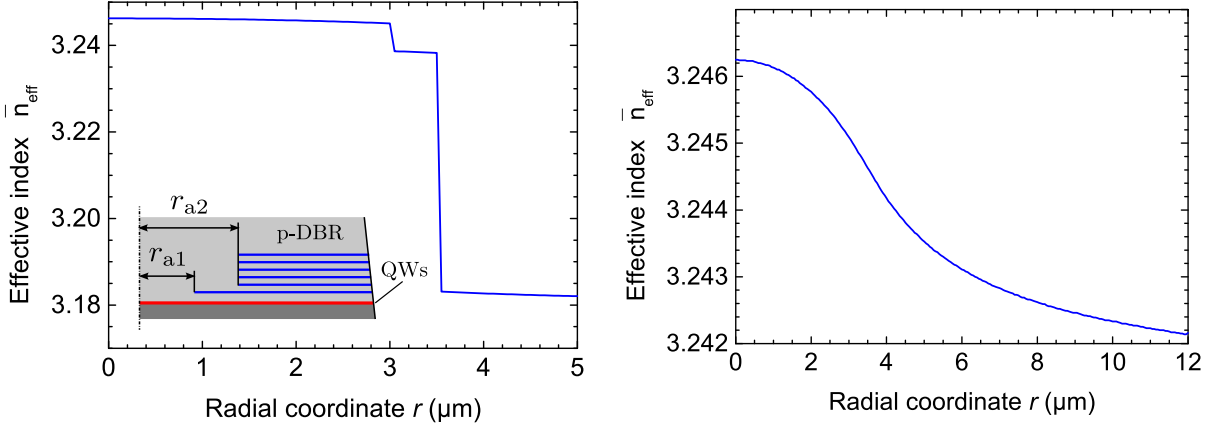


Fig. 5: Radial effective index profile of an oxide-confined VCSEL with one main aperture with active radius $r_{a1} = 3 \mu\text{m}$ and five additional apertures with $r_{a2} = 3.5 \mu\text{m}$ as well as a thermally induced index profile (left) and the same profile without the influence of the oxide layers (right).

gives a relation between the change of the resonance wavelength $\Delta\lambda$ and the change of the effective index $\Delta\bar{n}_{\text{eff}}$, namely

$$\frac{\Delta\lambda}{\lambda} = \frac{\Delta\bar{n}_{\text{eff}}}{\bar{n}_{\text{eff}}} \quad (18)$$

with the initial resonance wavelength λ and the effective index \bar{n}_{eff} . The values of $\Delta\lambda = \Delta\lambda(r)$ are determined with the one-dimensional transfer matrix method [12]. With this approximation we can evaluate the influence of thermal lensing as well as the guiding provided by one or multiple oxide layers. Figure 5 (left) depicts the effective index profile of an oxide-confined datacom VCSEL with one main aperture and five additional apertures with larger diameter to reduce the capacitance of the device, as indicated in the inset. The radii are $r_{a1} = 3 \mu\text{m}$ and $r_{a2} = 3.5 \mu\text{m}$ for the main and the additional apertures, respectively. The laser cavity consists of three quantum wells sandwiched between 26 top and 33.5 bottom mirror pairs. The influence of the oxide layers on the effective index profile is quite strong, which is due to the high index difference $\Delta\bar{n} \approx 1.4$ between aluminum oxide and AlGaAs. The effective index steps are $\Delta\bar{n}_{\text{eff}} = 0.006$ and 0.055 for the main and the additional apertures, respectively. The profile in Fig. 5 (left) includes both the oxide and thermal effects on the refractive index. In contrast, Fig. 5 (right) exclusively shows the thermally induced effective index profile for a dissipated electrical power $P_{\text{diss}} = 14 \text{ mW}$. The radial temperature profile inside the cavity causes a decreasing \bar{n}_{eff} with increasing radial coordinate. This \bar{n}_{eff} profile results in the so-called thermal lensing, which in the given case is small compared to the built-in guiding. The LP modes guided by the effective index profile $\bar{n}_{\text{eff}}(r)$ are then computed according to Sect. 2. The first six transverse modes of the oxide configuration of Fig. 5 (left) are displayed in Fig. 6 (left). On the right side of Fig. 6 we set the radii r_{a2} of the additional oxide layers to 3, 3.5, and $4 \mu\text{m}$ and compute the profiles of the corresponding fundamental LP_{01} modes. Larger r_{a2} obviously lead to a widening of the mode profiles. This effect is expected to saturate owing to the guiding effect of $\Delta\bar{n}_{\text{eff}}$ at $r = r_{a1}$.

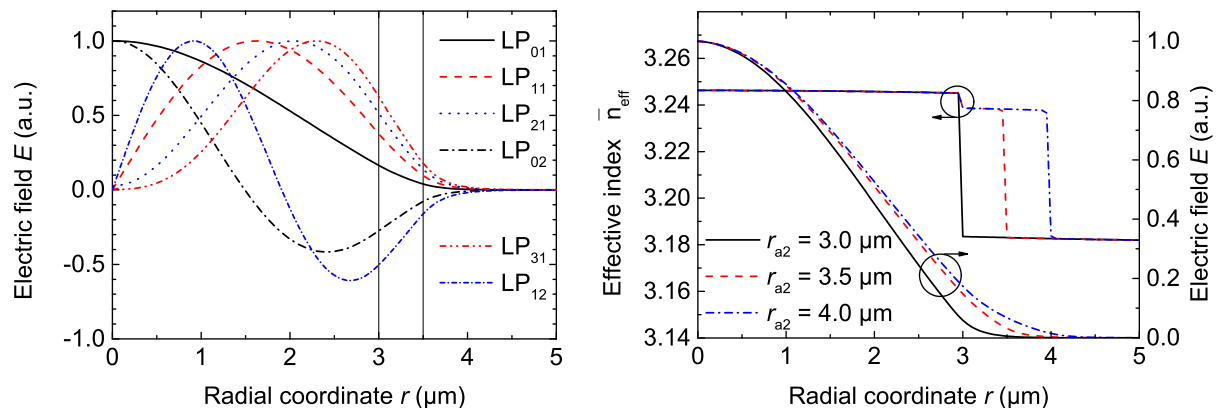


Fig. 6: Radial field profiles of the first six transverse modes in an oxide-confined VCSEL cavity with $r_{a1} = 3 \mu\text{m}$ and $r_{a2} = 3.5 \mu\text{m}$ (indicated as vertical lines) (left) and the resulting LP_{01} modes of the same structure with changing r_{a2} (right).

4. Conclusion

We have introduced a finite-difference-based eigenvalue method for the computation of optical modes in cylindrical geometries. In combination with the effective index method this approach can be used to evaluate the distributions of the linearly polarized LP modes inside the cavity of VCSELs with complex refractive index profiles. As a brief example we have calculated different modes of an oxide-confined VCSEL and have investigated the influence of variations of an oxide aperture diameter on the optical guiding.

Acknowledgment

We thank Philips Technologie GmbH, U-L-M Photonics, Germany for the fruitful collaboration and the German Federal Ministry of Education and Research (BMBF) for funding the HyPOT project.

References

- [1] K. Jackson and C. Schow, “VCSEL-Based Transceiver for Data Communication”, Chap. 14 in *VCSELs*, R. Michalzik (Ed.), pp. 431–448, Berlin: Springer, 2013.
- [2] D. Kuchta, “Progress in VCSEL-Based Parallel Links”, Chap. 16 in *VCSELs*, R. Michalzik (Ed.), pp. 473–519, Berlin: Springer, 2013.
- [3] P. Westbergh, R. Safaisini, E. Haglund, J. Gustavsson, A. Larsson, M. Green, R. Lawrence, and A. Joel, “High-speed oxide confined 850 nm VCSELs operating error-free at 40 Gb/s up to 85°C”, *IEEE Photon. Technol. Lett.*, vol. 25, pp. 768–771, 2013.

- [4] D.M. Kuchta, A.V. Rylyakov, F.E. Doany, C.L. Schow, J.E. Proesel, C.W. Baks, P. Westbergh, J.S. Gustavsson, and A. Larsson, “A 71-Gb/s NRZ modulated 850-nm VCSEL-based optical link”, *IEEE Photon. Technol. Lett.*, vol. 27, pp. 577–580, 2015.
- [5] M. Daubenschütz, P. Gerlach, and R. Michalzik, “Electro-thermal characteristics of VCSELs: simulations and experiments”, in *Semiconductor Lasers and Laser Dynamics VI*, K.P. Panajotov, M. Sciamanna, A.A. Valle, R. Michalzik (Eds.), Proc. SPIE 9134, pp. 91342H-1–8, 2014.
- [6] M. Daubenschütz, P. Gerlach, and R. Michalzik, “Epitaxy-based electro-thermal simulation approach for vertical-cavity surface-emitting laser structures”, in *Online Digest Conf. on Lasers and Electro-Optics Europe, CLEO/Europe 2015*, paper CB-P.14, one page. Munich, Germany, Jun. 2015.
- [7] R. Pregla, *Analysis of Electromagnetic Fields and Waves*, Weilheim: Wiley, 2013.
- [8] S.T. Helfert, “Modelling the coupling of electromagnetic waves to cylindrical waveguides with the method of lines”, *Opt. Quantum Electron.*, vol. 48, pp. 242-1–14, 2016.
- [9] H.-G. Unger, *Optische Nachrichtentechnik* (2nd ed.), Heidelberg: Hüthig, 1990.
- [10] K. Okamoto, *Fundamental of Optical Waveguides*, San Diego: Academic Press, 2000.
- [11] G.R. Hadley, “Effective index model for vertical-cavity surface-emitting lasers”, *Opt. Lett.*, vol. 20, pp. 1483–1485, 1995.
- [12] R. Michalzik, “VCSEL-Fundamentals”, Chap. 2 in *VCSELs*, R. Michalzik (Ed.), pp. 19–75, Berlin: Springer, 2013.

Parasitic Background Doping in Semipolar GaN

Marian Caliebe and Ferdinand Scholz

Semipolar GaN layers grown by metalorganic vapor phase epitaxy typically show quite strong n-type background doping, mainly caused by parasitic oxygen incorporation. In the studies reported here, we have investigated how to influence this parasitic doping by varying the growth temperature and the V-III ratio. Moreover, direct correlation with other sample properties, particularly the surface roughness, has been observed. Surprisingly, thick semipolar GaN layers grown by hydride vapor phase epitaxy exhibit very high background doping at the interface to the template and at the surface, whereas the carrier concentration seems to be significantly lower in the main part of the bulk layer.

1. Introduction

Semipolar GaN layers and respective heterostructures have attracted strong interest over the recent years (see, e.g., [1, 2] and references therein) as possible solutions to the so-called ‘green-gap problem’, i.e., the decrease of the LED efficiency when the color of the emitted light is shifted from blue to green. A major part of this problem is considered to be caused by the internal piezoelectric field in the active GaInN quantum wells of conventional structures grown in the polar c -direction, being larger for higher In content as needed for longer wavelength emission. In contrast, semipolar layers are grown in other, less polar directions leading to strongly reduced piezoelectric fields. However, in spite of these research activities, semipolar LEDs could not yet outperform their polar counterparts (see, e.g., results obtained in our recent research group PolarCoN [3] and in our EC project ALIGHT [4]). Typically, the lower quality of semipolar structures is blamed for this deficiency. In particular, a high basal plane stacking fault (BSF) density is to emphasize as the main difference to conventional c -plane structures. Moreover, a significantly higher background carrier concentration above 10^{18} cm^{-3} is observed in nominally undoped semipolar GaN layers [5, 6]. In the studies presented here, we have investigated by which growth parameters these concentrations can be influenced and eventually reduced. Besides parameters like temperature or V-III ratio, also the surface roughness of the layers seem to play an important role.

2. Experimental

The semipolar layers investigated here are grown on stripe-patterned sapphire wafers as described previously [7]. In brief, this procedure is described as follows: Few micrometer wide stripe trenches are dry-etched in specifically oriented sapphire wafers having inclined c -plane-like side-facets. These side-facets are the nucleation sites for the GaN

growth performed in an Aixtron AIX-200/4 RF-S HT low-pressure horizontal metalorganic vapor phase epitaxy (MOVPE) reactor. After having grown out of the trenches — basically growing along the inclined c -direction —, the GaN stripes eventually coalesce forming a layer with semipolar surface. For a $(11\bar{2}2)$ surface, sapphire wafers with r -plane orientation have been used. We have optimized this process carefully (see, e.g. [8]) achieving dislocation densities below 10^8 cm^{-2} and BSF densities of 200 cm^{-1} . Here, we focus mainly on the electrical and other properties of the top layer having a typical thickness of 2–3 μm grown on an about 5 μm thick multi-layer buffer structure [7]. Thicker layers up to several 100 μm have been deposited on these templates by hydride vapor phase epitaxy [9].

Carrier concentrations have been determined by C-V measurements. Moreover, the oxygen content was evaluated by secondary ion mass spectrometry (SIMS)². Low-temperature photoluminescence (PL) and scanning electron microscopy based cathodoluminescence (CL)³ spectra have been analyzed with respect to carrier concentration and defects like stacking faults. The surface roughness was determined by atomic force microscopy (AFM).

3. Results and Discussion

3.1 Variation of growth parameters

In order to find relations between the parasitic background doping and the growth procedure, we have grown several series of samples. As reference, we take conditions which have been optimized for c -plane growth and slightly modified in order to get best crystalline quality of semipolar layers [7]. As mentioned above, we found quite high background doping concentrations of about $7 \cdot 10^{17} \text{ cm}^{-3}$ for these conditions ($T = 1041 \text{ }^\circ\text{C}$, V-III $\simeq 560$), whereas comparable c -plane layers show concentrations below $1 \cdot 10^{17} \text{ cm}^{-3}$.

When increasing the growth temperature, we observed a significant decrease of the carrier concentration (Fig. 1). SIMS data of the oxygen concentration in some of these layers show the same trend confirming that indeed oxygen is the main impurity in these layers. This trend is often observed in MOVPE grown layers [10]. However, when decreasing the temperature below $1000 \text{ }^\circ\text{C}$, we also observed a decrease of carrier concentration and oxygen content [11]. Obviously, a maximum oxygen uptake happens around $1000 \text{ }^\circ\text{C}$.

The NH_3 flow and hence the V-III ratio is another growth parameter expected to significantly influence the background doping. Indeed, we observed a distinct decrease of the carrier concentration with decreasing V-III ratio, again nicely accompanied by a respective decrease of the O concentration as detected by SIMS. These data suggest that NH_3 may be a source of oxygen, although we have used best quality NH_3 with a purity of 6.0.

3.2 Influence of surface roughness on background doping?

Besides the above-mentioned growth parameters, it seems that also the surface roughness of our $(11\bar{2}2)$ layers influences the parasitic incorporation of n-type impurities like oxygen.

²SIMS evaluation was performed by RTG Mikroanalyse GmbH, Berlin.

³CL measurements have been done by M. Hocker *et al.*, Inst. of Quantum Matter, Ulm University.

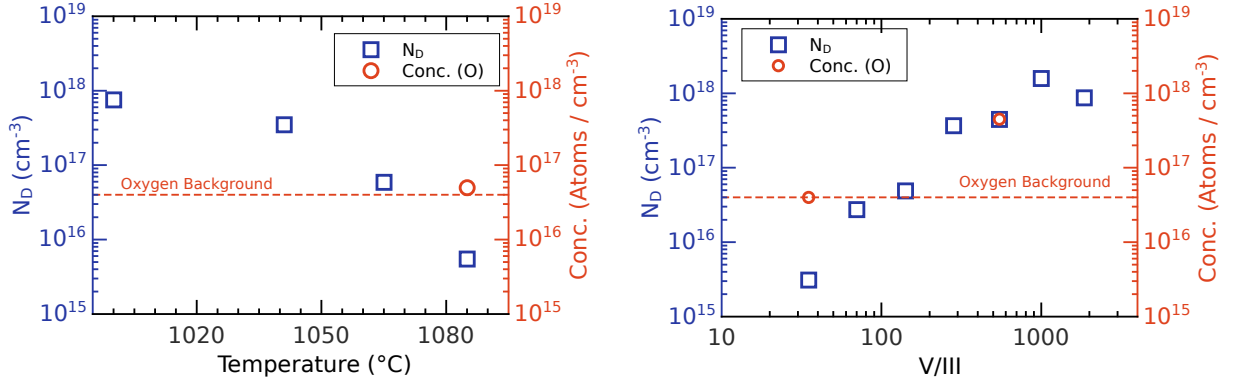


Fig. 1: Carrier concentration in $(11\bar{2}2)$ layers determined by C-V measurements as a function of growth temperature ($V\text{-III} = 564$, left) and V-III ratio ($T = 1041$ °C, right).

Layers with different surface roughness have been obtained by varying the sapphire trench period. Such studies have been performed to find the optimum periodicity for our growth procedure [12]. Analyzing low temperature PL spectra of this series, we observed that the intensity ratio between the donor-bound exciton (D^0, X) and the free exciton (X_A) lines correlate perfectly with the absolute intensity of the (D^0, X) line and even with the surface roughness measured by AFM (Fig. 2). This ratio is a qualitative indication of the donor density. Therefore, we also performed C-V measurements on these samples. Indeed, the donor concentration coincides also with the roughness data. This may be explained by the strong oxygen sensitivity of a perfect $(11\bar{2}2)$ plane, whereas other planes (being present in rougher surfaces) incorporate less oxygen.

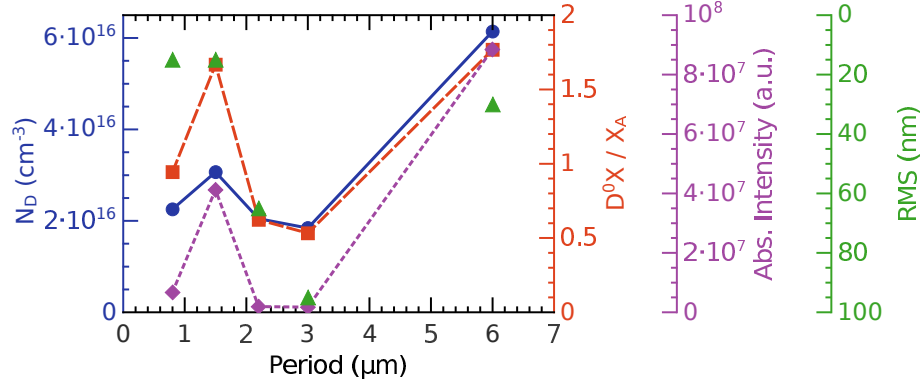


Fig. 2: Donor concentration, intensity ratio of (D^0, X) and (X_A) PL lines, absolute intensity, and surface roughness plotted versus stripe period of our sample series where the latter was varied between 0.8 and 6 μm .

3.3 Background doping in HVPE-grown semipolar layers

Previous low-temperature PL measurements on our HVPE-grown $(11\bar{2}2)$ layers have shown the presence of a so-called “free electron recombination band” (FERB) broadening the typically very sharp (D^0X) peak and extending it particularly to higher en-

ergies [13]. This is consistent with very high n-type background doping concentrations in the 10^{19} cm^{-3} range for the near-surface volume probed by PL, whereas comparable *c*-plane layers always exhibit carrier concentrations in the mid 10^{16} cm^{-3} range [14]. Such high carrier concentrations have also been confirmed by van der Pauw Hall experiments which yield average values for the whole layers.

In order to check details of such parasitic background doping in these layers, we have analyzed the cross-section of a (11 $\bar{2}$ 2) layer grown by HVPE on top of an MOVPE grown buffer as discussed above up to a total thickness of approximately 300 μm . Details of this growth procedure have been published in [9]. This sample was grown with a growth rate of about 100 $\mu\text{m}/\text{h}$.

Local luminescence spectra have been obtained by SEM-based CL at $T \approx 10 \text{ K}$. Surprisingly, we observed quite sharp peaks over most of the cross-section indicating a lower carrier concentration, while the FERB dominated near the MOVPE-HVPE interface and close to the upper sample surface. By analyzing the shape of these peaks⁴, the local carrier concentration can be deduced, as depicted in Fig. 3. These data could be confirmed and further quantified by analyzing the luminescence peak position of the signal of the basal plane stacking fault I_1 which was found to be sensible to the carrier concentration [15]. Indeed, fairly low carrier concentrations around 10^{18} cm^{-3} can be deduced from those spectra in the main bulk region between lower interface and upper surface.

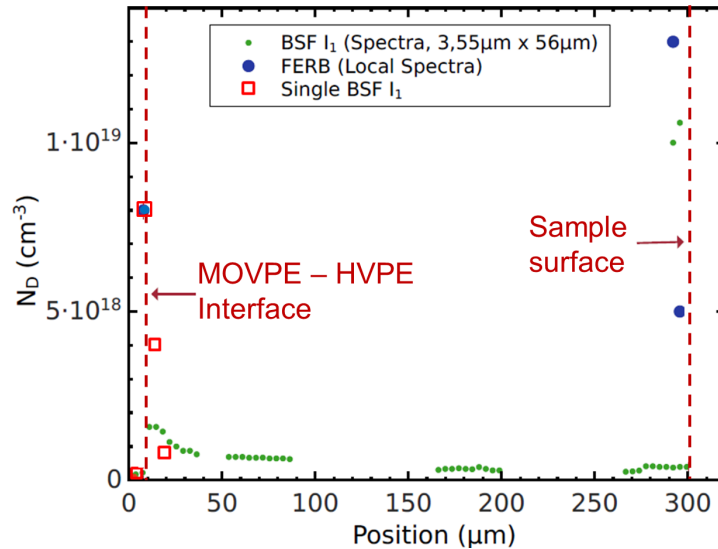


Fig. 3: Donor concentration profile over the cross-section of a semipolar GaN layer with a thickness of about 300 μm , determined by various methods (see text).

4. Conclusion

We have investigated the parasitic background doping in semipolar (11 $\bar{2}$ 2) GaN layers grown by MOVPE and HVPE. In both cases, we find high background doping, obviously

⁴Performed by M. Hocker and K. Thonke, Inst. of Quantum Matter, Ulm University.

due to parasitic oxygen incorporation. This is assumed to be a consequence of the chemical properties of such surface, being more nitrogen-polar than a conventional GaN layer grown in c -direction and hence being Ga-polar. Indeed, nitrogen-polar layers are known to incorporate oxygen much more efficiently than Ga-polar layers [16, 17]. For MOVPE-grown semipolar layers, the background doping can be significantly reduced by varying the growth temperature or decreasing the V-III ratio. In HVPE grown layers, fair carrier concentrations have been found in the bulk region with much higher concentrations incorporated at the beginning and at the end of the growth. At the beginning, this may be due to oxygen or water deposits on the surface of the template when transporting it from the MOVPE machine to the HVPE reactor. However, further studies are required to find good explanations for the very high concentrations at the end of growth.

Acknowledgment

We are grateful to M. Hocker and K. Thonke (Inst. of Quantum Matter, Ulm University) for CL evaluations and to N. Hibst (Inst. of Electronic Devices and Circuits, Ulm University) for his help concerning the C-V measurements. S. Tandukar, Z. Cheng (Inst. of Optoelectronics) and A. Plettl (Inst. of Solid State Physics, Ulm University) assisted to realize the sub-micrometer stripe period structures. Moreover, our thanks go to RTG Mikroanalyse GmbH for SIMS analysis.

References

- [1] F. Scholz, “Semipolar GaN grown on foreign substrates: a review”, *Semicond. Sci. Technol.*, vol. 27, pp. 024002-1–15, 2012.
- [2] F. Scholz, M. Caliebe, G. Gahramanova, D. Heinz, M. Klein, R.A.R. Leute, T. Meisch, J. Wang, M. Hocker, and K. Thonke, “Semipolar GaN-based heterostructures on foreign substrates”, *Phys. Status Solidi B*, vol. 253, pp. 13–22, 2016.
- [3] “Polarization field control in nitride light emitters”, F. Scholz and U. Schwarz (Eds.), pp. 3–185, *Phys. Status Solidi B*, Jan. 2016.
- [4] B. Corbett, Z. Quan, D.V. Dinh, G. Kozlowski, D. O’Mahony, M. Akhter, S. Schulz, P. Parbrook, P. Maaskant, M. Caliebe, M. Hocker, K. Thonke, F. Scholz, M. Pristovsek, Y. Han, C.J. Humphreys, F. Brunner, M. Weyers, T.M. Meyer, and L. Lymperakis, “Development of semipolar (11-22) LEDs on GaN templates”, H. Jeon, L.W. Tu, M.R. Krames, and M. Strassburg (Eds.), Proc. SPIE 9768, pp. 97681G-1–9, 2016.
- [5] S.C. Cruz, S. Keller, T.E. Mates, U.K. Mishra, and S.P. DenBaars, “Crystallographic orientation dependence of dopant and impurity incorporation in GaN films grown by metalorganic chemical vapor deposition”, *J. Cryst. Growth*, vol. 311, pp. 3817–3823, 2009.

- [6] T. Zhu, D. Sutherland, T.J. Badcock, R. Hao, M.A. Moram, P. Dawson, M.J. Kappers, and R.A. Oliver, “Defect reduction in semi-polar (11 $\bar{2}2$) gallium nitride grown using epitaxial lateral overgrowth”, *Jpn. J. Appl. Phys.*, vol. 52, pp. 08JB01-1–5, 2013.
- [7] M. Caliebe, Y. Han, M. Hocker, T. Meisch, C. Humphreys, K. Thonke, and F. Scholz, “Growth and coalescence studies of (11 $\bar{2}2$) oriented GaN on pre-structured sapphire substrates using marker layers”, *Phys. Status Solidi B*, vol. 253, pp. 46–53, 2016.
- [8] M. Caliebe, T. Meisch, M. Madel, and F. Scholz, “Effects of miscut of prestructured sapphire substrates and MOVPE growth conditions on (11 $\bar{2}2$) oriented GaN”, *J. Cryst. Growth*, vol. 414, pp. 100–104, 2015.
- [9] M. Caliebe, T. Meisch, B. Neuschl, S. Bauer, J. Helbing, D. Beck, K. Thonke, M. Klein, D. Heinz, and F. Scholz, “Improvements of MOVPE grown (11 $\bar{2}2$) oriented GaN on pre-structured sapphire substrates using a SiN_x interlayer and HVPE overgrowth”, *Phys. Status Solidi C*, vol. 11, pp. 525–529, 2014.
- [10] B. Chung and M. Gershenson, “The influence of oxygen on the electrical and optical properties of GaN crystals grown by metalorganic vapor phase epitaxy”, *J. Appl. Phys.*, vol. 72, pp. 651–659, 1992.
- [11] F. Scholz, T. Meisch, and K. Elkhoully, “Efficiency studies on semipolar GaInN-GaN quantum well structures”, *Phys. Status Solidi A*, vol. 213, pp. 3117–3121, 2016.
- [12] M. Caliebe, S. Tandukar, Z. Cheng, M. Hocker, Y. Han, T. Meisch, D. Heinz, F. Huber, S. Bauer, A. Plettl, C. Humphreys, K. Thonke, and F. Scholz, “Influence of trench period and depth on MOVPE grown GaN on patterned r-plane sapphire substrates”, *J. Cryst. Growth*, vol. 440, pp. 69–75, 2016.
- [13] P. Schustek, M. Hocker, M. Klein, U. Simon, F. Scholz, and K. Thonke, “Spectroscopic study of semipolar (11-22)-HVPE GaN exhibiting high oxygen incorporation”, *J. Appl. Phys.*, vol. 116, pp. 163515-1–9, 2014.
- [14] F. Lipski, T. Wunderer, S. Schwaiger, and F. Scholz, “Fabrication of freestanding 2”-GaN wafers by hydride vapour phase epitaxy and self-separation during cooldown”, *Phys. Status Solidi A*, vol. 207, pp. 1287–1291, 2010.
- [15] M. Hocker, I. Tischer, B. Neuschl, K. Thonke, M. Caliebe, M. Klein, and F. Scholz, “Stacking fault emission in GaN: influence of n-type doping”, *J. Appl. Phys.*, vol. 119, pp. 185703-1–6, 2016.
- [16] M. Sumiya, K. Yoshimura, K. Ohtsuka, and S. Fuke, “Dependence of impurity incorporation on the polar direction of GaN film growth”, *Appl. Phys. Lett.*, vol. 76, pp. 2098–2100, 2000.
- [17] N.A. Fichtenbaum, T.E. Matesa, S. Keller, S.P. DenBaars, and U.K. Mishra, “Impurity incorporation in heteroepitaxial N-face and Ga-face GaN films grown by metalorganic chemical vapor deposition”, *J. Cryst. Growth*, vol. 310, pp. 1124–1131, 2008.

Selective Functionalization of GaInN Quantum Well Surfaces for Applications in Biosensing

Dominik Heinz and Martin F. Schneidereit

In this work, chemical functionalization of the surface of gallium indium nitride (GaInN) quantum well structures is performed aiming to study biosensing of the iron-storage molecule ferritin. In order to enable local investigations of ferritin molecules, a local functionalization of the group III-nitride surface with silane molecules is performed. Our studies demonstrate a preferred attachment of ferritin molecules on the functionalized quantum well surface.

1. Introduction

Besides prominent applications in general lighting and lasing, chemical sensing based on III-nitride semiconductors finds increasing interest [1–5]. Group III-nitrides provide a very stable [6] and biocompatible [5] material system with excellent optoelectronic properties. Today, biosensing methods are frequently based on fluorescent labels which can be selectively linked to biomolecules [7] and enable subsequent optical investigations down to the microscopic scale [7,8].

However, fluorescent dyes are often reported to suffer from photobleaching effects [9,10] and weak light intensity [10] which limits applications in biosensing [7,9,11]. Moreover, fluorescent molecules are typically not selective to specific molecular properties such as the iron-load of ferritin molecules [12,13]. Hence, new label-free sensing approaches are of interest for next generation optical biosensing. Ferritin molecules play a key role in regulating the iron status of the human body [12]. Within their spherical cavity, up to 4500 iron atoms can be reversibly stored [12]. Besides the molecular concentration of ferritin in human blood, the iron-load is reported as a superior biomarker [13].

In our recent studies, a new approach for sensing ferritin bound iron is demonstrated applying polar GaInN quantum wells as optochemical transducers [14]. Ferritin and apoferritin molecules immobilized onto the GaN semiconductor surface cause spectral shifts of the polar GaInN quantum well photoluminescence [14]. Apoferritin corresponds to ferritin molecules without iron-load. Spectral shifts are associated to changes of the quantum confined Stark effect (QCSE) present in polar GaInN quantum wells.

In this study, a local functionalization of GaInN quantum well structures for selective binding of ferritin molecules is studied. Hence, local photoluminescence changes caused by adsorbed ferritin molecules can be investigated in micro-photoluminescence spectroscopy.

2. Key-Lock Principle

In order to enable local investigations of (apo)ferritin molecules, a chemical functionalization of the III-nitride semiconductor surface with silane molecules is studied. Both, the semiconductor surface and (apo)ferritin molecules are functionalized with molecules which obey very specific binding properties. By using a key-lock principle, (apo)ferritin molecules can be locally attached to the III-nitride semiconductor surface. A schematic illustration of the applied key-lock principle for selective attachment of ferritin on GaN is given in Fig. 1.

In this work, a local surface functionalization with 3-mercaptopropyltrimethoxysilane (MPTMS) is studied. Silane molecules bind to OH groups present on the hydroxylated GaN surface and obey a functional SH group. A functional maleimide group can be attached to (apo)ferritin. The interaction between the functional SH group of MPTMS and the maleimide group is highly specific [16]. Ferritin molecules with functional maleimide group selectively bind to the SH group present on the silanized semiconductor surface. Optionally, fluorescent rhodamine dyes can be attached to (apo)ferritin in order to allow fluorescence microscopic investigations for cross-checking the surface functionalization. In the target sensor design, local changes of the GaInN quantum well photoluminescence shall be used for sensing the ferritin molecules as discussed in [14].

Two different approaches for local silanization of group III-nitrides are investigated. First, selective stamping of silanes onto the semiconductor surface is performed. Polydimethylsiloxane (PDMS) stamps are realized using structured silicon wafers as templates. A SU-8 2000 photoresist is structured on the silicon wafer using conventional optical lithography. The viscous PDMS is molded on the structured wafer and hardened for several hours. Subsequently, the elastic PDMS stamp can be removed from the substrate and mounted on a step motor based setup which allows a controlled stamping of different surfaces with silanes. The detailed stamping sequence is given in Fig. 2.

In order to exclude silanization of nominally unpatterned areas, a second approach based on the selective evaporation of silanes onto the semiconductor surface is applied using a shadow mask. MPTMS is evaporated onto the uncovered areas of the sample. Subsequently, the mask is removed from the sample surface and the template is rinsed with toluene to remove unbound silanes. In contrast to the micro-contact patterning, an improved selectivity is expected with less silane molecules in nominally unpatterned areas.

Polar GaInN quantum well structures are realized on sapphire wafers in a commercial Aixtron AIX200/RF metal organic vapor phase epitaxy (MOVPE) reactor using ammonia (NH_3), trimethylgallium (TMGa), trimethylaluminum (TMAI), triethylgallium (TEGa), and trimethylindium (TMIn) as precursors. First, a thin oxygen-doped aluminum nitride (AlN) nucleation layer is realized, followed by a Ga-polar GaN buffer layer. GaInN quantum wells with a thickness of 3 nm, 7 nm GaN barrier thickness, and a GaN cap layer with a thickness of about 7 nm are realized. Before deposition of the silane molecules, the semiconductor surface is hydroxylated using a mixture of sulfuric acid and hydrogen peroxide.

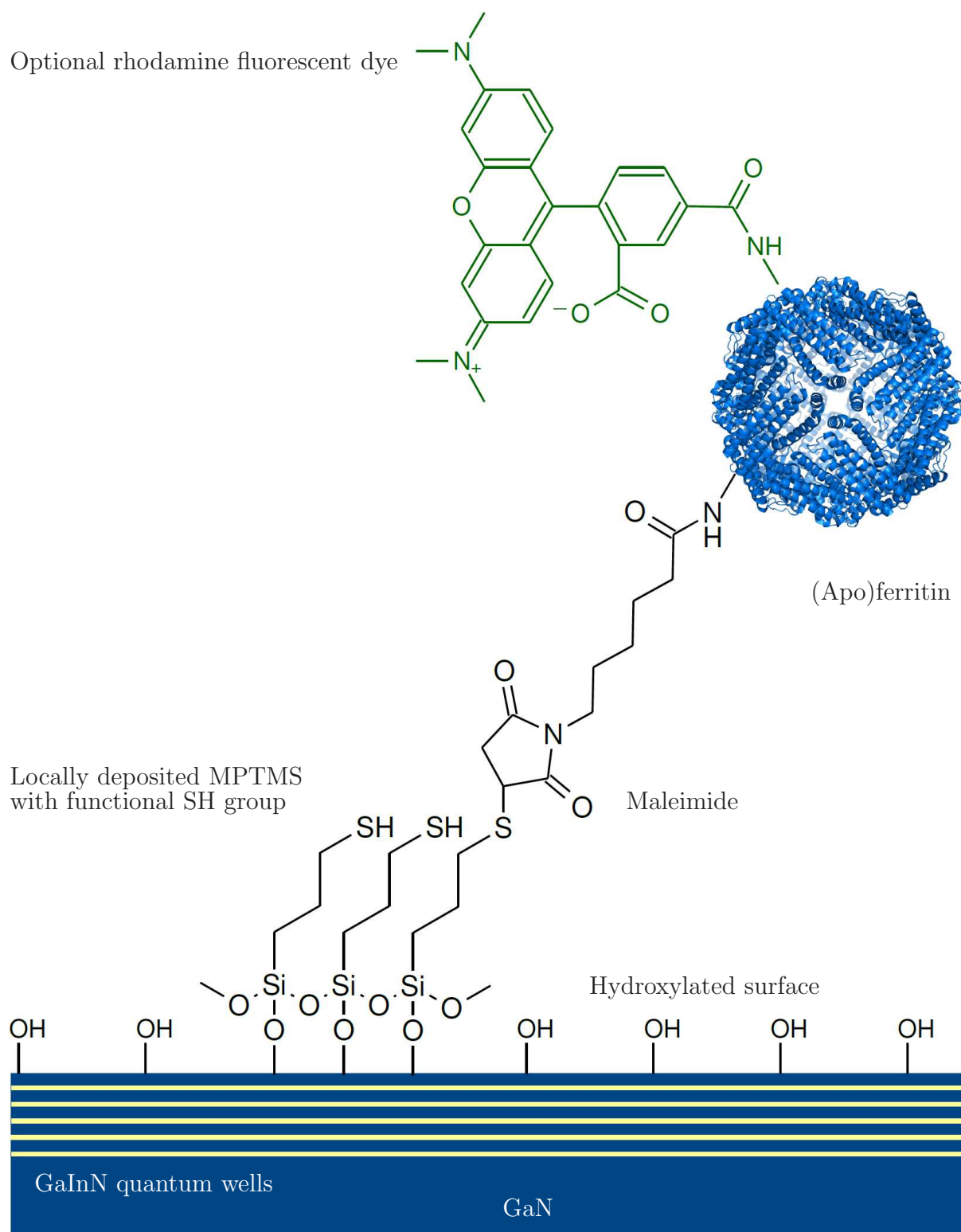


Fig. 1: Schematic illustration of the key-lock principle. Silane molecules are locally deposited onto the hydroxylated GaN surface. The functional SH group of MPTMS selectively binds to the maleimide group which is linked to the (apo)ferritin molecule in a separate functionalization step. Optionally, a fluorescent rhodamine dye can be attached to the (apo)ferritin molecules. Apoferritin was visualized with PyMol (PDB ID: 4V1W) [15].

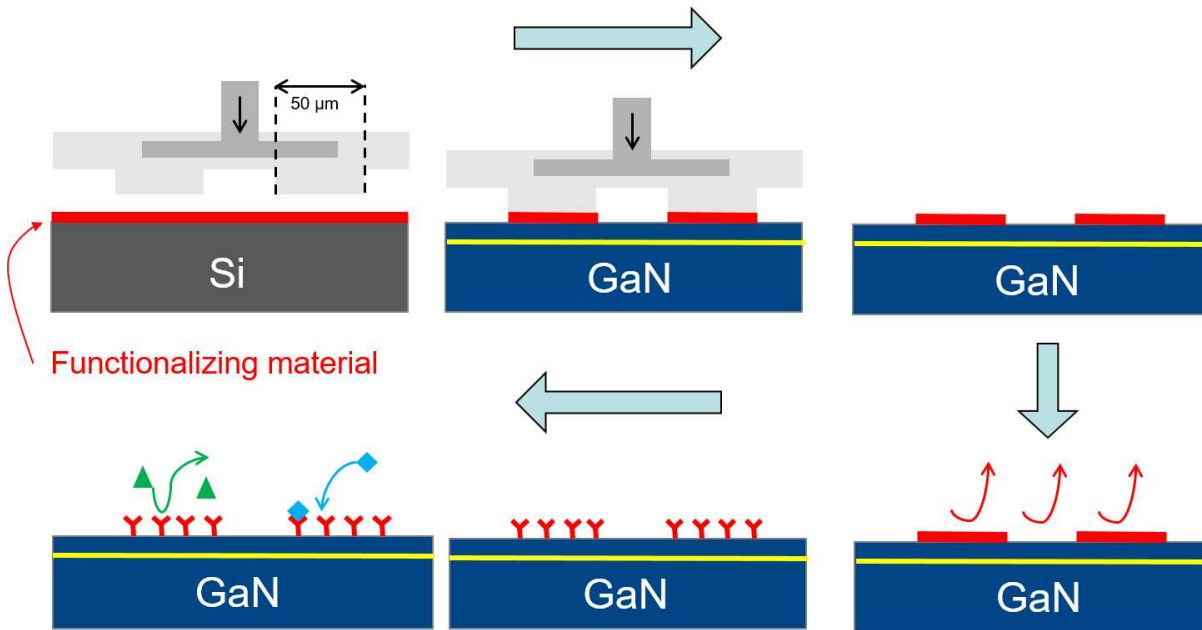


Fig. 2: Schematic illustration of the stamping procedure for selective deposition of silane on the hydroxylated GaN surface. In the first step, the PDMS stamp is loaded with MPTMS. Subsequently, the silane molecules are locally deposited on GaN and link to OH groups on the GaN surface. Unbound silanes are removed by rinsing the sample with toluene. The silanized areas on the surface allow a selective binding to the maleimide group of functionalized (apo)ferritin molecules.

3. Selective Binding of Ferritins

In our first experiments, a selective attachment of ferritin molecules on cheap glass substrates was studied in order to optimize the micro-contact patterning process. After silanization of the surface, (apo)ferritin molecules with functional maleimide group are attached to the SH group of the silane molecules. Ferritin molecules are drop-casted on the silanized surface and incubated for one hour. After incubation the samples are dipped in water in order to remove unspecifically bound ferritin molecules from the surface.

Fluorescent micrographs of selectively attached ferritin molecules incubated with high and low concentration are given in Fig. 3 (left, right), respectively. A selective attachment of fluorescent ferritin molecules on glass is clearly visible using fluorescence microscopy (Fig. 3). However, ferritin molecules also unspecifically attach in nominally not functionalized areas on glass. A periodic pattern with continuously increasing periodicity was chosen. Higher concentrations of ferritin are found in unpatterned areas with smaller periodicity of the stamping pattern. In areas with small periodicity silane molecules are expected to accumulate during the stamping process. Hence, fluorescent ferritins also attach in these areas.

Using the established micro-contact processing (Fig. 2), silane molecules are locally deposited on GaN surfaces. Due to the higher electrical conductivity of GaN in contrast to glass, scanning electron microscopy can be performed on the silanized GaN surface. A scanning electron micrograph of a silanized GaN surface is given in Fig. 4. Due to the

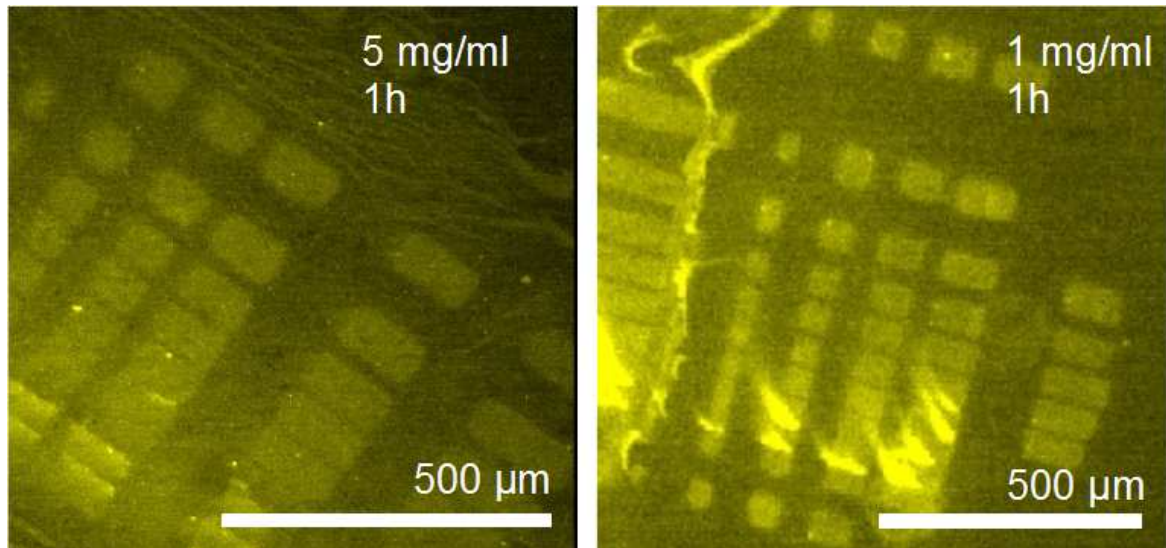


Fig. 3: Fluorescence micrograph of locally functionalized glass substrates using the silane stamping procedure after subsequent attachment of ferritin molecules. A selective attachment of fluorescent ferritin molecules is observed besides unspecifically bound ferritin in nominally not silanized areas.

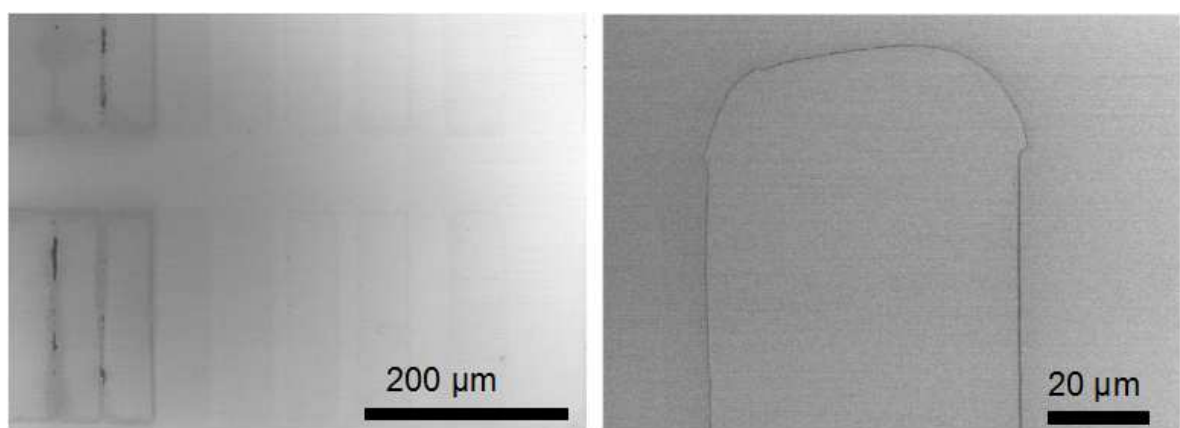


Fig. 4: Scanning electron micrograph of a silanized GaN surface using micro-contact patterning. Accumulations of MPTMS molecules are visible in areas with smaller periodicity of the stamp pattern (black areas).

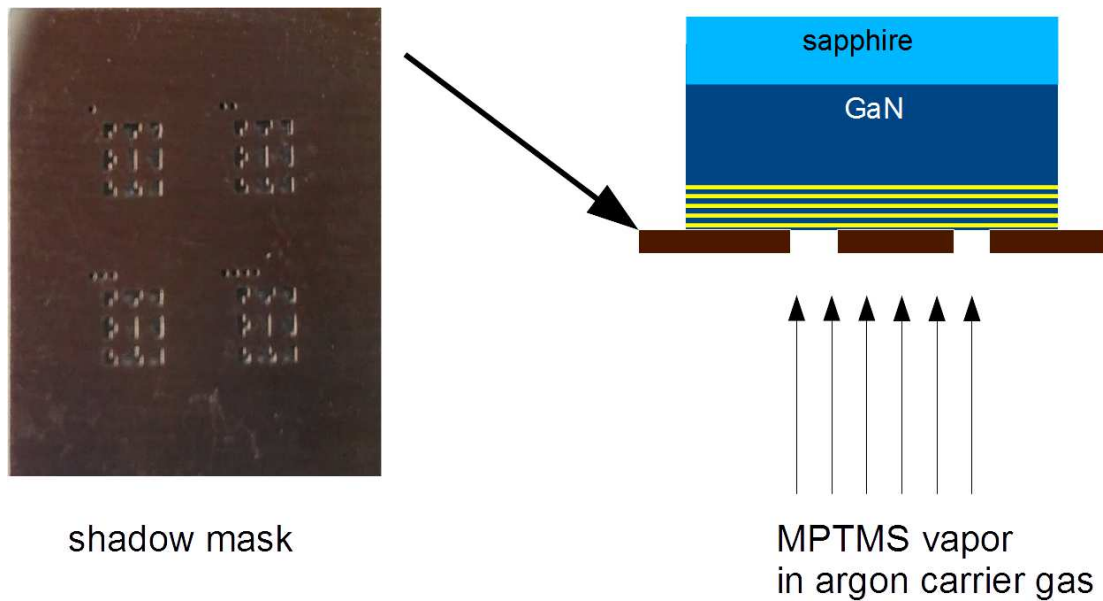


Fig. 5: Selective evaporation of silane molecules onto a masked GaN template.

material contrast (back-scattering) between the silanized and unpatterned GaN surface, the stamping pattern is clearly visible. As expected from our observations on glass substrates, accumulations of silane molecules are found in areas with small periodicity of the PDMS stamp pattern. Similar to our observations on glass, ferritin molecules are found to unspecifically bind in unpatterned areas (not shown).

In order to avoid contamination of nominally unpatterned areas with silane molecules during the micro-contact patterning, local evaporation of MPTMS onto a masked GaN surface is studied (Fig. 5). After silanization, a small droplet with ferritin is deposited on the patterned area and incubated for 1 hour. Subsequently, the sample is rinsed with ultrapure water to remove unspecifically bound ferritin.

In fluorescence and scanning electron microscopy, the shape of the original ferritin droplet is clearly visible (Fig. 6, left and right, respectively). A clear correlation of the attached ferritin molecules to the silane pattern is possible. However, again unspecifically bound ferritin molecules are found to preferably attach to unpatterned areas on GaN. Hence, GaN is found to be highly attractive for ferritin molecules and further investigations are necessary to remove unspecifically bound ferritin.

4. Summary

In this work, chemical functionalization of planar GaInN quantum well structures with silane molecules for local immobilization of ferritin molecules is demonstrated. Our studies provide a first step for next-generation biosensors using local photoluminescence changes of GaInN quantum wells interacting with ferritin molecules immobilized on the semiconductor surface. Two different approaches are studied based on micro-contact patterning and selective evaporation of silane molecules. A selective attachment of ferritin molecules on GaN is found as well as unspecifically bound ferritin on GaN.

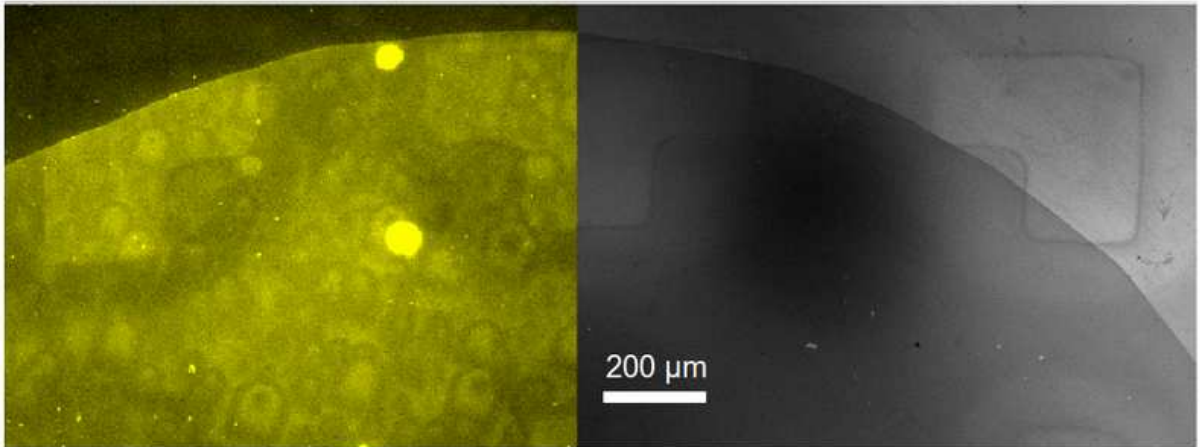


Fig. 6: Fluorescence micrograph of locally functionalized GaN templates using selective evaporation of MPTMS after subsequent local attachment of ferritin molecules (left), corresponding scanning electron micrograph (right). A selective attachment of fluorescent ferritin molecules can be observed besides unspecifically bound ferritin.

Acknowledgment

Scientific support by L. Wu, J. Shabaz (Institute of Optoelectronics, Ulm University), F. Huber, S. Bauer, B. Hörbrand, K. Thonke (Institute of Quantum Matter / Semiconductor Physics Group, Ulm University), S. Chakraborty, N. Naskar, Y. Wu, T. Weil (Institute of Organic Chemistry III, Ulm University), and T. Sandner (Institute of Analytical and Bioanalytical Chemistry, Ulm University) is gratefully acknowledged. This work was financially supported by the Baden-Württemberg Stiftung gGmbH within the project “Intelligente optoelektronische Biosensoren”.

References

- [1] J. Teubert, P. Becker, F. Furtmayr, and M. Eickhoff, “GaN nanodiscs embedded in nanowires as optochemical transducers”, *Nanotechnology*, vol. 22, pp. 275505-1–5, 2011.
- [2] S. Paul, A. Helwig, G. Müller, F. Furtmayr, J. Teubert, and M. Eickhoff, “Optochemical sensor system for the detection of H₂ and hydrocarbons based on InGaN/GaN nanowires”, *Sens. Actuators B*, vol. 173, pp. 120–126, 2012.
- [3] K. Maier, A. Helwig, G. Müller, P. Becker, P. Hille, J. Schörmann, J. Teubert, and M. Eickhoff, “Detection of oxidising gases using an optochemical sensor system based on GaN/InGaN nanowires”, *Sens. Actuators B*, vol. 197, pp. 87–94, 2014.
- [4] B. Chu, C. Chang, S.J. Pearton, J. Lin, and F. Ren, “Recent advances in wide-bandgap semiconductor biological and gas sensors”, Ch. 2 in *Semiconductor Device-Based Sensors for Gas, Chemical, and Biomedical Applications*, F. Ren and S. Pearton (Eds.), p. 43, Boca Raton: CRC Press, 2011.

- [5] I. Cimalla, M. Gebinoga, A. Schober, V. Polyakov, V. Lebedev, and V. Cimalla, "AlGaIn/GaN sensors for direct monitoring of nerve cell response", Ch. 1 in *Semiconductor Device-Based Sensors for Gas, Chemical, and Biomedical Applications*, F. Ren and S.J. Pearton (Eds.), p. 1, Boca Raton: CRC Press, 2011.
- [6] K.A. Son, A. Liao, G. Lung, M. Gallegos, T. Hatake, R.D. Harris, L.Z. Scheick, and W.D. Smythe, "GaN-based high-temperature and radiation-hard electronics for harsh environments", in *Micro- and Nano-Harsh Environment Sensors*, T. George, M.S. Islam, and A.K. Dutta (Eds.), Proc. SPIE 7679, pp. 76790U-1-8, 2010.
- [7] J. Eid *et al.*, "Real-time DNA sequencing from single polymerase molecules", *Science*, vol. 323, pp. 133-138, 2009.
- [8] M.C. Estevez, M.A. Otte, B. Sepulveda, and L.M. Lechuga, "Trends and challenges of refractometric nanoplasmonic biosensors: a review", *Anal. Chim. Acta*, vol. 806, pp. 55-73, 2014.
- [9] J.R. Heath and M.E. Davis, "Nanotechnology and cancer", *Annu. Rev. Med.*, vol. 59, pp. 251-265, 2008.
- [10] A. Ermakova, G. Pramanik, J.M. Cai, G. Algara-Siller, U. Kaiser, T. Weil, Y.K. Tzeng, H.C. Chang, L.P. McGuinness, M.B. Plenio, B. Naydenov, and F. Jelezko, "Detection of a few metallo-protein molecules using color centers in nanodiamonds", *Nano Lett.*, vol. 13, pp. 3305-3309, 2013.
- [11] M.J. Levene, J. Korlach, S.W. Turner, M. Foquet, H.G. Craighead, and W.W. Webb, "Zero-mode waveguides for single-molecule analysis at high concentrations", *Science*, vol. 299, pp. 682-686, 2003.
- [12] Y. Ren and T. Walczyk, "Quantification of ferritin bound iron in human serum using species-specific isotope dilution mass spectrometry", *Metallomics*, vol. 6, pp. 1709-1717, 2014.
- [13] V. Herbert, E. Jayatilleke, S. Shaw, A.S. Rosman, P. Giardina, R.W. Grady, B. Bowman, and E.W. Gunter, "Serum ferritin iron, a new test, measures human body iron stores unconfounded by inflammation", *Stem Cell*, vol. 15, pp. 291-296, 1997.
- [14] D. Heinz, F. Huber, M. Spiess, M. Asad, L. Wu, O. Rettig, D. Wu, B. Neuschl, S. Bauer, Y. Wu, S. Chakraborty, N. Hibst, S. Strehle, T. Weil, K. Thonke, and F. Scholz, "GaInN quantum wells as optochemical transducers for chemical sensors and biosensors", *IEEE J. Sel. Top. Quantum Electron.*, vol. 23, pp. 1900109-1-9, 2017.
- [15] Visualization of PDB ID: 4V1W, C. Russo, and L. Passmore, "Ultrastable gold substrates for electron cryomicroscopy", *Science*, vol. 346, pp. 463-468, 2014, visualized with The PyMOL Molecular Graphics System, Version 1.7 Schrödinger, LLC.
- [16] M. Brinkley, "A brief survey of methods for preparing protein conjugates with dyes, haptens and crosslinking reagents", *Bioconjugate Chem.*, vol. 3, pp. 2-13, 1992.

Optimizing InGaN Heterostructures for High Biosensitivity: Simulations Versus Experiments

Martin F. Schneidereit and Dominik Heinz

In this work, the optimisation of indium gallium nitride (InGaN) heterostructures towards high biosensitivity is presented. Potential changes on the surface of InGaN heterostructures lead to a shift in wavelength and intensity of the photoluminescence (PL) signal of an InGaN quantum well (QW) positioned close to the surface. The semiconductor software nextnano is used to simulate various parameters to find the ideal background doping, QW position and thickness. For live sensing experiments, a new setup with horizontal sample positioning is introduced to enable reproducible verification of the simulation results.

1. Introduction

Gallium nitride (GaN) is widely known for its use in LEDs and, more recently, in high-electron mobility transistors (HEMTs) [1, 2]. With its chemical inertness and stability it is ideal for the use in biological and chemically harsh surroundings [3–6]. The photoluminescence (PL) signal of InGaN quantum well (QW) heterostructures is sensitive to electrical fields within the QW such, that a wavelength emission shift as well as an intensity change can be observed for varying fields present in the QW (quantum-confined Stark effect, QCSE). This effect can be used to detect surface potential changes (compare Fig. 1): due to near-surface band bending, surface potential changes induce electric fields within a QW located close to the surface. Due to this field, wavefunctions from both electrons and holes get more separated for higher internal fields and show reduced separation for lower internal fields. The separation on one hand determines the overlap and thus recombination probability/PL intensity of the exciton. On the other hand, both electrons and holes have their effective recombination energy decreased for higher separation. The surface potential change is thus translated into a PL wavelength shift. It has been shown by several groups (including our own) that InGaN heterostructures can be used for sensing [5, 7, 8].

In order to achieve a maximum response from the QW structure, various sample parameters can be changed and thus optimized. To reduce time and cost for such growth series, simulations are performed with nextnano.

2. Experimental Setup

In order to obtain an undisturbed read-out signal, backside excitation through the substrate is essential. Double-side polished (DSP) sapphire wafers are thus used for the epitaxy of the heterostructures. The setup described in the following can be seen in Fig. 2:

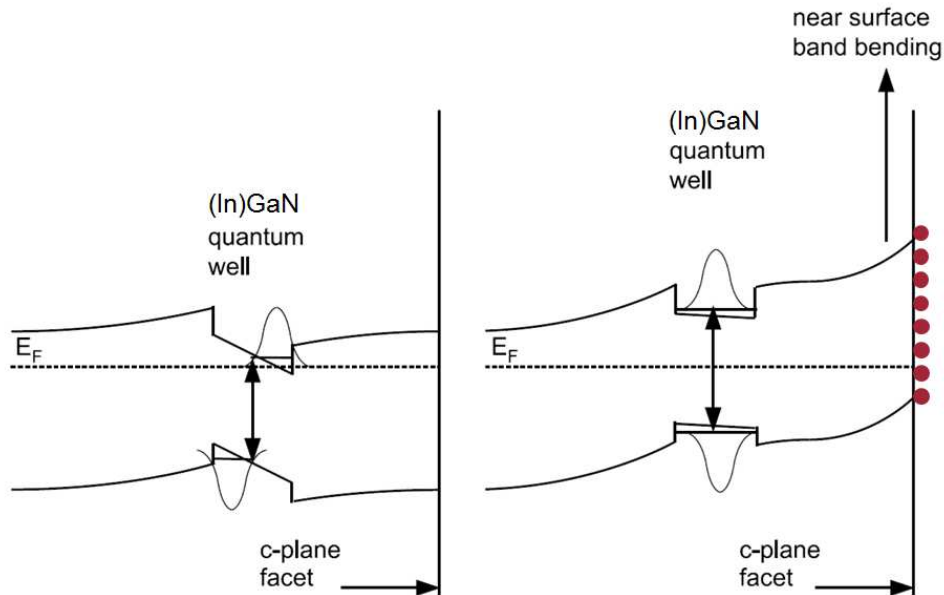


Fig. 1: Sensor principle schematic: for an undisturbed/virgin surface (left), the surface potential is only tilted due to the piezofield of the QW. For adsorbed molecules, the surface potential is shifted (right), resulting in a near-surface band bending which leads to shift in the effective QW recombination energy: surface potential change is translated into QW emission shift.

for live sensing, the sample surface should be horizontal in order to enable application of liquids from the top. In order to measure the spectral shift directly, the spectrum of the QW with an untreated surface is recorded. Then, the molecules are added to the surface via a pipette and the shifted spectrum is recorded. This is done in order to eliminate spectral changes due to inhomogeneities of the heterostructure itself. From the relative position of the peaks, the wavelength shift in nm can be determined, all spectra are normalized for better comparability. To exclude (complete) laser absorption within the GaN bulk material and to excite only the QW, a 405 nm laser is used which has its energy below the bandgap of GaN. The laser beam is coupled into the beamline of the optical setup via a dichroic beamsplitter which reflects the laser but transmits the PL signal. The transmission spectrum of the filter can be seen in the inset of Fig. 2. The beam is then focussed onto the InGaN heterostructure to excite the QW. The PL signal is collected and collimated by the same lens located below the sample. This is done to keep the top side free for adding of sensing liquids. The collimated PL signal is transmitted through the beamsplitter and then reflected by a silver mirror to be focused into the spectrometer unit.

3. Simulation with nextnano

The heterostructures which are grown by metalorganic vapor phase epitaxy (MOVPE) have to be optimized for optical sensing. To maximize the spectral shift originating from the QCSE, various parameters can be adjusted, including: QW thickness, cap layer

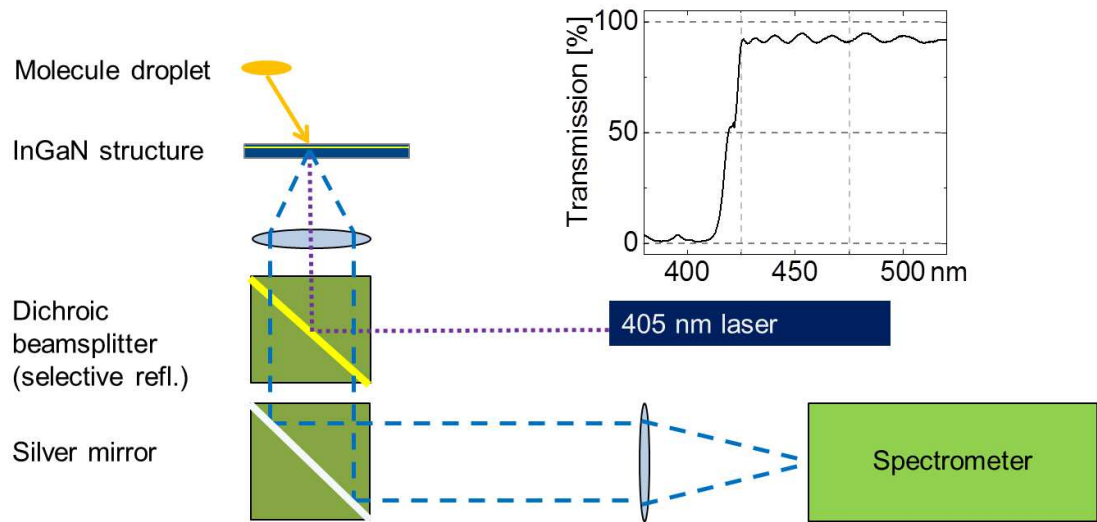


Fig. 2: The setup for live sensing experiments. The beam of a 405 nm laser is coupled into the optical readout beam line via a dichroic beamsplitter (transmission spectrum, see inset) and then focused onto the InGaN structure from the backside. The PL signal is then also collected from the backside and passes the dichroic filter where it gets reflected by a silver mirror. The collimated signal is then focused into a spectrometer unit. In order to perform live sensing, a PL spectrum of the structure is recorded and subsequently the test substance is added from the top. The PL emission shift can then be directly observed.

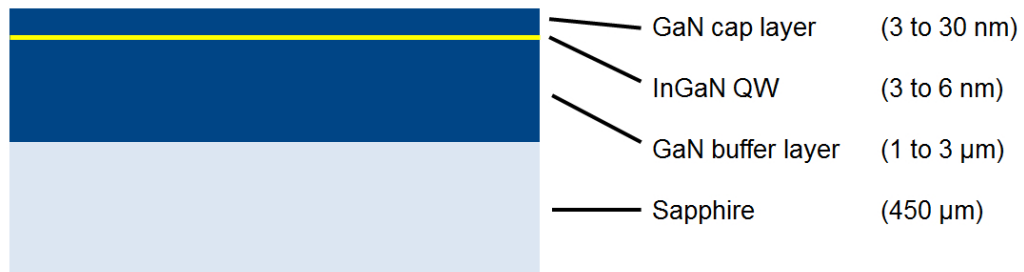


Fig. 3: Schematic of a standard QW heterostructure. The GaN buffer layer (thickness 1–3 μm) is grown on a sapphire substrate of 450 μm . On the buffer layer, a 3–6 nm InGaN layer is grown, which is followed by a GaN cap layer of 3–30 nm. The InGaN embedded between the GaN layers forms the quantum well.

thickness, background doping concentration, indium concentration within the QW (see Fig. 3 for reference). The tool used for these simulations is nextnano, which is an advanced semiconductor device simulation program. nextnano performs a self-consistent solution of Poisson, Schrödinger and drift-diffusion current equations.

As a first means, the QW thickness was varied from 3 nm up to 6 nm in steps of 0.5 nm for different background doping concentrations. It is expected that for a thicker quantum well, the overall potential difference in the QW increases and thus leads to an increased QCSE. This in turn increases the wavelength shift and thus the sensitivity for the given heterostructure. The results are indicated in Fig. 4. With larger thickness, an increased

wavelength shift could be observed from a predefined surface potential shift. The potential shift was chosen to be 0.6 eV as this is the order of magnitude that can be expected from biomolecules. With increasing thickness however, the separation between electron and hole wavefunctions increases linearly, thus reducing their overlap exponentially. This leads to a reduced recombination rate by up to a factor of ≈ 1000 . This means that a trade-off has to be met between sensitivity (i.e., the amount of wavelength shift) on one hand and signal intensity, which is related to the recombination rate, on the other. For intermediate thicknesses, high background doping concentrations seem to be desirable.

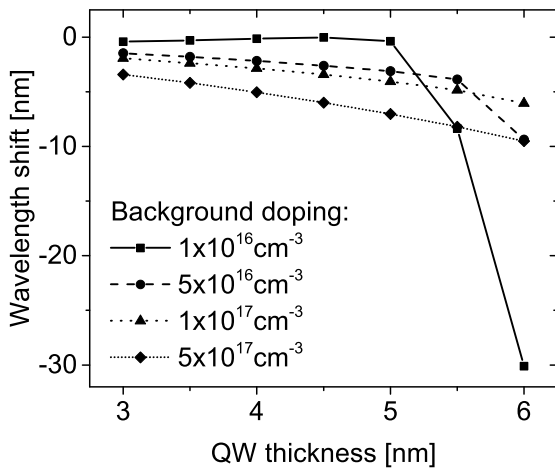


Fig. 4: Wavelength shift versus QW thickness. The dotted curves represent different n-doping concentrations: for higher doping, even thin QWs exhibit an increased shift.

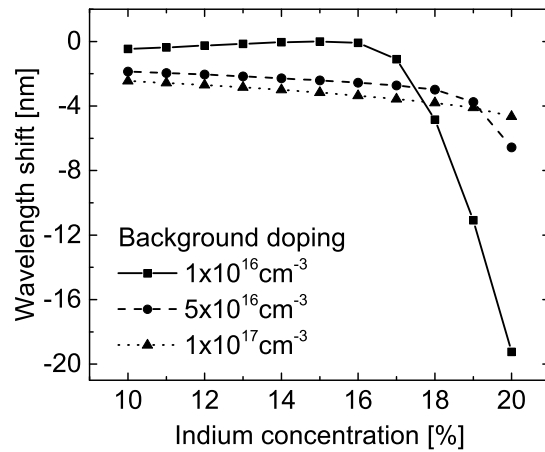


Fig. 5: Wavelength shift versus indium content in the QW. The dotted curves represent different n-doping concentrations: higher doping increases the shift for even low indium content.

The second parameter varied in the simulations was the indium content in the InGa_N QWs, again with various background doping concentrations. Considerations were the same as for the QW thickness: with higher indium concentration, strain is increased, as is the QCSE. The simulations confirm these expectations: higher indium concentration leads to a considerably increased sensitivity for low background doping, while for higher doping, the effect is not as prominent (see Fig. 5). The drawback of high indium concentrations (similar to higher QW thicknesses) is that the wavefunction separation increases and leads to reduced signal intensity. For intermediate indium content, again, higher background doping seems to be desirable.

The last parameter that was considered is the positioning of the QW within the GaN bulk, i.e., its position relative to the surface. The barrier between the surface and the QW is called the cap layer. The sensor principle is based on the change of the QCSE which is induced by free carriers within the material. Depending on the background doping, the penetration of the surface band bending into the material happens within few to several hundreds of nanometers. From first considerations done in [9], the higher the field in the QW, the more sensitive it reacts to small potential changes. In the simulations performed, the trend is perfectly clear: highest sensitivity is achieved for QWs positioned close to the surface and for the maximum local field, high doping is needed (see Fig. 7). This matches

well with the previous considerations of higher background doping being advantageous for higher sensitivity. The simulations for 3 nm showed numerical problems and were not included in Fig. 7.

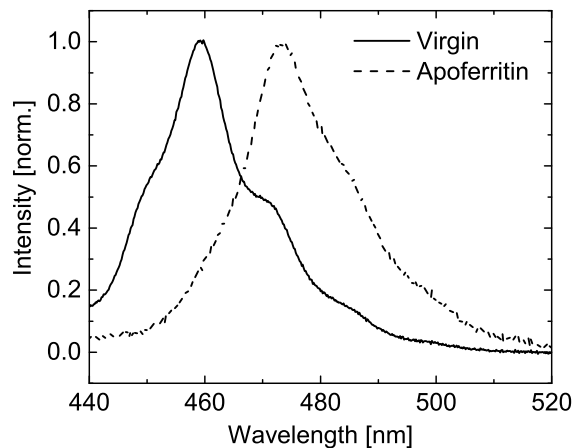


Fig. 6: Representative PL spectra for apoferritin: the virgin surface PL signal was undergoing a red-shift when apoferritin (solved in DI water) was added on top. The observed red-shift was 17 nm for a QW thickness of 3 nm and a cap layer of 3 nm.

4. Comparison Between Simulations and Measurements

With the setup described above, live measurements are possible and thus, first results could be obtained from sensing in liquid environments. As exemplary biomolecules, solutions of ferritin and apoferritin² have been prepared by S. Chakraborty et al.³. Ferritin is a macromolecule related to the iron household of the human body. Within its hollow core, it can store Fe^{2+} ions and release them at a desired position within the bloodstream [10]. The ferritin concentration in the blood is an indicator for various health conditions, such as chronic anemia [11]. With our sensor structure we want to detect the iron content of ferritin itself, which is expected to be an even superior biomarker for further diseases such as Alzheimer's disease [12]. For first analysis, the influence of the biosolvent on the surface potential was investigated. The intrinsic wavelength shift of the biosolvent has to be taken into account for an exact determination of the molecule's concentration later on. The shift is determined by analyzing and comparing the spectra of the virgin surface versus the surface with added molecules/liquids. An exemplary apoferritin analysis can be seen in Fig. 6. While deionized (DI) water did not show any spectral shift, toluene showed a spectral shift of 4.4 nm (both see Fig. 9). DI water is used as solved for pure ferritin and apoferritin, while toluene is used for later stages of the experiments.

The next step was to analyze the molecules themselves (see Fig. 10): ferritin and apoferritin were analyzed for different cap layer thicknesses⁴ to compare with the results

²Apoferritin is ferritin depleted of iron.

³Institute of Organic Chemistry III, Ulm University

⁴Samples with cap layers > 9 nm had faulty growth runs and could not be investigated.

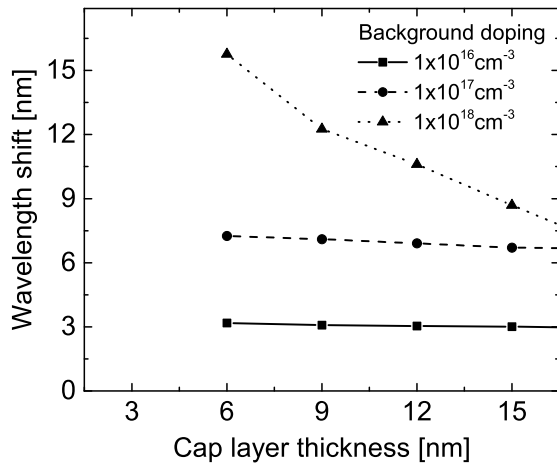


Fig. 7: Wavelength shift vs. cap layer thickness for various doping concentrations. Thin cap layers show the strongest shift and with high doping, the response maximizes.

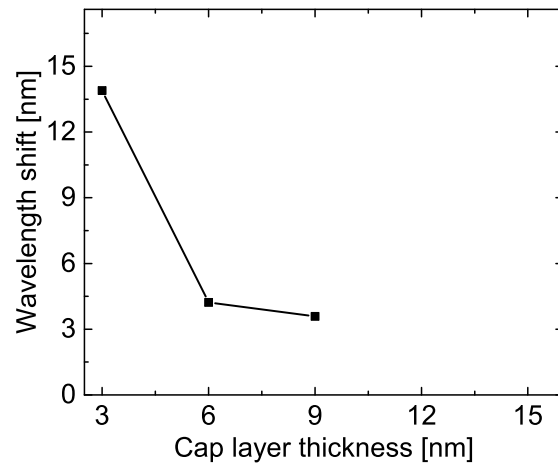


Fig. 8: Measurements of three samples with different cap layer thicknesses. From the simulations the doping concentration is concluded to be around $0.5 \cdot 10^{17} \text{cm}^{-3}$.

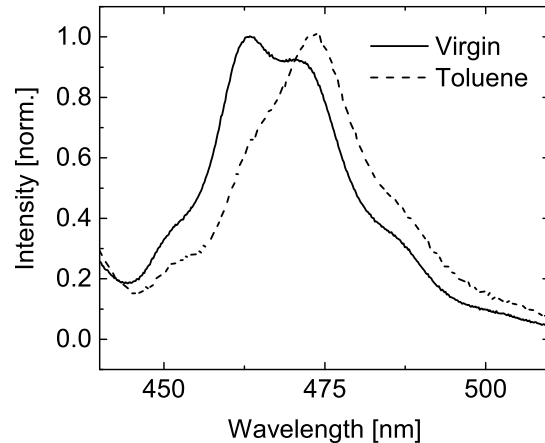
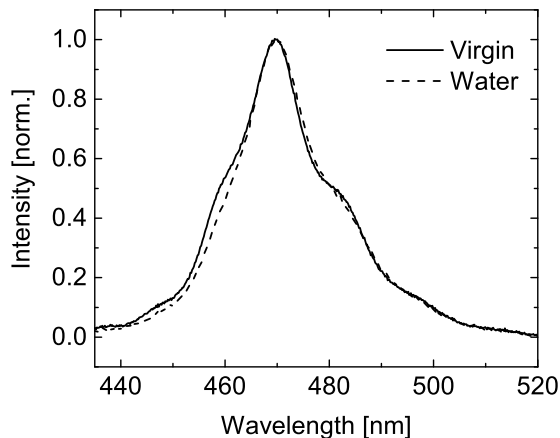


Fig. 9: Spectral shifts of biosolvents: DI water (left) did not lead to any spectral shift of the PL signal. For toluene (right), a spectral red-shift of 4.4 nm can be observed.

discussed in Sect. 3. The results were mostly as expected: for the thinnest cap layer, the sensing shift was highest, whereas for thicker cap layers the shift reduced (see Fig. 8). When compared to the simulations in detail, the results point to a background doping concentration of $\approx 0.5 \cdot 10^{17} \text{cm}^{-3}$, which is reasonable for MOVPE growth with unintended background doping from contaminants. In order to better determine the shift in surface potential due to the adsorption of apoferritin, the simulations were used to approach the observed shift by assuming various surface potential changes. The results can be seen in Fig. 11: due to the observed wavelength shift, a surface potential change of -1.6eV is concluded. This is higher than expected, errors might arise from donor concentration which was assumed to be $\approx 1 \cdot 10^{16} \text{cm}^{-3}$ but is possibly higher (compare results above). All in all, the simulations match well with the expected result, even though uncertainties remain about exact surface starting potential and induced shift by the biomolecules.

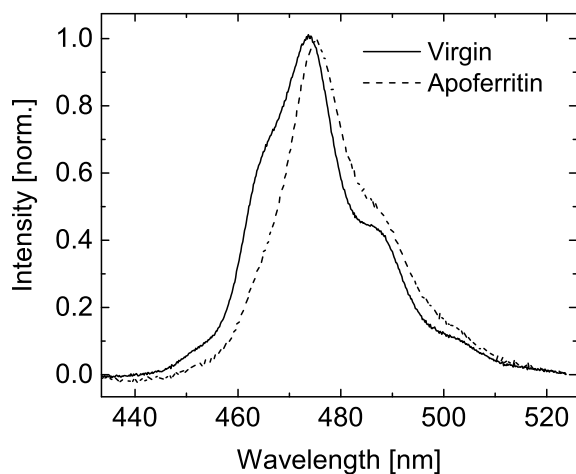


Fig. 10: Comparison between measurement and simulation for apoferritin sensing: the observed red-shift was 3.5 nm for a QW thickness of 3 nm and a cap layer of 9 nm.

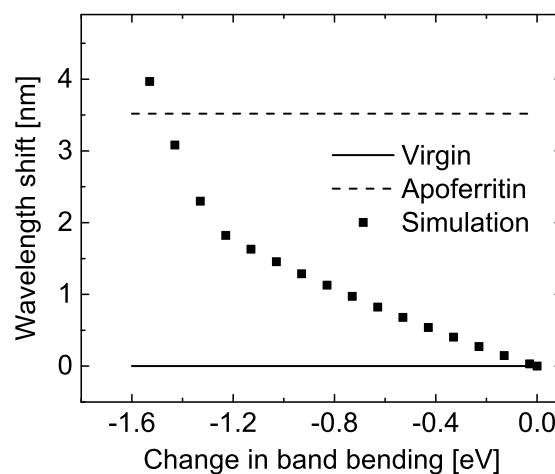


Fig. 11: QW simulations for Fig. 10: for the given sample, the surface potential was changed and the resulting wavelength shift was compared to the measurement. The matching potential change was -1.6 eV.

5. Summary

In conclusion, a setup for horizontal excitation is demonstrated, enabling live sensing experiments on fixed sample positions. These live sensing results are used to better understand the sensing behaviour of InGaN QW heterostructures and to confirm the results found in [7]. They are also compared to the simulations done in nextnano, which have been performed in order to optimize the heterostructure design parameters to achieve maximum biosensitivity. With both, simulations and experiments, further QW samples will be improved to come closer to our final goal of realising medical sensors for biomolecules.

Acknowledgment

Scientific support by J. Shabaz (Institute of Optoelectronics, Ulm University), F. Huber, S. Bauer, B. Hörbrand, K. Thonke (Institute of Quantum Matter / Semiconductor Physics Group, Ulm University), S. Chakraborty, N. Naskar and T. Weil (Institute of Organic Chemistry III, Ulm University) is gratefully acknowledged. This work was financially supported by the Baden-Württemberg Stiftung gGmbH within the project: “Intelligente optoelektronische Biosensoren”.

References

- [1] N. Koide, H. Kato, M. Sassa, S. Yamasaki, K. Manabe, M. Hashimoto, H. Amano, K. Hiramatsu, and I. Akasaki, “Doping of GaN with Si and properties of blue m/i/n/n⁺ GaN LED with Si-doped n⁺-layer by MOVPE”, *J. Cryst. Growth*, vol. 115, pp. 639–642, 1991.

- [2] R.S. Pengelly, S.M. Wood, J.W. Milligan, S.T. Sheppard, and W.L. Pribble, “A review of GaN on SiC high electron-mobility power transistors and MMICs”, *IEEE Trans. Microw. Theory Techn.*, vol. 60, pp. 1764–1783, 2012.
- [3] I. Yonenaga, “Thermo-mechanical stability of wide-bandgap semiconductors: high temperature hardness of SiC, AlN, GaN, ZnO and ZnSe”, *Physica B: Condensed Matter*, vol. 308–310, pp. 1150–1152, 2001.
- [4] K.-A. Son, A. Liao, G. Lung, M. Gallegos, T. Hatake, R.D. Harris, L.Z. Scheick, and W.D. Smythe, “GaN-based high-temperature and radiation-hard electronics for harsh environments”, in *Micro- and Nanotechnology Sensors, Systems, and Applications II*, T. George, M.S. Islam, and A.K. Dutta (Eds.), Proc. SPIE 7679, pp. 76790U-1–8, 2010.
- [5] S. Pearton, B. Kang, S. Kim, F. Ren, B. Gila, C. Abernathy, J. Lin, and S. Chu, “GaN-based diodes and transistors for chemical, gas, biological and pressure sensing”, *J. Phys. Condens. Mat.*, vol. 16, p. R961–R994, 2004.
- [6] I. Cimalla, F. Will, K. Tonisch, M. Niebelschütz, V. Cimalla, V. Lebedev, G. Kittler, M. Himmerlich, S. Krischok, J. Schaefer, M. Gebinoga, A. Schober, T. Friedrich, and O. Ambacher, “AlGaIn/GaN biosensor-effect of device processing steps on the surface properties and biocompatibility”, *Sens. Actuators B*, vol. 123, pp. 740–748, 2007.
- [7] D. Heinz, F. Huber, M. Spiess, M. Asad, L. Wu, O. Rettig, D. Wu, B. Neuschl, S. Bauer, Y. Wu, S. Chakraborty, N. Hibst, S. Strehle, T. Weil, K. Thonke, and F. Scholz, “GaInN quantum wells as optochemical transducers for chemical sensors and biosensors”, *IEEE J. Sel. Topics Quantum Electron.*, vol. 23, pp. 1–9, 2017.
- [8] S. Paul, A. Helwig, G. Müller, F. Furtmayr, J. Teubert, and M. Eickhoff, “Optochemical sensor system for the detection of H₂ and hydrocarbons based on In-GaN/GaN nanowires”, *Sens. Actuators B*, vol. 173, pp. 120–126, 2012.
- [9] O. Rettig, *Nitridische Nanosäulen – Design und Wachstum für Sensoranwendungen*, Master Thesis, Ulm University, Ulm, Germany, 2014.
- [10] Y. Ren and T. Walczyk, “Quantification of ferritin bound iron in human serum using species-specific isotope dilution mass spectrometry”, *Metallomics*, vol. 6, pp. 1709–1717, 2014.
- [11] G. Weiss and L.T. Goodnough, “Anemia of chronic disease”, *N. Engl. J. Med.*, vol. 352, pp. 1011–1023, 2005.
- [12] P.D. Sole, C. Rossi, M. Chiarpotto, G. Ciasca, B. Bocca, A. Alimonti, A. Bizzarro, C. Rossi, and C. Masullo, “Possible relationship between Al/ferritin complex and Alzheimer’s disease”, *Clinical Biochemistry*, vol. 46, pp. 89–93, 2013.

Gas Sensing Using InGaN Quantum Wells

Jassim Shahbaz

Chemical stability and inertness of GaN and InGaN make them suitable candidates for gas and biosensing applications in chemically harsh environments. Unlike conventional III-nitride based sensors with electrical readout, we focus on heterostructures which can be read out purely by their photoluminescence signal remotely. These semiconductors are particularly sensitive to changes in surface charges. In this initial study, InGaN quantum wells grown on GaN buffer layers are used for gas sensing measurements and the knowledge acquired from these experiments will be applied to the development of highly sensitive optical analysis of gases present in human breath.

1. Introduction

GaN is well established as a general lighting and lasing applications semiconductor material. In recent years it has also attracted interest from the scientific community for other applications such as gas and biosensing [1–3]. The material is chemically stable and inert, has good optoelectronic properties and is biocompatible [4, 5]. For biosensing the polarity dependent piezoelectric properties are expected to be extremely useful [6]. GaN also has a large bandgap and the highest occupied and lowest unoccupied orbitals of many biomolecules match very well with it [7]. Typically gas and biosensors are electrical devices, transistors and Schottky diodes [8], in which the adsorption of molecules changes the surface Fermi level pinning and hence the electrical conductivity. A near-surface upward band bending is observed with the creation of a depletion zone for n-doped semiconductors. More complex nanostructures have also been researched due to their high surface-to-volume ratio and low power consumption. However, these structures require intricate fabrication processes and also sophisticated contacting methods. Even then the contacts are vulnerable in wet chemical environments.

III-nitride based semiconductors on the other hand can be read out optically completely avoiding the drawbacks of electrical contacting making the structures stable against destructive chemicals. The adsorbates on the surface of such structures modify the optical photoluminescence (PL) response which can be investigated remotely. In this study a label-free approach towards gas sensing is presented, with a particular focus on gases present in the human breath. The PL response of a planar near-surface InGaN quantum well (QW) with different GaN capping layer thickness in the presence of different gases is studied.

2. Experimental Details

A commercial horizontal flow metal organic vapour phase epitaxy (MOVPE) reactor Aixtron AIX200/RF is used for the semiconductor heterostructure growth. Ammonia (NH_3), trimethylgallium (TMGa), trimethylaluminum (TMAI), triethylgallium (TEGa), and trimethylindium (TMIn) are used as precursors. Nitrogen and ultra-pure hydrogen are used as carrier gases. First, a 10 nm thick AlN nucleation layer is grown on a c-oriented double-side polished sapphire wafer followed by a nominally undoped Ga-polar GaN buffer layer with a thickness of about 3 μm . Then a single 3 nm thick InGaN QW is grown with a GaN capping layer of different thickness, i.e., 3, 6, 9, 15 and 30 nm at the top (Fig. 1, left). For the optical characterisation of the QW, a micro-photoluminescence setup with a sealed chamber connected to a gas mixing apparatus was used. The changing PL spectra in response to the cyclic switching of ambient gases is continuously recorded. A HeCd laser (325 nm) is used for the excitation of the QW PL and both the optical excitation and the read-out of the PL spectra is performed from the top. A monochromator in combination with a liquid nitrogen cooled CCD camera is used to spectrally resolve and record the QW emission signal.

3. QW Photoluminescence Response to Gas Molecules

The adsorption of gas molecules on the surface influences the near-surface InGaN QW PL emission. Within the GaN bandgap the Fermi level is pinned to the surface states present in high density when no surface modification is done. For n-doped GaN in air, upward band bending of 1 eV has been reported [9] which induces a depletion zone for majority charge carriers (i.e., electrons) near the surface. The length of the depletion zone (W_d) is dependent on the carrier concentration in the bulk crystal and the surface potential as described by

$$W_d = \sqrt{(2 \cdot \epsilon_s \cdot \psi_s) / (q \cdot N_d)} . \quad (1)$$

Here ϵ_s is the absolute dielectric permittivity, ψ_s is the surface potential, q is the elementary charge and N_d is the doping concentration [10]. Figure 1 (right) shows the energy band diagram of an n-type semiconductor with upward band bending resulting in the depletion of electrons and accumulation of holes in the region. The QW near the surface experiences this electric field and as a consequence the effective bandgap is changed, an effect known as the quantum-confined Stark effect. Moreover, the QW grown on the polar c-plane also suffers from the internal piezoelectric fields which tilts the QW energy band in the opposite direction to the surface-induced band bending. Any adsorbate on the surface accumulating negative charges will increase the near-surface band bending for an n-doped material while on the other hand a reducing agent will have the opposite effect. So for oxidising agents a blue-shift in the emission due to the reduced tilt in the QW energy band is expected while an increase in the overlap of electron-hole wave function should also improve the radiative recombination probability.

The QW should be positioned in the region with a large potential gradient, i.e., close to the surface, for maximal spectral shift. However, due to lowering of the barrier height, there is an increased probability of the carriers tunnelling out of the QW and non-radiatively

recombining at the surface or in the bulk. This could potentially lead to a loss in the PL intensity. Under these circumstances a compromise might be necessary between high sensitivity in terms of a wavelength shift and high signal-to-noise ratio for such a sensor.

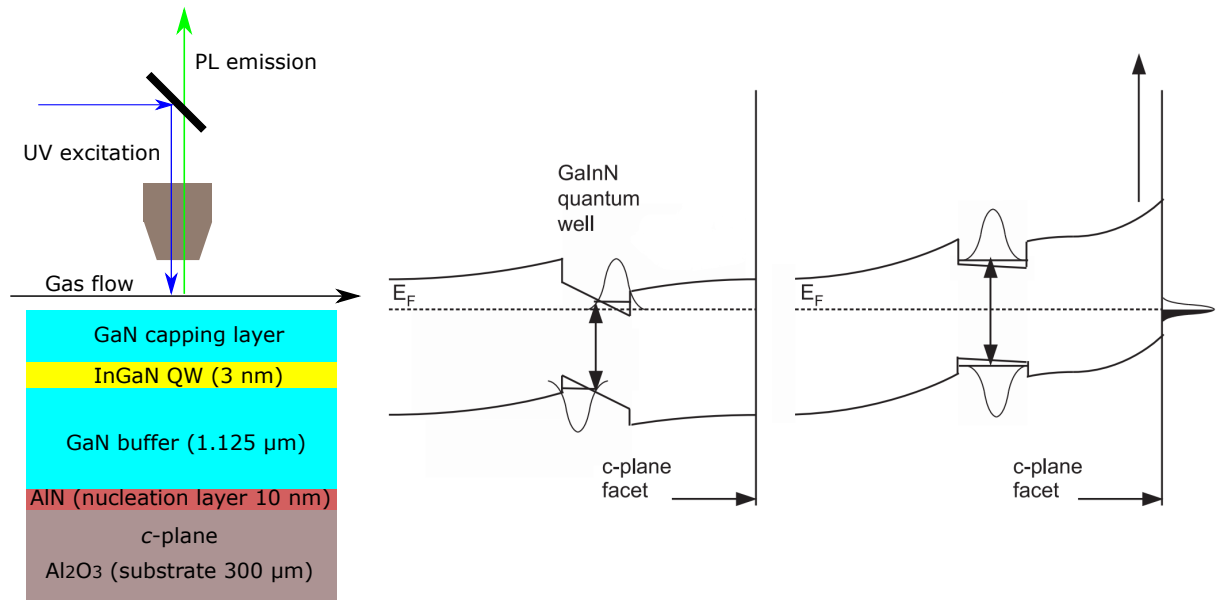


Fig. 1: Micro-PL setup schematic for front-side UV excitation of the InGaN QW (left). Capping layers of different thickness were used for these measurements. Band structure for GaN/InGaN heterostructure without and with near-surface band bending after adsorption of oxidising agent (right) [1].

4. Experimental Results

Gas sensing experiments were performed using a single 3 nm thick InGaN planar quantum well. In order to investigate the influence of the capping layer thickness on the sensitivity of the sensor, layers of different thickness were grown. With the HeCd laser front-side excitation of the QW, a PL signal from the different samples is observed at around 2.6 eV. By changing the thickness of the capping layer from 3 nm to 30 nm, a blue-shift of about 90 meV is observed (Fig. 2). This shift might be a result of strong near-surface band bending compensating the internal piezoelectric polarisation effects. Another possible reason for the blue-shift is the desorption of indium during the longer capping layer growth at slightly higher temperature.

To measure the influence of surface gases on the QW emission, first nitrogen and oxygen were used and the results for PL peak energy variation are shown in Fig. 3 for two different capping layers i.e., 3 and 30 nm. Oxygen atmosphere is expected to increase the upward surface band bending and increase the overlap of the electron-hole wave function. A clear peak emission shift is visible when switching from nitrogen to oxygen and the PL intensity is also affected (not shown here). However, the sensitivity of the sensor decreases considerably after the first cycle, as is evident from the energy variation, pointing to the

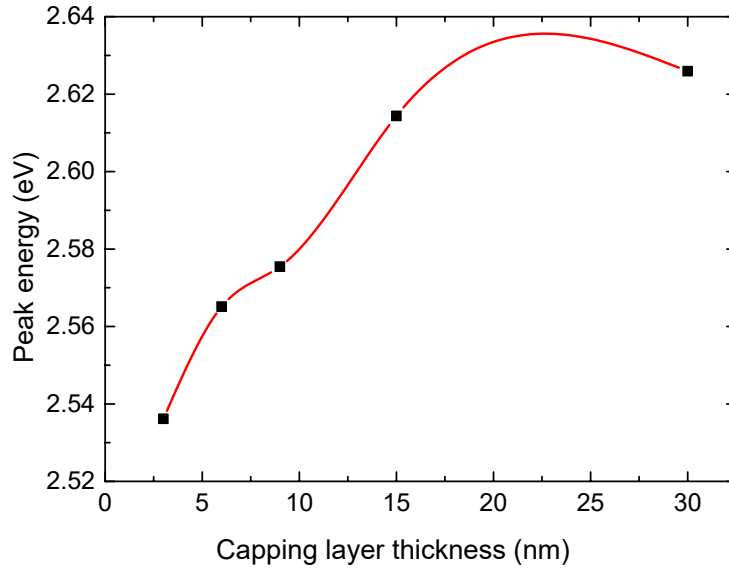


Fig. 2: Peak emission energy of InGaN QW structures with different GaN capping layer thickness, a blue-shift with increasing cap thickness is observed.

formation of an oxide layer on the surface. The thinner capping layer with 3 nm showed higher sensitivity compared to a thicker layer with 30 nm showing shifts of about 28 meV and about 0.5 meV, respectively. These results confirm simulation results presented in [11].

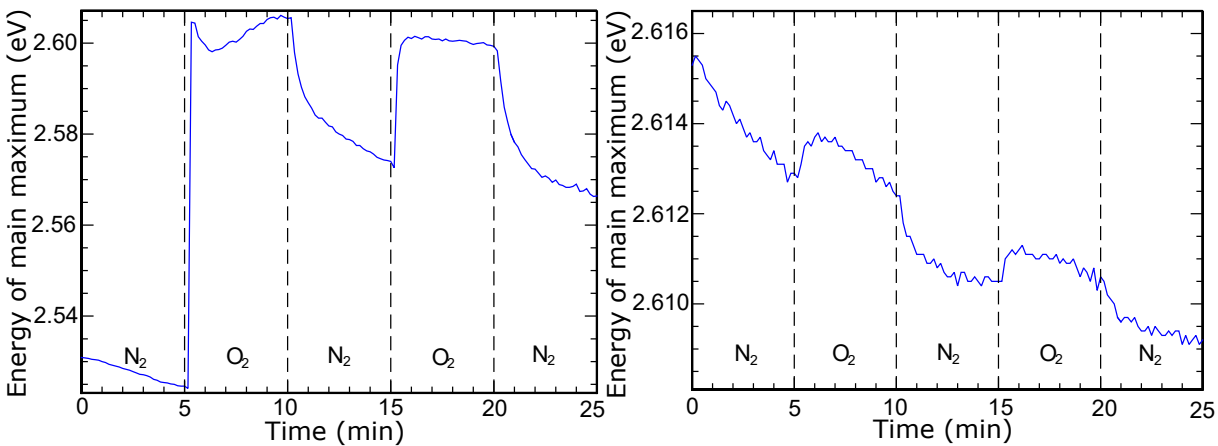


Fig. 3: Spectral shift of InGaN QW in nitrogen and oxygen when cyclically switched in 5 min intervals: 3 nm cap (left) and 30 nm cap (right).

The effect of hydrogen on the QW PL emission was also investigated. 5% hydrogen in nitrogen was switched in place of oxygen and the PL emission peak position and intensity was recorded (Fig. 4). With hydrogen adsorption on the surface a blue-shift is observed again possibly due to the increased near-surface band bending. The reduction in sensitivity due to the oxidation layer is less severe in this case compared to pure oxygen. Although the emission energy is higher in hydrogen ambient, the intensity of the signal is decreased possibly due to the tunnelling of electrons out of the QW and

increased non-radiative surface recombination processes, although further studies need to be done to investigate this phenomena. The shift in energy seemingly is a more reliable sensor response as it is a direct result of the QW band situation. However, the intensity change could be used in combination with the energy change for more complex ambient environments carrying additional information about the gas to be detected.

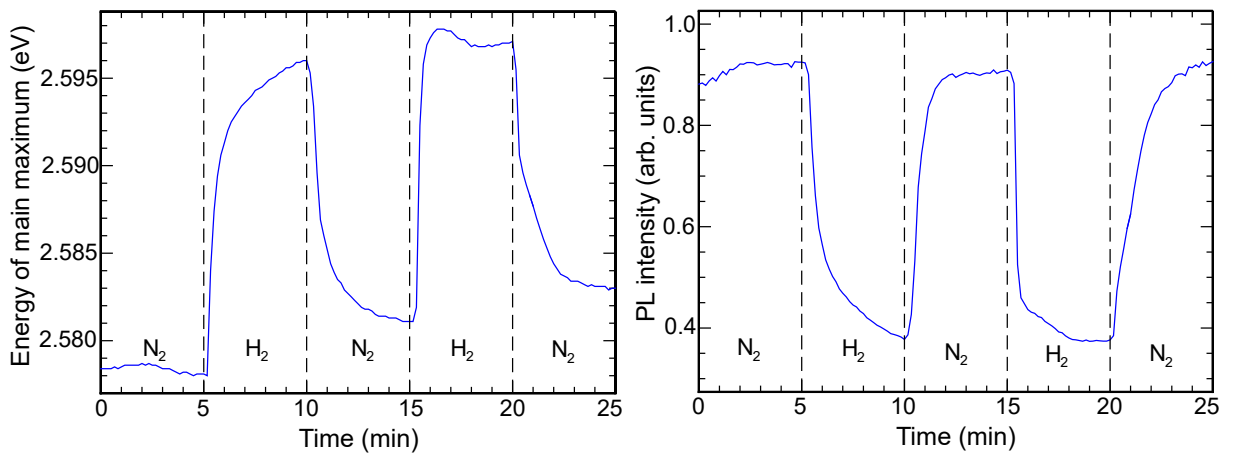


Fig. 4: (Left) Spectral shift and (right) intensity shift of an InGaN QW in nitrogen and 5% hydrogen in nitrogen when cyclically switched in 5 min intervals.

5. Conclusion

Optical transducers based on GaN/InGaN heterostructures for the detection of gases have been realized for a proof of concept. Gas molecules on the surface of such sensors induce a spectral shift of the PL emission and a change in the signal intensity with the changing of gas molecules is also observed. Oxidising agents induce a blue-shift with a decrease in PL intensity while reducing agents induce a red-shift and an increase in the PL intensity. Further work is to be done towards functionalization of the surface to improve sensitivity and selectivity. These results are promising and could be useful in the development of high-sensitivity gas sensors with optical readouts.

Acknowledgment

Scientific support by B. Hörbrand, S. Bauer, and K. Thonke (Institute of Quantum Matter/Semiconductor Physics, Ulm University) is gratefully acknowledged. This work is financially supported by the Deutsche Forschungsgemeinschaft (DFG) within the PULMOSENS project “Semiconductor-based nano structures for the highly sensitive optical analysis of gases and bio-materials”.

References

- [1] D. Heinz, F. Huber, M. Spiess, M. Asad, L. Wu, O. Rettig, D. Wu, B. Neuschl, S. Bauer, Y. Wu, S. Chakraborty, N. Hibst, S. Strehle, T. Weil, K. Thonke, and F. Scholz, “GaInN quantum wells as optochemical transducers for chemical sensors and biosensors”, *IEEE J. Select. Topics Quantum Electron.*, vol. 23, pp. 1900109-1-9, 2017.
- [2] J. Teubert, P. Becker, F. Furtmayr, and M. Eickhoff, “GaN nanodiscs embedded in nanowires as optochemical transducers”, *Nanotechnology*, vol. 22, pp. 275505-1-5, 2011.
- [3] S.J. Pearton, F. Ren, Y.L. Wang, B.H. Chu, K.H. Chen, C.Y. Chang, W. Lim, J. Lin, and D.P. Norton, “Recent advances in wide bandgap semiconductor biological and gas sensors”, *Prog. Mater. Sci.*, vol. 55, pp. 1-59, 2010.
- [4] I. Cimalla, F. Will, K. Tonisch, M. Niebelschütz, V. Cimalla, V. Lebedev, G. Kittler, M. Himmerlich, S. Krischok, A.J. Schaefer, M. Gebinoga, A. Schober, T. Friedrich, and O. Ambacher, “AlGaIn/GaN biosensor—effect of device processing steps on the surface properties and biocompatibility”, *Sens. Actuators B*, vol. 123, pp. 740-748, 2007.
- [5] S. Paul, A. Helwig, G. Müller, F. Furtmayr, J. Teubert, and M. Eickhoff, “Optochemical sensor system for the detection of H₂ and hydrocarbons based on InGaIn/GaN nanowires”, *Sens. Actuators B*, vol. 173, pp. 120-126, 2012.
- [6] Y.L. Wang, F. Ren, U. Zhang, Q. Sun, C.D. Yerino, T.S. Ko, Y.S. Cho, I.H. Lee, J. Han, and S.J. Pearton, “Improved hydrogen detection sensitivity in N-polar GaN Schottky diodes”, *Appl. Phys. Lett.*, vol. 94, pp. 212108-1-3, 2009.
- [7] M. Stutzmann, J.A. Garrido, M. Eickhoff, and M.S. Brandt, “Direct biofunctionalization of semiconductors: a survey”, *Phys. Status Solidi A*, vol. 203, pp. 3424-3437, 2006.
- [8] J. Schalwig, G. Müller, M. Eickhoff, O. Ambacher, and M. Stutzmann, “Group III-nitride-based gas sensors for combustion monitoring”, *Mater. Sci. Eng. B*, vol. 93, pp. 207-214, 2002.
- [9] M. Foussekis, A.A. Baski, and M.A. Reshchikov, “Photoadsorption and photodesorption for GaN”, *Appl. Phys. Lett.*, vol. 94, pp. 162116-1-3, 2009.
- [10] D.K. Schroder, *Semiconductor Material and Device Characterization* (3rd ed.), Tempe: Wiley-Interscience, 2006.
- [11] M. Schneidereit, “Optimizing InGaIn heterostructures for high biosensitivity: simulations versus experiments”, *Annual Report 2016*, pp. 37-44. Ulm University, Institute of Optoelectronics.

Growth and Characterization of AlGaN/AlN Heterostructures

Tomáš Hubáček[†]

In this article, we present our studies about the epitaxial growth of AlGaN quantum well (QW) structures for deep ultraviolet light emitting devices as a preparatory work for the later incorporation of boron, which is not described here. X-ray diffraction, photo- and cathodoluminescence, atomic force microscopy, and transmission electron microscopy have been used for characterization of our structures.

1. Introduction

Since few years, deep ultraviolet (UV) light emitting diodes (LEDs) based on high Al content $\text{Al}_x\text{Ga}_{1-x}\text{N}$ materials have attracted strong scientific focus due to many possible applications. Especially in the UV-C range (around 270 nm), there are many applications as sterilization and disinfection of water and air, phototherapy, medical diagnostics etc. [1, 2]. Compared to conventional deep UV sources (e.g. mercury lamps), LEDs can have lower power consumption. Being mercury-free, they are also environmentally acceptable. Moreover, they can be switched on/off much faster. Mercury lamps have a fixed emission spectrum with a narrow peak at 254 nm, while the emission wavelength of LEDs can be chosen arbitrarily from 210 nm up to the visible spectrum [3].

Although the output power of deep UV LEDs has greatly increased [4–6] in the last few years, their wall-plug efficiency is still typically less than 10 %, i.e., substantially inferior as compared to visible LEDs based on InGaN materials [7]. Our current studies concentrate on two major reasons which are blamed responsible for such low efficiency of deep UV LEDs. The first challenge is to grow high quality AlN layers with a low density of threading dislocations, which induce severe nonradiative recombination processes. The second problem is the significant lattice mismatch between layers with different Al content leading to strong pseudomorphic strain in the active QWs. This causes strong piezoelectric fields in the active layers reducing the overlap between the electron and hole wave functions, which further deteriorates the radiative recombination rate [8].

To solve the strain problem, we can use boron containing AlGaN layers in the active region. Boron nitride (BN) has an approximately 18 % smaller lattice constant compared to AlN [9]. Hence, alloying BN with Al(Ga)N opens the possibility to lattice match active layers to the AlN host material used for short wavelength LEDs. Besides leading to a reduced piezoelectric field in the active layers, lower lattice mismatch may help to reduce

[†]Tomáš Hubáček was a visiting scientist in the Inst. of Optoelectronics from Aug. 2016 until Jan. 2017. His permanent address is: Institute of Physics, Czech Academy of Sciences, Prague, Czech Republic.

strain-induced crystalline defects. Currently, only few publications about $\text{Al}_x\text{B}_y\text{Ga}_{1-x-y}\text{N}$ concerning experimental [9–14] and theoretical studies [15–17] can be found. Many fundamental properties are still unknown or uncertain. Boron is reported to have a poor solubility in AlGaN [18], but for $\text{Al}_{0.5}\text{Ga}_{0.5}\text{N}$ only 6–7% of boron is enough to compensate compressive strain with respect to AlN.

In this article, we present some preliminary results of AlGaN/AlN heterostructures with an emission wavelength around 260 nm which have been optimized for preparation of subsequent structures where B will be incorporated into the quantum wells.

2. Experimental

All structures were prepared in an Aixtron AIX-200/4 RF-S HT low-pressure horizontal MOVPE reactor, equipped with a Laytec EpiCurveTT apparatus for *in-situ* measurement of reflectivity and the true wafer temperature. Slightly mis-cut *c*-plane oriented sapphire wafers have been taken as substrates. Standard precursors (trimethylgallium, TMGa, trimethylaluminum, TMAI, and ammonia, NH_3) were used with nitrogen and hydrogen as carrier gases.

A high-resolution X-ray diffractometer (Bruker Discover D8) was used to study the crystal quality and other parameters of the heterostructures (strain, composition and layer thickness). Photoluminescence (PL) spectra were measured at low temperature (8 K) using an argon fluoride excimer laser (excitation wavelength of 193 nm). Depth-resolved scanning electron microscopy (SEM) based cathodoluminescence (CL) was measured also at $T \simeq 8$ K (SEM: 1–10 keV, spectral resolution: 7 meV/0.34 nm) [19]. Moreover, surface properties have been measured by atomic force microscopy (AFM), whereas details about the quantum wells have been observed by transmission electron microscopy (TEM).

All heterostructures were grown on 500 nm thick AlN buffer with an AlN nucleation layer [20]. We typically have grown heterostructures with 5 AlGaN QWs with a thickness of about 2 nm embedded into 8 nm thick AlN quantum barriers (QBs). First samples have been grown continuously without any interruption between template and heterostructure growth. In later experiments, we prepared full wafer AlN templates which have been used as quarter wafer substrates for the subsequent deposition of our AlGaN heterostructures to get comparable conditions for several samples. The growth on these templates was initiated with the deposition of a 100 nm thick AlN layer in order to have a perfect transition.

3. Results and Discussion

3.1 Stabilization time between barrier and quantum well growth

Forghani *et al.* [21, 22] have already investigated the growth of AlGaN layers. We started our investigations by following their recipes and growth parameters for the AlGaN layers, whereas the AlN growth was optimized at the beginning of our project. For obtaining high AlN template quality, a pulse-growth mode turned out to be beneficial where TMAI

and NH_3 were supplied separately for 2 s and 1 s, respectively. With this approach, we obtained a good crystal quality of 500 nm thick AlN templates with a full width at half maximum (FWHM) of around 40 arcsec and 1400 arcsec for the 0002 and $10\bar{1}2$ X-ray diffraction peaks, respectively. An excellent flatness of the surface could be confirmed by AFM (RMS for $10 \times 10 \mu\text{m}^2$ was 0.6 nm), which was much better than what we obtained by continuous growth of the AlN template. So we used this recipe for the growth of the buffer layers and the AlN barriers between the QWs.

Initially, some growth parameters, especially the reactor pressure and TMAI flow, were different for the quantum barrier (QB) and quantum well (QW) growth. When keeping all growth parameters and total flow during epitaxy constant and only changing the reactor pressure from QB to QW from 35 hPa to 80 hPa, respectively, we observed an increase in the surface temperature by about 18 K). This may be due to the lower gas velocity at lower pressure. Although a growth interruption of 20 s was introduced at each interface, some part of the temperature ramp was still going on during the QW growth. As the temperature may influence the Al and Ga incorporation, we introduced an additional 20 s growth interruption as stabilization time. Indeed, we observed that the QW PL peak shifted from 292 nm to 269 nm (Fig. 1) for the samples grown with this stabilization phase.

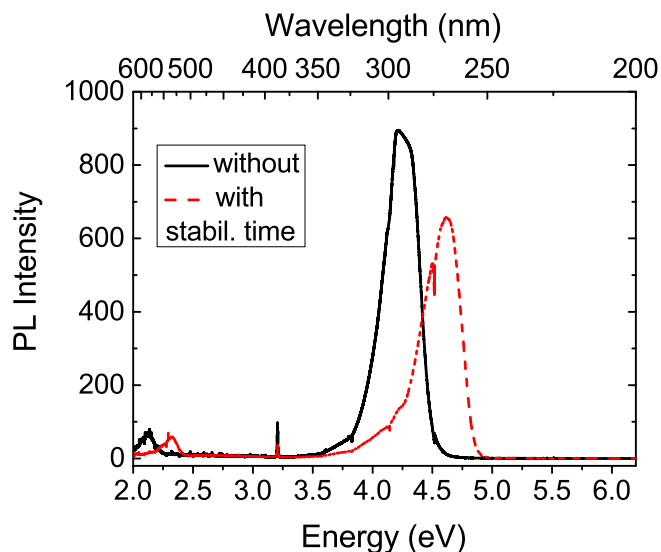


Fig. 1: PL spectrum of samples with and without stabilization time and with different TMGa flow during QW growth. The Ga flow was slightly changed by about 10% (without stab. time: $31 \mu\text{mol}/\text{min}$, with stab. time: $27 \mu\text{mol}/\text{min}$). However, this change cannot explain the large change of wavelength and hence the obvious change of composition x by more than 30%.

3.2 Different TMGa flow

In order to check the Ga incorporation at fairly high temperature (the true temperature was 1160°C), we have grown a series with different TMGa flow during the QW, keeping all other parameters unchanged. As expected, we observed a shift of the PL wavelength (Fig. 2) to higher energy for smaller TMGa flow. However, the shift was not consistent

(4 nm shift for 15 % decreased flow, 20 nm shift for 33 % decreased flow), which may be caused by some variations in the template quality in this series. Therefore, we have decided to grow our further growth series on quarter wafer templates, hence using the same template quality for 3 runs (one quarter keeping as a reference sample).

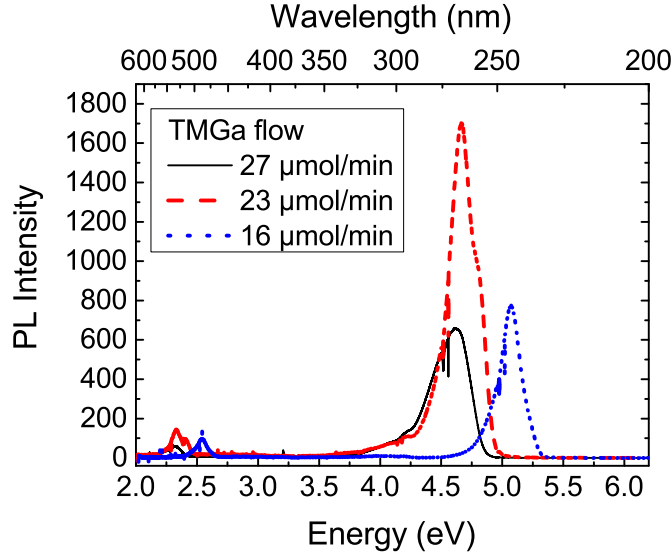


Fig. 2: PL spectrum of samples with different TMGa flow during QW growth. Samples with 5 QWs on 500 nm AlN template. All other parameters were kept constant (TMAl flow, pressure, temperature, NH₃ flow).

3.3 High-energy shoulder in PL

In the PL spectrum of the sample grown with 6 sccm TMGa flow (23 μmol/min), we observe a shoulder at higher energy (see Fig. 2). Therefore, depth-resolved cathodoluminescence [19] was done (Fig. 3) to find out whether this may be a consequence of different properties of the 5 QWs. For low acceleration voltages (probing just the upper quantum wells) we do not see the high-energy shoulder. It starts to appear for 2.5 kV primary electron voltage which probes mostly the deeper QWs. For an acceleration voltage of 4 kV, the intensity of both bands in the PL spectrum are equal. Hence these experiments obviously indicate that the first grown QWs show luminescence at shorter wavelength than the later grown QWs.

There are several possible explanations for this high-energy shoulder. On the one hand, the composition or the thickness of the QWs may be different due to some uncontrolled growth variations. Regarding a composition variation, the results would indicate an Al content of about 55 % in the first grown QWs and about 50 % in the upper QWs. On the other hand, later grown QWs could be partially relaxed, as they may have reached the critical thickness. The best measurement tool for investigation of strain in heterostructures is X-ray diffraction of asymmetric planes. Therefore, we have measured reciprocal space maps (RSM) of the (204+) plane. The main substrate peak, the zero-order peak and other satellite peaks are on the same vertical line (the same q_a value in the reciprocal space,

which is related to the a lattice parameter in real space) indicating that the structure is fully strained (no relaxation of AlGaN QWs).

Transmission electron microscopy (TEM) studies (Fig. 4) indicate a thickness of the QWs of just 2.0 ± 0.1 nm, and the QBs show 8.0 ± 0.1 nm thickness, both in fair agreement to our XRD data. Moreover, these micrographs show a fairly abrupt hetero-interface when switching from AlGaN to AlN, whereas the other interface seems to be less abrupt. Obviously, further studies are necessary to improve the abruptness of the AlN-AlGaN interface. However, these TEM micrographs confirm a uniform thickness of all QWs. Hence we conclude that the high-energy shoulder in the luminescence spectrum is caused by some composition variation in the QWs.

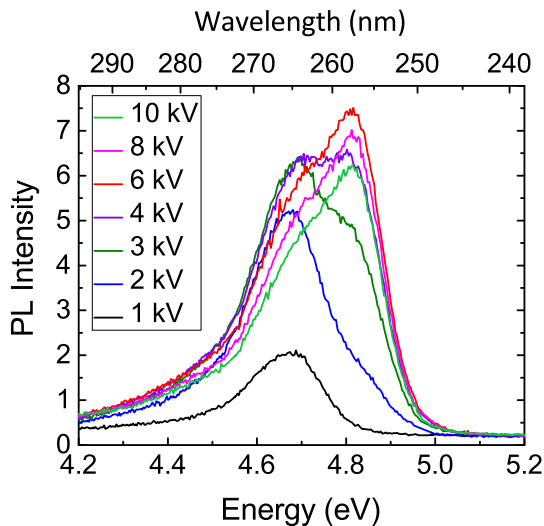


Fig. 3: Depth-resolved cathodoluminescence of sample with $31 \mu\text{mol}/\text{min}$ TMGa flow (cf. Fig. 1). The primary electron voltage was varied between 1 and 10 kV.

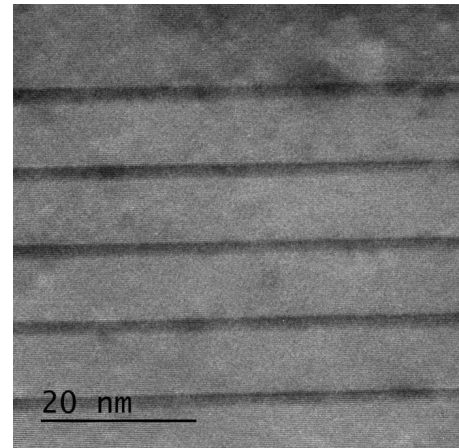


Fig. 4: TEM image of 5 QW sample (cf. Figs. 1 and 3). The QW and the QB thickness were measured to be 2.0 ± 0.1 nm and 8.0 ± 0.1 nm, respectively. Cap layer (top part of figure) thickness: 24 nm.

3.4 Different number and thickness of QWs

In a next series, we have grown some structures with 10 QWs, one with the same QW growth times as in the samples described above. In another sample, the QW growth time was reduced by about 40%. In XRD, full pseudomorphic strain for both structures could be measured confirming that even these structures did not relax because of surpassing the critical thickness. As expected, the sample with the thinner QWs showed a blue-shift of about 25 nm in PL. Particularly in the sample with thicker QWs, a similar high-energy shoulder was observed and analyzed by CL as discussed above (Fig. 5).

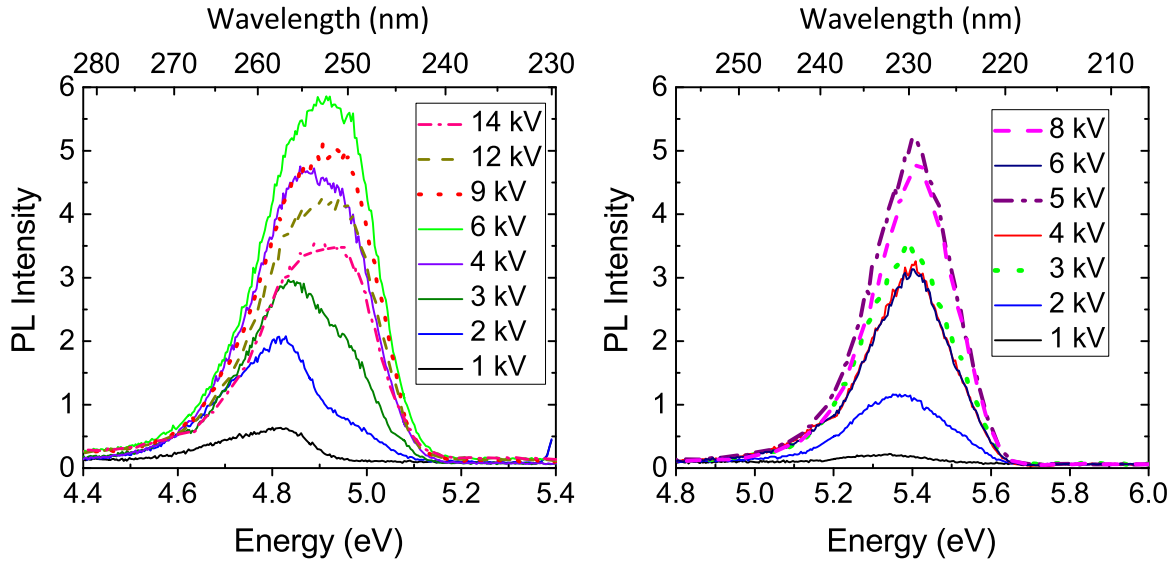


Fig. 5: Depth-resolved cathodoluminescence spectra for sample T6190 (QW growth time: 45 s; left) and T6191 (QW growth time: 27 s; right), both containing 10 QWs. Primary electron energy varied between 1 and 14 keV.

4. Conclusion

We have grown first AlGaIn/AlN QW heterostructures and tried to get good and uniform PL emission at around 260 nm. XRD and SEM-CL measurements indicate that the structures are fully strained. However, we observed a broadening of the PL signal due to a slight variation of the Ga concentration in each quantum well with more Ga found in the upper (later grown) QWs. From TEM we obtained the real thickness of the QWs which was in good agreement with our expectations. We found a significant difference in interface abruptness between QBs and QWs with the transition from AlGaIn to AlN being more abrupt.

Acknowledgment

We like to thank O. Rettig and F. Scholz from the Institute of Optoelectronics for their help and scientific support. We are grateful to K. Thonke and his group for PL and CL measurements, in particular J.-P. Scholz and M. Hocker. Moreover, our thanks go to U. Kaiser and her group for TEM measurements, in particular Y. Li. This work was financially supported by the Deutsche Forschungsgemeinschaft.

References

- [1] M. Kneissl, T. Kolbe, C. Chua, V. Kueller, N. Lobo, J. Stellmach, A. Knauer, H. Rodriguez, S. Einfeldt, Z. Yang, N. Johnson, and M. Weyers, "Advances in group III-nitride-based deep UV light-emitting diode technology", *Semicond. Sci. Technol.*, vol. 26, pp. 014036-1-6, 2011.

- [2] H. Hirayama, S. Fujikawa, N. Noguchi, J. Norimatsu, T. Takano, K. Tsubaki, and N. Kamata, “222–282 nm AlGaN and InAlGaN-based deep-UV LEDs fabricated on high-quality AlN on sapphire”, *Phys. Status Solidi A*, pp. 1176–1188, 2009.
- [3] M.S. Shur and R. Gaska, “Deep-ultraviolet light-emitting diodes”, *IEEE Trans. Electron. Dev.*, vol. 57, pp. 12–25, 2010.
- [4] M. Shatalov, J. Yang, W. Sun, R. Kennedy, R. Gaska, K. Liu, M. Shur, and G. Tamulaitis, “Efficiency of light emission in high aluminum content AlGaN quantum wells”, *J. Appl. Phys.*, vol. 105, pp. 073103-1–6, 2009.
- [5] A. Khan, K. Balakrishnan, and T. Katona, “Ultraviolet light-emitting diodes based on group three nitrides”, *Nature Photonics*, vol. 2, pp. 77–84, 2008.
- [6] A.J. Fischer, A.A. Allerman, M.H. Crawford, K.H.A. Bogart, S.R. Lee, R.J. Kaplar, W.W. Chow, S.R. Kurtz, K.W. Fullmer, and J.J. Figiel, “Room-temperature direct current operation of 290 nm light-emitting diodes with milliwatt power levels”, *Appl. Phys. Lett.*, vol. 84, pp. 3394–3396, 2004.
- [7] G.F. Yang, Q. Zhang, J. Wang, S.M. Gao, R. Zhang, and Y.D. Zheng, “Analysis of 270/290/330-nm AlGaN-based deep ultraviolet light-emitting diodes with different Al content in quantum wells and barriers”, *IEEE Photonics J.*, vol. 7 (6), pp. 1–7, 2015.
- [8] M.F. Huang and T.H. Lu, “Optimization of the active layer structure for the deep-UV AlGaN light-emitting diodes”, *IEEE J. Quantum Electron.*, vol. 42, pp. 820–826, 2006.
- [9] T. Akasaka and T. Makimoto, “Flow-rate modulation epitaxy of wurtzite AlBN”, *Appl. Phys. Lett.*, vol. 88, pp. 041902-1–3, 2006.
- [10] A.Y. Polyakov, M. Shin, W. Qian, M. Skowronski, D.W. Greve, and R.G. Wilson, “Growth of AlBN solid solutions by organometallic vapor-phase epitaxy”, *J. Appl. Phys.*, vol. 81, pp. 1715–1719, 1997.
- [11] M. Kurimoto, T. Takano, J. Yamamoto, Y. Ishihara, M. Horie, M. Tsubamoto, and H. Kawanishi, “Growth of B GaN/AlGaN multi-quantum-well structure by metalorganic vapor phase epitaxy”, *J. Cryst. Growth*, vol. 221, pp. 378–381, 2000.
- [12] X. Li, S. Sundaram, Y.E. Gmili, F. Genty, S. Bouchoule, G. Patriache, P. Disseix, F. Réveret, J. Leymarie, J.P. Salvestrini, R. Dupuis, P. Voss, and A. Ougazzaden, “MOVPE grown periodic AlN/BAIN heterostructure with high boron content”, *J. Cryst. Growth*, vol. 414, pp. 119–122, 2015.
- [13] T. Takano, M. Kurimoto, J. Yamamoto, and H. Kawanishi, “Epitaxial growth of high quality BAIGaN quaternary lattice matched to AlN on 6HSiC substrate by LP-MOVPE for deep-UV emission”, *J. Cryst. Growth*, vol. 237–239, part 2, pp. 972–977, 2002.

- [14] A. Kadys, J. Mickevicius, T. Malinauskas, J. Jurkevicius, M. Kolenda, S. Stanionyte, D. Dobrovolskas, and G. Tamulaitis, “Optical and structural properties of BGaN layers grown on different substrates”, *J. Phys. D: Appl. Phys.*, vol. 48, pp. 465307-1–6, 2015.
- [15] S.H. Park, “High-efficiency BAlGa_N/AlN quantum well structures for optoelectronic applications in ultraviolet spectral region”, *Opt. Express*, vol. 23, pp. 3623–3629, 2015.
- [16] S.H. Park and D. Ahn, “Theoretical studies on ultraviolet nearly lattice-matched BAlGa_N/BAlGa_N quantum well structures with quaternary BAlGa_N barriers”, *Jpn. J. Appl. Phys.*, vol. 55, pp. 074101-1–3, 2016.
- [17] S.H. Park and D. Ahn, “Effect of boron incorporation on light emission characteristics of UV BAlGa_N/AlN quantum well structures”, *Appl. Phys. Express*, vol. 9, pp. 021001-1–3, 2016.
- [18] C. Wei and J. Edgar, “Unstable composition region in the wurtzite B_{1-x-y}Ga_xAl_yN system”, *J. Cryst. Growth*, vol. 208, pp. 179–182, 2000.
- [19] M. Hocker, P. Maier, I. Tischer, T. Meisch, M. Caliebe, F. Scholz, M. Mundszinger, U. Kaiser, and K. Thonke, “Three-dimensional cathodoluminescence characterization of a semipolar GaInN based LED sample”, *J. Appl. Phys.*, vol. 121, pp. 075702-1–7, 2017.
- [20] J. Hertkorn, P. Brückner, S.B. Thapa, T. Wunderer, F. Scholz, M. Feneberg, K. Thonke, R. Sauer, M. Beer, and J. Zweck, “Optimization of nucleation and buffer layer growth for improved GaN quality”, *J. Cryst. Growth*, vol. 308, pp. 30–36, 2007.
- [21] K. Forghani, *Investigations on MOVPE growth of AlGa_N heterostructures for UV LED applications*, Master Thesis, Ulm University, Ulm, Germany, 2008.
- [22] K. Forghani, *Growth of AlGa_N Heterostructures for UV LED Applications*, Ph.D. Thesis, Ulm University, Ulm, Germany, 2012.

Investigation of AlBN Grown by MOVPE

Oliver Rettig

In this report, growth of boron containing layers and their characterisation will be presented. Different growth parameters are changed to investigate whether they have beneficial influence on the growth of boron containing Al(Ga)N with boron contents in the percentage regime. As template previously optimised AlN layers with a thickness of 500 nm were mainly used for overgrowth.

1. Introduction

LEDs based on GaN material already revolutionised the light market in the visible spectrum. However, current ultraviolet (UV) applications such as sterilization and disinfection of water and air [1,2], phototherapy [1], fluorescence analytical systems [2], bio-agent detection [3], spectrometry and currency validation [4] still use mercury containing lamps. Even though UV-LEDs have many advantages like their size and non-toxicity, they still suffer from external quantum efficiencies below 10 %.

Apart from carrier injection efficiency and light outcoupling, there are further important challenges in the realization of high efficiency devices. State-of-the-art AlN templates still exhibit many threading dislocations which decrease the efficiency drastically when penetrating the optically active quantum wells (QWs). They are generated as a consequence of the lattice mismatch of sapphire or silicon carbide (SiC), which are possible substrate materials, and the AlN template grown on top. Also the lattice mismatch of the AlN template and the AlGa_xN QWs leads to a significant decrease in luminescence. AlGa_xN QWs with a thickness of only a few nanometers grow strained on top of the AlN template. Due to the strong piezoelectricity of AlGa_xN-based materials, an electric field is induced in the compressively strained QWs leading to a band tilt. This results in a decrease of the overlap integral of the electrons and holes which causes a decrease in radiative recombination as well as a decrease of the effective transition energy.

By introducing boron, which is the lightest and smallest group-III element, to state-of-the-art AlGa_xN-based material systems, another degree of freedom in lattice matching can be utilised. Therefore both, template quality as well as a reduction of the quantum-confined Stark effect (QCSE) in the QWs might be achieved by the incorporation of boron. According to current scientific knowledge only 5 % of boron would be enough to lattice match AlBN on SiC.

In this work, we try to clarify whether it is possible to grow Al_xB_yGa_{1-x-y}N layers with good crystalline quality. Until now only few studies have been focussing on the growth of boron containing group-III-nitrides [5–7]. Important material properties such as the

composition dependence of the bandgap, lattice parameter for wurtzite-BN and ionisation energies of donors and acceptors are not yet known for this material. Due to its very low surface diffusion, parasitic gas phase reactions and poor solubility in AlGa_N [5], growing high quality boron containing material has not yet been achieved. By introducing high temperatures of up to 1400 °C, optimising V/III-ratio, applying indium as surfactant and precursor alternation we try to increase the surface mobility of boron. For characterisation, photoluminescence spectroscopy (PL), X-ray diffraction (XRD), scanning electron microscopy (SEM), atomic force microscopy (AFM), secondary ion mass spectroscopy (SIMS), and transmission electron microscopy (TEM) are performed to steadily increase the quality of the layers.

2. Experimental Details

The MOVPE reactor used for this study is a low-pressure horizontal reactor (Aixtron AIX-200/4 RF-S) with a high-temperature susceptor kit enabling growth temperatures up to 1400 °C. All group-III-nitrides are grown on standard (0001) sapphire substrates with an offset of 0.3° towards the m-plane. Trimethyl-aluminium (TMAI), trimethyl-gallium (TMGa), trimethyl-indium (TMIn), triethyl-boron (TEB) and ammonia are used as precursors.

For characterisation, a high resolution X-ray diffractometer (Bruker Discover D8) is used to check the crystal quality of the samples. Additionally aberration-corrected high-resolution TEM (AC-HRTEM) was performed by our project partners of the Central Facility of Electron Microscopy at Ulm University.

Photoluminescence spectroscopy is performed by using an argon fluoride excimer laser as excitation source which works at a wavelength of 193 nm. This part was supervised by the Institute of Quantum Matter, Semiconductor Physics Group at Ulm University.

3. Growth of Boron Containing AlN Layers

3.1 Growth at AlN growth conditions

Literature reports different values for the incorporation efficiency of boron in AlN [8, 9]. Therefore, first experiments were performed at standard AlN growth conditions [10] using different amounts of boron. In SEM, we found that a boron content in the gas phase larger than 2% drastically decreases the surface morphology. For TEB/III-ratios between 3% and 29%, no boron related XRD signal and a clearly visible shift of the PL defect band can be observed. In AlBN layers with higher boron content an additional defect band occurs at 4 eV which shifts even further to higher energies when increasing the boron supply. This band then dominates over the 3 eV defect band which is related to the AlN [11]. This already implies a change of growth regarding the formation of different defect types caused by boron.

In order to improve the layer quality, AlBN layers were grown with lower gas phase ratios of ~2%. XRD as well as SIMS studies were performed to determine the amount of

boron incorporated in the AlBN layers. In XRD, a weak peak was visible in some layers which would indicate a boron content of only $\sim 0.4\%$ can be calculated assuming fully relaxed layers and a c -lattice constant of 0.422 nm for w-BN [12]. Being very close to the AlN main peak at these low contents, the AlBN reflex only shows a weak response. In contrast, SIMS investigations identify 5% of boron inside the layers which is much more than indicated by XRD measurements. Therefore further characterisations of the grown layers are performed. TEM investigations reveal columnar growth of the upper part of the AlBN. Figure 1 shows a weak beam dark field (WBDF)-TEM image in $g = 11\bar{2}0$ direction of the 300 nm thick AlBN layer grown on top of an AlN template with a thickness of 500 nm .

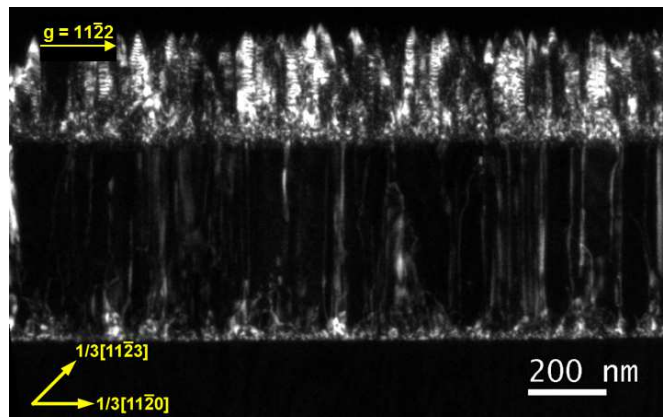


Fig. 1: WBDF image of a 300 nm thick $\text{Al}_{0.95}\text{B}_{0.05}\text{N}$ layer on top of a 500 nm thick AlN template on sapphire. For the upper part of the AlBN layer strong columnar growth can be observed.

The first $\sim 50\text{ nm}$ of the AlBN show many bright small spots, which makes it impossible to follow the threading dislocations originating from the AlN template. In the upper part of the layer, strong columnar growth can be seen with many of those columns being bright whereas others appearing dark. The width of these columns fluctuates between 20 nm and 40 nm . As WBDF images are taken with a slight angle offset from the Bragg condition, only dislocations are visible as bright lines. Since in this image many of the columns are bright it can be concluded that they are rotated around the c -axis such that the crystal does fulfil the Bragg condition. Additionally a very rough surface can be observed for the AlBN layers. The individual columns have a very sharp tip resulting in a needle-like shape.

Selective area diffraction measurements (Fig. 2) of the interface of the AlN template show a wurtzite configuration of the AlBN, which matches the template well. Performing the same measurements at the top part of the AlBN, it can be seen that the wurtzite diffraction pattern smears up by a small amount. Course approximations of the angle suggest a tilt of the c -direction of $\sim 4^\circ$.

Plan view TEM investigations of the top of the AlBN layer (Fig. 3) confirm strong columnar growth. In fact the columns do not coalesce completely to form a closed layer. In between those columns formation of amorphous material appears. Nevertheless, the diffraction pattern of the columns depicts crystallinity in wurtzite configuration. However a tilt

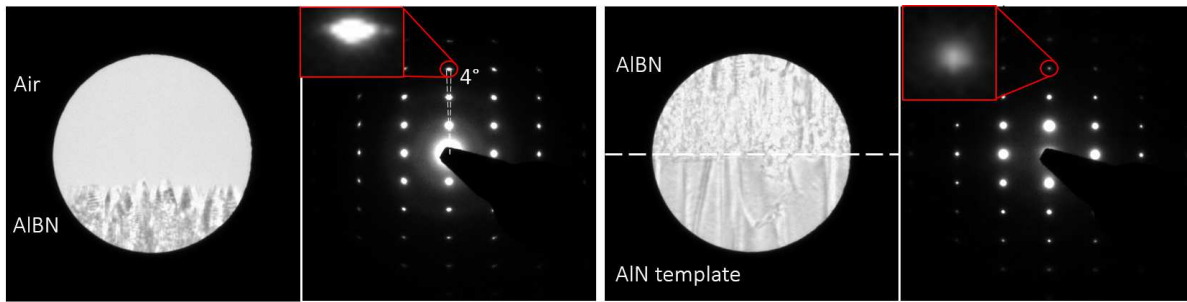


Fig. 2: Selective area electron diffraction image of the upper part of the AlBN layer with columnar growth and the interface between the AlN template and the AlBN layer. The *c*-axis of the AlBN columns at the top rotated up to 4° , whereas at the interface the lattice fits the direction of the template well.

of the columns by up to 3° around the *c*-axis can be observed. High resolution images of the coalescence region of two neighbouring columns after filtering respective lattice directions confirm the difference in lattice direction of $\sim 2^\circ$.

The presence of strong columnar growth with amorphous material enclosed might be the reason for the inconsistency in SIMS and XRD data. Accumulation of boron in the amorphous materials due to phase separation causes less boron incorporation in the AlBN columns. Therefore XRD, which reflects the composition of the columns, can only measure much lower boron concentrations than SIMS, which is sensitive for the overall presence of boron, but cannot distinguish between material incorporated in the columns and material present in the amorphous inclusions.

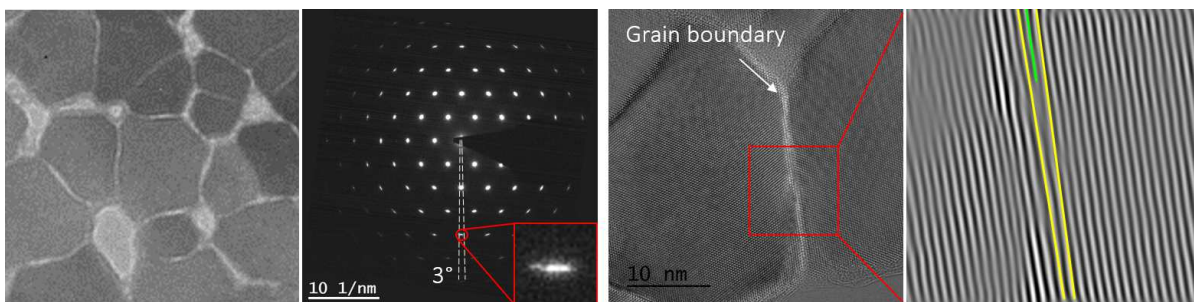


Fig. 3: Plan view TEM images and electron diffraction pattern of surface near region of the AlBN layer. A non-fully-coalesced layer of individual columns can be observed. Diffraction patterns reveal a rotation of the crystal structure around the *c*-axis of the columns by up to 3° . This behaviour can be validated by high resolution images of neighbouring columns where a tilt of $\sim 2^\circ$ is visible.

3.2 High-temperature growth series

From literature [5] and the results obtained above we conclude that the surface mobility of the boron is the main reason for columnar growth since the columns do not coalesce to

form a closed layer. Hence, further studies were performed trying to increase the mobility of the B atoms on the growing surface.

By using a high-temperature setup for our MOVPE reactor, it is possible to reach temperatures up to 1400 °C. To investigate whether high temperatures help to improve crystal growth, a series with 3 different temperatures was grown, not changing any other process parameters. Figure 4 shows PL spectra of 300 nm thick AlBN layers grown on the same 500 nm thick AlN template which is also displayed as reference.

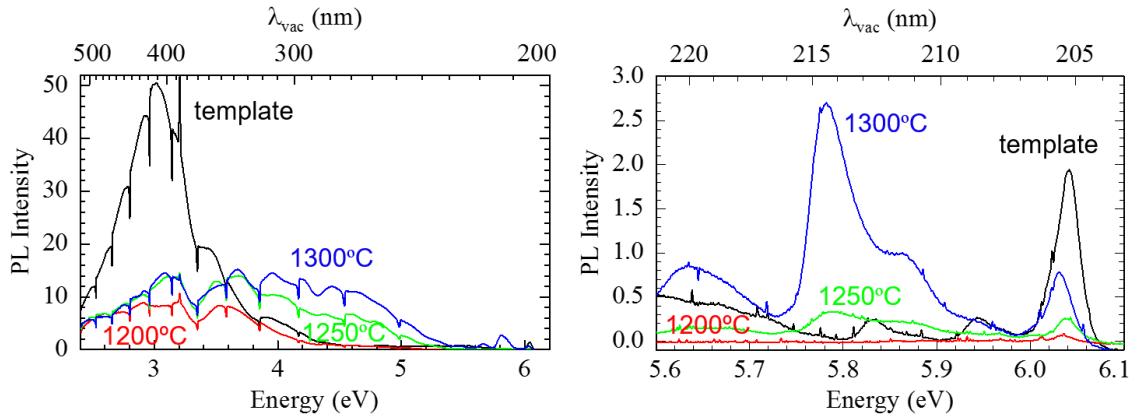


Fig. 4: Overview PL spectra of AlBN temperature series and reference template (left) and zoomed NBE region (right). With higher temperatures an additional defect band arises at around 4 eV. At high temperatures the NBE luminescence also exhibits additional contributions.

One can clearly see a drop in intensity in the defect related PL intensity when boron is supplied during growth. Moreover, a change in the respective positions of the peaks can be observed. All 3 AlBN layers still show a contribution at 3 eV which is most likely related to the AlN defect band. Additionally, a second contribution is present for all boron containing samples. Those peaks however are not appearing at the same energy for all samples. With increasing temperature the centre of the peak shifts to higher energies. At 1200 °C this peak is located at ~3 eV whereas at 1300 °C a much broader peak is visible reaching from 3.6 eV up to 5 eV. Previous studies showed a similar behaviour of the defect band when increasing the boron supply in the gas phase, leading to the conclusion that at higher temperatures more boron incorporated in the AlBN layers might be present compared to lower temperatures. However SIMS measurements revealed that more boron is incorporated in layers grown at lower temperatures. Again it has to be considered that this does not necessarily mean an increase in boron incorporation in the crystalline parts of the layers.

In the near-band-edge (NBE) region the PL spectra of the AlBN layers differ significantly. Whereas the layer grown at 1200 °C shows almost no NBE luminescence, different major contributions are visible in the spectra of the samples grown at 1300 °C surface temperature. The latter shows much stronger AlN-related band-edge luminescence. Additionally, a very strong peak arises at 5.8 eV. For this peak, different origins are possible. When considering bandgap bowings reported in literature [13] a boron content below 5% can

lead to a decrease in the bandgap energy by up to 300 meV which is in good agreement with the data received by SIMS investigations. However bowing parameters as well as band-edge energies of wurtzite BN are still not well known and contradictory discussed in literature due to its unstable nature. Another possible origin of this contribution is the presence of hexagonal BN. Due to phase separation at higher temperatures BN might grow in its initially more stable hexagonal phase. As discussed in [14], an indirect bandgap of h-BN with the longitudinal and acoustic phonon transitions present at energies possibly related to $\text{Al}_{0.95}\text{B}_{0.05}\text{N}$. The strong PL peak at ~ 5.8 eV in Fig. 4 might be related to optical phonons. The acoustic phonons should have a contribution at ~ 5.86 eV, which fits well with our PL data. The respective ratios between acoustic and optical phonons should be constant for all samples. This, however, could not be verified for additional grown layers runs, indicating that this peak might be related to other phenomena. TEM diffraction patterns of the hotter grown layers, which are not displayed here, reveal that the wurtzite crystallinity of the previous layers (see Fig. 2) cannot be maintained. Therefore it has to be assumed that at higher temperatures, phase separation is preferred over the incorporation in AlN, leading to other possible phases like h-BN or amorphous growth.

3.3 Reduction of boron supply

With the goal to achieve growth of a closed layer without having strong columnar features present, a further decrease in boron content in the gas phase was performed. Boron contents reported here arise from the assumption of linear incorporation with gas phase supply, starting at boron contents known from our previous SIMS investigations. A growth temperature of 1170 °C was chosen in order to suppress the additional NBE contributions observed in Sect. 3.2.

It is clearly visible that changing the boron supply does not affect the shift of the NBE peak. Only the intensity of the peaks increases by the reduction of boron. The small down-shift in energy of the band edge might be related to the boron incorporated in the AlBN layers. Again utilising bowing parameter values reported in literature [13], this shift would be related to approximately 0.4% of boron in AlN. However those values are still vague due to the scarce literature available for boron containing III-nitrides. Nevertheless, from the position of the band edge being constant for all boron contents, it could be concluded that the solubility limit of boron in AlN is reached for respective growth conditions. This assumption would also fit with previous investigations of strong columnar growth and amorphous material grown between the columns. Excessive boron which cannot be incorporated in AlN accumulates and forms amorphous clusters.

4. Summary

First studies on the growth of boron containing AlN layers were performed. $\text{Al}_{0.95}\text{B}_{0.05}\text{N}$ was grown with strong columnar growth as well as growth of amorphous material could be observed. The columns show wurtzite configuration in TEM investigations. From our studies we conclude that phase separation might be caused by exceeding the solubility of boron in AlN.

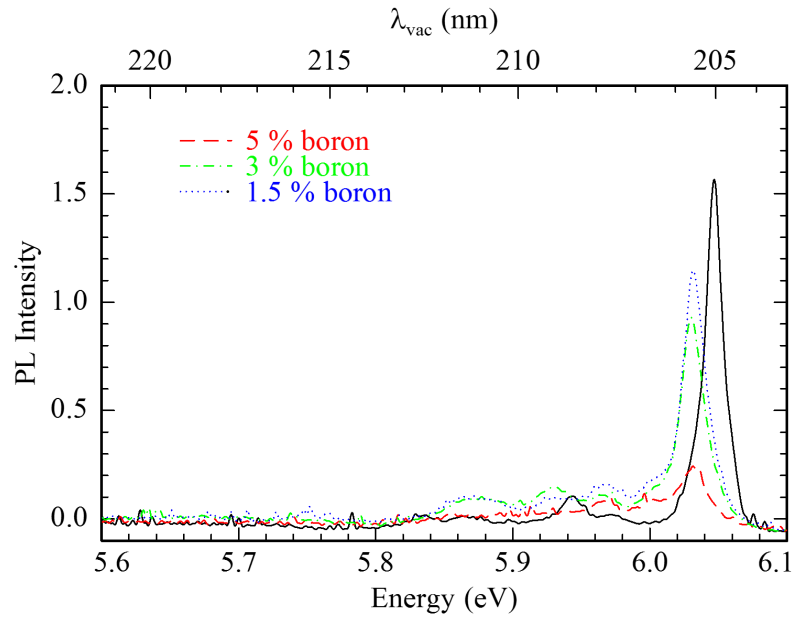


Fig. 5: NBE PL spectra of AlBN boron series and their template as reference. The amount of boron between 1.5% and 5% supplied during growth, does not affect the shift of the band edge related peak.

Therefore, more experiments are currently planned to decrease the boron content further to reach a concentration that is still below the solubility limit. Additionally, by optimising the growth conditions, we try to increase it further.

Acknowledgment

I thank the coauthors J.-P. Scholz, S. Bauer, M. Hocker, and K. Thonke of the Institute of Quantum Matter, Semiconductor Physics Group at Ulm University, Y. Li, H. Qi, J. Biskupek, and U. Kaiser of the Central Facility of Electron Microscopy at Ulm University, and T. Hubáček of the Institute of Physics, Czech Academy of Sciences, Prague, Czech Republic for their scientific support. This work was financially supported by the DFG within the framework of the project “Investigations on the epitaxy of AlBGaN heterostructures for applications in UV-LEDs”.

References

- [1] M. Kneissl, T. Kolbe, C. Chua, V. Kueller, N. Lobo, J. Stellmach, A. Knauer, H. Rodriguez, S. Einfeldt, Z. Yang, N.M. Johnson, and M. Weyers, “Advances in group III-nitride-based deep UV light-emitting diode technology”, *Semicond. Sci. Technol.*, vol. 26, pp. 014036-1–6, 2011.

- [2] H. Hirayama, S. Fujikawa, N. Noguchi, J. Norimatsu, T. Takano, K. Tsubaki, and N. Kamata, “222–282 nm AlGa_N and InAlGa_N-based deep-UV LEDs fabricated on high-quality AlN on sapphire”, *Phys. Status Solidi A*, vol. 206, pp. 1176–1182, 2009.
- [3] X. Hu, J. Deng, J.P. Zhang, A. Lunev, Y. Bilenko, T. Katona, M.S. Shur, R. Gaska, M. Shatalov, and A. Khan, “Deep ultraviolet light-emitting diodes”, *Phys. Status Solidi A*, vol. 203, pp. 1815–1818, 2006.
- [4] C. Pernot, M. Kim, S. Fukahori, T. Inazu, T. Fujita, Y. Nagasawa, A. Hirano, M. Ippommatsu, M. Iwaya, S. Kamiyama, I. Akasaki, and H. Amano, “Improved efficiency of 255–280 nm AlGa_N-based light-emitting diodes”, *Appl. Phys. Express*, vol. 3, pp. 061004-1–3, 2010.
- [5] T. Akasaka and T. Makimoto, “Flow-rate modulation epitaxy of wurtzite AlBN”, *Appl. Phys. Lett.*, vol. 88, pp. 041902-1–3, 2006.
- [6] A.Y. Polyakov, M. Shin, W. Qian, M. Skowronski, D.W. Greve, and R.G. Wilson, “Growth of AlBN solid solutions by organometallic vapor-phase epitaxy”, *J. Appl. Phys.*, vol. 81, pp. 1715–1719, 1997.
- [7] M. Kurimoto, T. Takano, J. Yamamoto, Y. Ishihara, M. Horie, M. Tsubamoto, and H. Kawanishi, “Growth of BGa_N/AlGa_N multi-quantum-well structure by metalorganic vapor phase epitaxy”, *J. Cryst. Growth*, vol. 221, pp. 378–381, 2000.
- [8] X. Li, S. Sundaram, Y.E. Gmili, T. Moudakir, F. Genty, S. Bouchoule, G. Patriarche, R.D. Dupuis, P.L. Voss, J.P. Salvestrini, and A. Ougazzaden, “BAIN thin layers for deep UV applications: BAIN thin layers for deep UV applications”, *Phys. Status Solidi A*, vol. 212, pp. 745–750, 2015.
- [9] T. Takano, M. Kurimoto, J. Yamamoto, and H. Kawanishi, “Epitaxial growth of high quality BAIGa_N quaternary lattice matched to AlN on 6H-SiC substrate by LP-MOVPE for deep-UV emission”, *J. Cryst. Growth*, vol. 237, pp. 972–977, 2002.
- [10] O. Rettig, “Investigation of AlBGa_N structures for UV-lighting”, *Annual Report 2016*, pp. 65–70, Ulm University, Institute of Optoelectronics.
- [11] K. Genji and T. Uchino, “Time-resolved photoluminescence characterization of oxygen-related defect centers in AlN”, *Appl. Phys. Lett.*, vol. 109, pp. 021113-1–5, 2016.
- [12] A. Nagakubo, H. Ogi, H. Sumiya, K. Kusakabe, and M. Hirao, “Elastic constants of cubic and wurtzite boron nitrides”, *Appl. Phys. Lett.*, vol. 102, pp. 241909-1–5, 2013.
- [13] S. Azzi, A. Zaoui, and M. Ferhat, “On the importance of the band gap bowing in boron-based III-V ternary alloys”, *Solid State Comms.*, vol. 144, pp. 245–248, 2007.
- [14] G. Cassabois, P. Valvin, and B. Gil, “Hexagonal boron nitride is an indirect bandgap semiconductor”, *Nature Photonics*, vol. 10, pp. 262–266, 2016.

Generation of Ultraviolet Laser Light by Frequency Tripling of a High-Power Infrared Optically Pumped Semiconductor Disk Laser

Markus Polanik and Jakob Hirlinger-Alexander

We present an ultraviolet (UV) laser with an output power exceeding 23 mW at an emission wavelength of 327 nm. The UV laser is realized by frequency tripling an infrared optically pumped semiconductor disk laser which is capable of an output power above 23 W at a wavelength of 982 nm. To access the UV wavelength regime, sum frequency generation of the frequency-doubled and the fundamental wavelength is utilized.

1. Introduction

The accessible wavelength range for optically pumped semiconductor disk lasers (OPSDLs) in the InGaAs/GaAs material system can cover a broad regime between 920 and 1180 nm. Utilizing different gain material like GaAlAs or GaInNAs extends the range to even shorter or longer emission wavelengths [1]. Since frequency doubling of the laser device is easily achievable by placing a nonlinear crystal inside the lasers cavity, semiconductor disk lasers grown on GaAs substrate can cover almost the entire visible wavelength spectrum. Adding a birefringent filter into the cavity allows to improve the second harmonic performance and to tune the emission wavelength by a few nanometers. Output powers with tens of watts in the visible range are possible by using second harmonic generation [2]. An ultraviolet emission can either be realized by tripling an infrared disk laser or by doubling an AlGaInP red laser [3, 4].

In order to generate ultraviolet light with an infrared laser it is necessary to frequency triple the laser's emission wavelength. Although it is possible to directly frequency triple the output light of a laser by taking advantage of the third-order nonlinearity, this process is quite uncommon due to the low conversion efficiency. A two-step process which involves mixing the fundamental infrared laser light with the frequency-doubled output of the laser can be far more efficient [5]. This approach can be realized with an optically pumped semiconductor disk laser by placing two nonlinear optical crystals inside the lasers cavity, one for the second-harmonic generation and the other one for the sum-frequency generation. Here, we utilize this two-step process to frequency-triple the output of an optically pumped semiconductor disk laser which is designed for a wavelength of 980 nm [6].

2. Layer Design and Characterization of the Disk Laser

The semiconductor disk lasers structure contains three key elements: A dielectric anti-reflection coating, a resonant periodic gain structure and a double-band Bragg reflector (DBBR). The gain region of the disk laser contains six InGaAs quantum wells which are placed in the anti-nodes of the standing electric field inside of the microresonator. The quantum wells have an indium concentration of 16.5%. Strain compensation is utilized by GaAsP layers. In order to provide a bottom mirror with a high reflectivity for the laser wavelength as well as for the pump wavelength, a numerically designed DBBR with 33 mirror pairs out of AlAs/Al_{0.19}Ga_{0.81}As is used [7]. The disk structure was designed for an emission wavelength of 980 nm and a pump wavelength of 808 nm. During the processing of the laser devices, the GaAs substrate will be completely removed, which requires growing the epitaxial structure in reverse order. The Bragg mirror is therefore the last layer sequence grown in the chamber of the molecular beam epitaxy machine. To further improve the performance of the barrier pumped laser device, a diamond heat spreader is used. The measured reflectivity spectra of a processed disk laser are shown in Fig. 1.

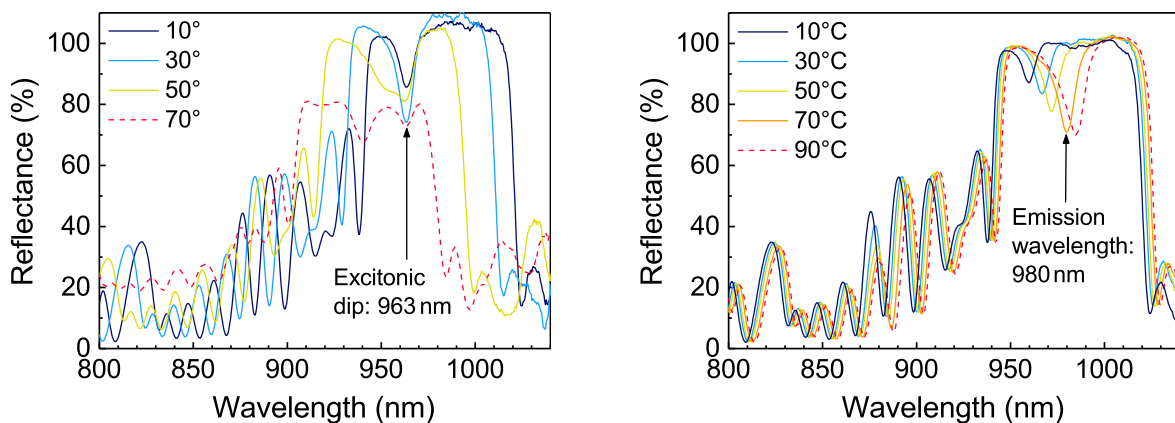


Fig. 1: Reflectivity spectra of a disk laser over the incidence angle at room temperature (left). The reflectivity spectra over the temperature (right) were taken at an angle of 10°.

From the angle-dependent reflectivity spectra, the excitonic resonance wavelength and a suitable pump angle can be determined. The excitonic dip is located at a wavelength of 963 nm, which is roughly 17 nm shorter than the emission wavelength of the laser device. A slightly greater distance between these two wavelengths would be favorable, since the gain spectrum will shift four to five times faster with increasing temperature than the resonance wavelength. One of the two stop bands of the DBBR is located between 945 and 1015 nm, while the other one lies between 800 and 830 nm. The position of the stop band for the pump wavelength can be determined by measuring the reflectivity spectra of the semiconductor disk lasers backside [7].

In a linear resonator with an outcoupling mirror reflectivity of 99.1% an optical output power of 23.3 W can be achieved with the optically pumped semiconductor disk laser. The heat sink of the laser device was cooled down to a temperature of -7.5°C . At higher

heat-sink temperatures a decline of the output power is noticeable. Nevertheless an output power beyond 17 W is still possible at a heat-sink temperature of 7.5 °C. The output characteristics of the disk laser measured at four different heat-sink temperatures is displayed in Fig. 2. A diode laser with an emission wavelength of 808 nm is used as a pump source. The spot size of the pump beam on the chip is $600 \times 550 \mu\text{m}^2$. An increase of the absorbed pump power leads to a linear shift of the emission wavelength of approximately 0.19 nm/W. The absorptance rate of the pump power during the four measurements at different heat-sink temperatures is between 89.8 and 97.8 %. It is noticeable that an increase of the chip temperature leads to a decline of the absorptance rate. This can be explained with an increasing reflectance of the semiconductor disk at the pump wavelength, due to the red-shift of the spectrum, for higher temperatures. A larger pump angle may solve this problem.

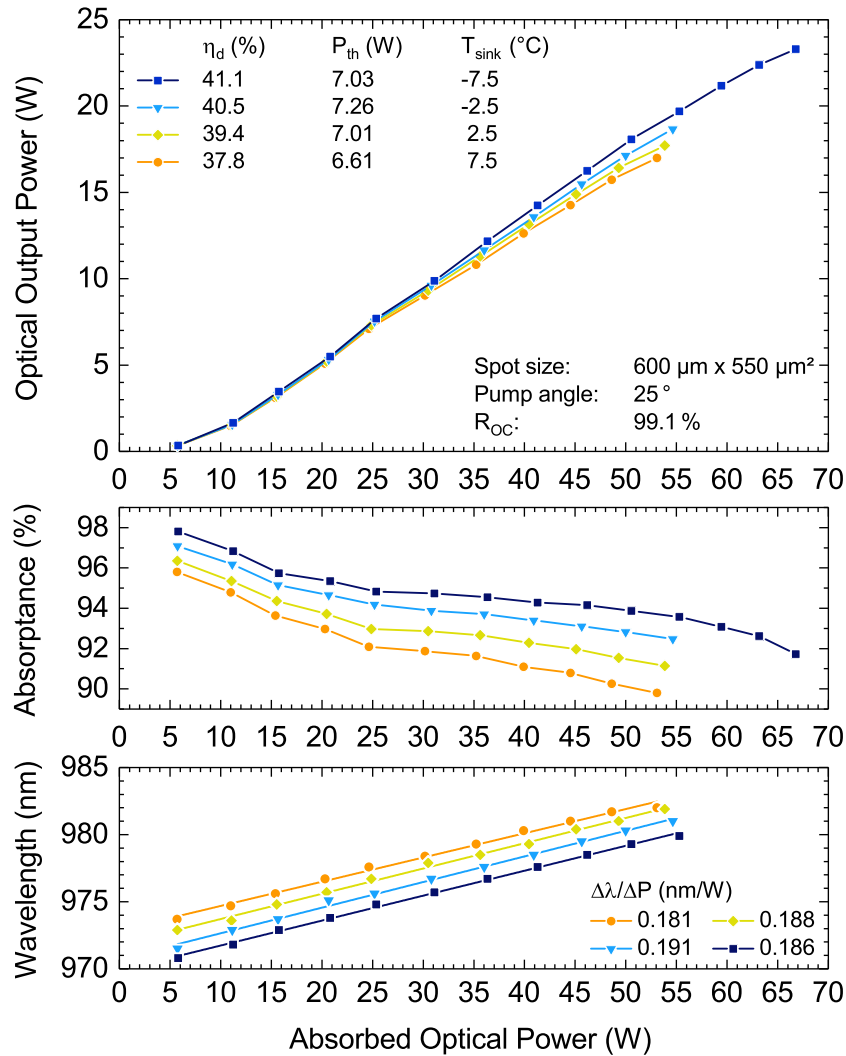


Fig. 2: Output characteristics of the used semiconductor disk laser in a linear resonator setup with an outcoupling mirror reflectivity of 99.1 %. The measurements were taken at four different temperatures of the heat sink.

3. Experimental Setup for Frequency Tripling

For the frequency tripling we used a double-folded resonator with three different mirrors, a birefringent filter and two nonlinear crystals for the second harmonic and sum-frequency generation. Both are lithium triborate (LBO) crystals and have $3 \times 3 \text{ mm}^2$ wide cross-sections. The crystal for the second-harmonic generation is 8 mm, the crystal for the sum-frequency generation 10 mm long. The thickness of the birefringent filter is 4 mm. A sketch of the experimental setup is shown in Fig. 3.

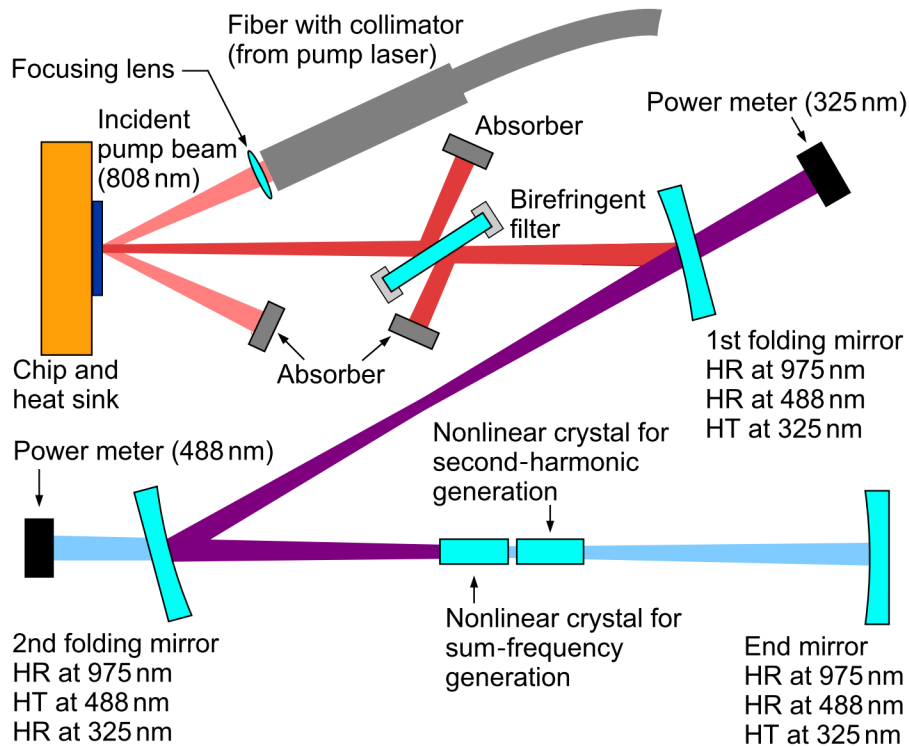


Fig. 3: Sketch of the experimental setup for frequency tripling the infrared laser. The ultraviolet light is coupled out at the first folding mirror and the frequency-doubled light is coupled out at second folding mirror. All resonator mirrors are highly reflective for infrared light.

The first mirror is the integrated Bragg mirror on the semiconductor chip. It is highly reflective for the pump and the fundamental wavelength. Due to the fact that the bandgap of GaAs at room temperature is 1.42 eV, which corresponds to a wavelength of 873.13 nm, the semiconductor disk is absorptive for the second and the third harmonic. To prevent the semiconductor structure from unnecessary heating, we couple the second and third harmonic beam out of the resonator before it can reach the chip. Therefore, we have two different coatings on the first and second folding mirror. The first folding mirror is transmissive for the third and highly reflective for the fundamental wavelength and the second harmonic. The second folding mirror is transmissive for the second and highly reflective for the fundamental wavelength and the third harmonic.

In order to narrow the spectral width and stabilize the emission wavelength the laser, a birefringent filter is placed in the first resonator arm. Although the filter is placed in the Brewster angle inside of the resonator, the filter still couples out a high amount of infrared light, which has to be blocked with suitable absorbers. The two nonlinear crystals are placed right next to each other in the beam waist of the last resonator arm, since high electric field strengths are beneficial to increase the efficiency of the nonlinear conversions. Placing the crystals directly next to each other has in addition the advantage that the influence of the walk-off angle between the first and the second harmonic in the SFG crystal, which is not avoidable with critical phase matching, is small. The standing wave in the laser resonator is a superposition of a forward and a backward traveling wave. As a result, the crystal for the second harmonic generation will also produce a forward and a backward traveling wave. In the crystal for the sum-frequency generation we want to have as much second harmonic electric field strength as possible, so we place the SHG crystal behind the SFG crystal and make the end mirror high reflective for the second harmonic. This positioning of the crystals has the big advantage that the second harmonic photons are traveling only in one direction through the SFG crystal (towards the semiconductor chip). Due to momentum conservation, the generated third harmonic has the same direction as the second harmonic. On the way back towards the chip, the second harmonic is coupled out at the second folding mirror and the third harmonic — the UV light we want to get — is coupled out at the first folding mirror. The captured beam profile of the ultraviolet laser beam and a picture of the experimental setup are shown in Fig. 4.

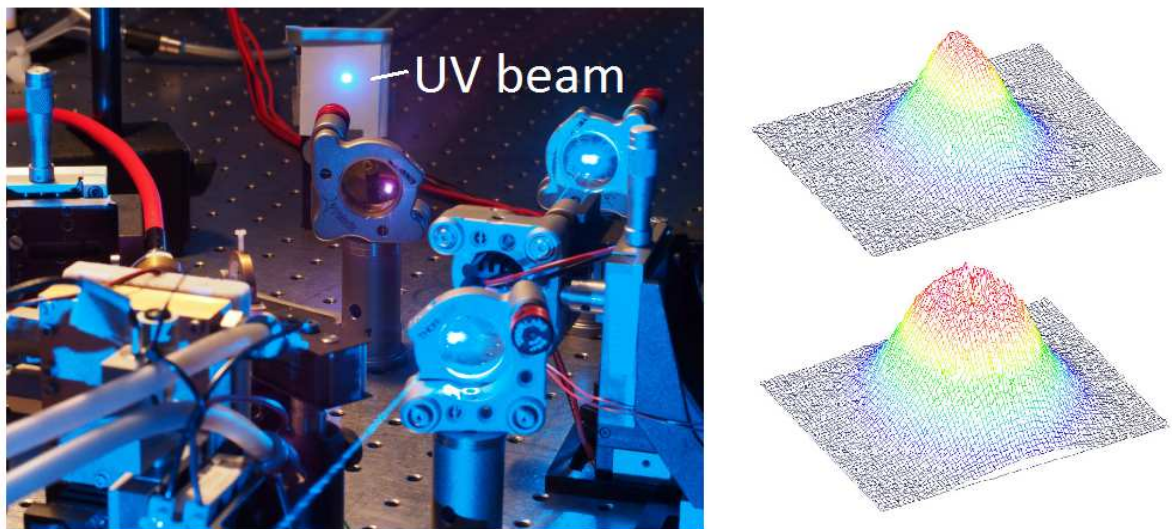


Fig. 4: Picture of the experimental setup (left). The ultraviolet laser beam is visible on a piece of paper due to fluorescence. A CMOS camera was used to measure the beam profile of the ultraviolet beam at a pump power of 10 W (top right) and 33 W (bottom right).

4. Output Characteristics of the Ultraviolet Laser

The experimental setup allows a tuning of the fundamental wavelength from 970 to 985 nm (full width at half maximum) with the birefringent filter. However, a significant drop in the ultraviolet output power takes place if the fundamental wavelength is detuned away from the adjusted wavelength. Tuning of the emission wavelength requires a realignment of the two nonlinear crystals due to the loss of the phase matching. Although the spectral width of the ultraviolet light could not be directly measured, it is expected to be 0.08 nm, since the spectral width of the fundamental wavelength is 0.24 nm at -3 dB clip level. Without a birefringent filter in the resonator, the spectral width of the fundamental emission at -3 dB is 2.4 nm wide. In our experiment, the fundamental wavelength of the laser of 982 nm leads to a second harmonic wavelength of 491 nm. The sum-frequency generation of the first and the second-harmonic results in a third-harmonic wavelength of 327 nm. In Fig. 5 the output characteristics of the second and the third harmonic are shown.

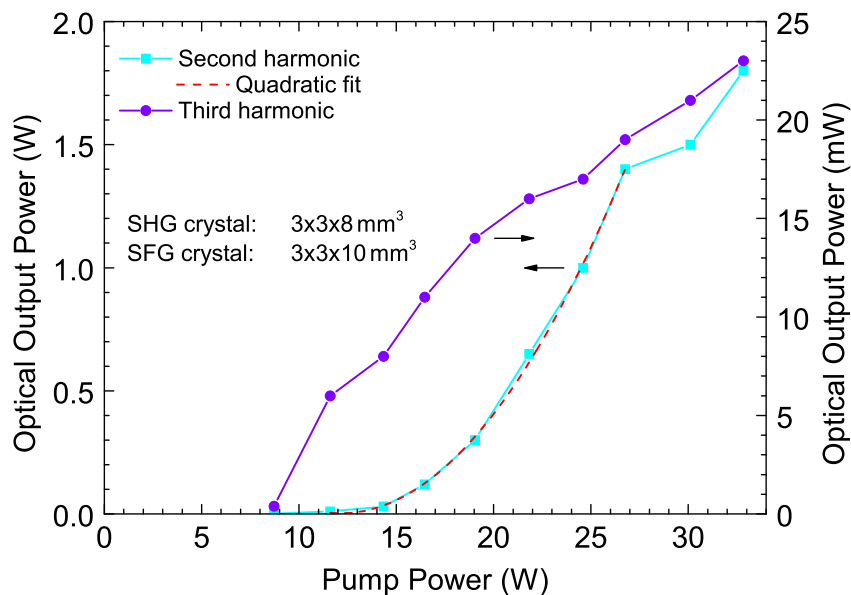


Fig. 5: Second and third harmonic output power. A quadratic fit of the second harmonic output power is possible for pump powers below 27 W.

The output power of the second harmonic rises from zero to 1.8 W when the pump power is raised from 8.7 to 32.8 W. A quadratic fit to the output curve could be applied for pump powers below 26.8 W. At higher pump powers a deviation from the quadratic fit is observed. The reason for this behavior is the temperature rise of the nonlinear crystal which leads to a phase mismatch with higher powers. With a second harmonic power of 1.8 W, the third harmonic output power reaches 23 mW.

The pump conversion efficiency is calculated as the ratio between the output power and the pump power. The results for the second and third harmonic are displayed in Fig. 6. For the second harmonic a nearly linear behavior for pump powers between 14.4 and 26.8 W is noticeable. This corresponds to the quadratic curve of the output power. An

explanation for this behavior is the proportionality of the second harmonic output to the square of the fundamental laser power. The fundamental power itself is proportional to the pump power. So the second harmonic output divided by the pump power must be linear.

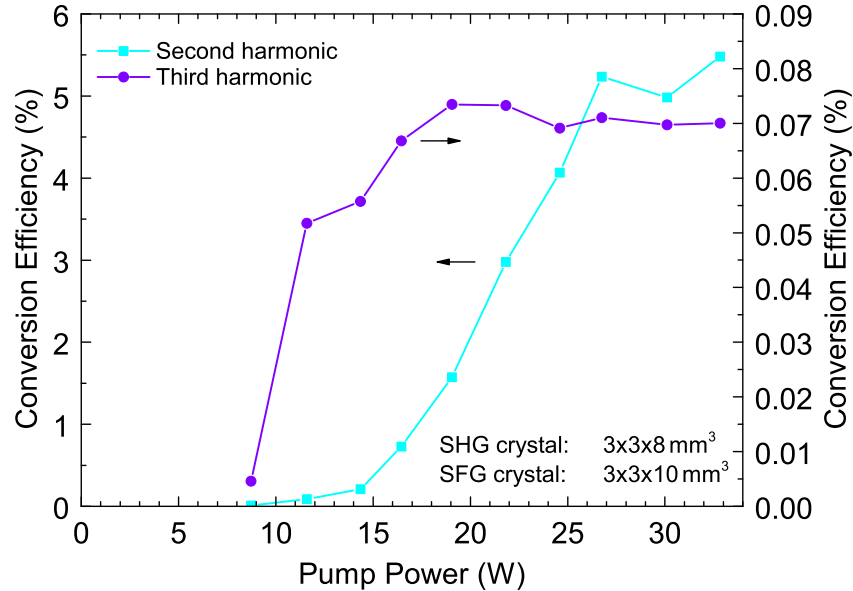


Fig. 6: Pump conversion efficiencies of the second and third harmonic of the laser from Fig. 5.

5. Conclusion

We demonstrated the output characteristics of an intra-cavity frequency-tripled infrared laser. Frequency tripling was achieved by mixing the fundamental wavelength of the semiconductor disk laser of 982 nm with the second harmonic. While it was possible to achieve an output power of more than 23 W at the fundamental wavelength of the laser, the double-folded resonator with two nonlinear crystals inside it only allowed a second-harmonic output power of 1.8 W. With a value beneath 6%, the conversion efficiency of the second harmonic is over three times lower than the anticipated efficiency from previous frequency doubling experiments [8]. Nevertheless, an ultraviolet output power of 23 mW at a wavelength of 327 nm was possible. Further improvements of the second-harmonic power should also increase the ultraviolet output, since the third harmonic generation highly depends on the second harmonic field strength in the sum-frequency generation crystal.

Acknowledgment

Prior work of Alexander Hein in planning and testing the frequency-tripling experiment is highly appreciated.

References

- [1] O.G. Okhotnikov, *Semiconductor Disk Lasers: Physics and Technology*, Weinheim: WILEY-VCH Verlag, 2009.
- [2] A. Rahimi-Iman, “Recent advances in VECSELs”, *J. Opt.*, vol. 18, pp. 093003-1–30, 2016.
- [3] J.E. Hastie, L.G. Morton, A.J. Kemp, M.D. Dawson, A.B. Krysa, and J.S. Roberts, “High power ultraviolet VECSEL through intra-cavity frequency-doubling in BBO”, in Proc. *20th IEEE International Semiconductor Laser Conf., ISLC*, pp. 109–110. Kohala Coast, HI, USA, Sep. 2006.
- [4] H. Kahle, R. Bek, M. Heldmaier, T. Schwarzbäck, M. Jetter, and P. Michler, “High optical output power in the UVA range of a frequency-doubled, strain-compensated AlGaInP-VECSEL”, *Appl. Phys. Express*, vol. 7, pp. 092705-1–4, 2014.
- [5] S.-N. Zhu, Y.-Y. Zhu, and N.-B. Ming, “Quasi-phase-matched third-harmonic generation in a quasi-periodic optical superlattice”, *Science*, vol. 278, pp. 843–846, 1997.
- [6] J. Hirlinger-Alexander, *Experimentelle Untersuchungen zur resonatorinternen Frequenzverdreifachung bei optisch gepumpten Halbleiterscheibenlasern*, Bachelor Thesis, Ulm University, Ulm, Germany, 2016.
- [7] F. Demaria, S. Lorch, S. Menzel, M.C. Riedl, F. Rinaldi, R. Rösch, and P. Unger, “Design of highly efficient high-power optically pumped semiconductor disk lasers”, *IEEE J. Select. Topics Quantum Electron.*, vol. 15, pp. 973–977, 2009.
- [8] A. Hein, “High-power green laser sources”, *Annual Report 2012*, pp. 3–10, Ulm University, Institute of Optoelectronics.

Ph.D. Thesis

1. Tobias Meisch,
*Untersuchungen von semipolarem (In)GaN auf strukturierten
Saphirsubstraten für effiziente grüne Leuchtdioden,*
April 2016.

Master Theses

1. Claudia Steinmann,
*Optimierung von Ohm-Kontakten bei HEMT-Transistoren
(mit Hilfe eines trockenchemischen Ätzprozesses),*
Sept. 2016.
2. Vignesh Devaki Murugesan,
*Quantum well photoluminescence under the influence
of externally applied electric field,*
Oct. 2016.
3. Jan-Patrick Scholz,
MOVPE-Wachstum und Charakterisierung von (BAlGa)N,
Dec. 2016.

Bachelor Theses

1. David Kern,
Untersuchung der Eigenschaften von oberflächengeätzten Vertikallaserdioden,
Jan. 2016.
2. Maximilian Johannes Spiess,
Optische Gassensorik mit oberflächennahen InGaN-Quantenfilmen,
Feb. 2016.
3. Shaohua Bian,
Optical backside-excitation of GaN-based chemical sensor structures,
May 2016.
4. Jakob Hirlinger-Alexander,
*Experimentelle Untersuchungen zur resonatorinternen Frequenzverdreifachung
bei optisch gepumpten Halbleiterscheibenlasern,*
July 2016.
5. Philipp Ackermann,
*Experimentelle Untersuchungen zur resonatorinternen Frequenzverdopplung
von quantenfilmgepumpten Halbleiterscheibenlasern,*
Dec. 2016.

Talks and Conference Contributions

- [1] S. Bader, P. Gerlach, and R. Michalzik, “VCSELs with optically controlled current confinement: experiments and analysis”, *SPIE Photonics Europe, Conf. on Semiconductor Lasers and Laser Dynamics VII*, Brussels, Belgium, Apr. 2016.
- [2] S. Bader, P. Gerlach, and R. Michalzik, “VCSELs with optically controlled current confinement”, *European VCSEL Day 2016*, Darmstadt, Germany, June 2016.
- [3] M. Caliebe, T. Meisch, F. Scholz, M. Hocker, and K. Thonke, “Investigations about parasitic n-type doping in semipolar GaN”, *International Workshop on Nitride Semiconductors, IWN2016*, Orlando, USA, Oct. 2016.
- [4] M. Daubenschütz and R. Michalzik, “Parameter extraction from temperature-dependent light–current–voltage data of vertical-cavity surface-emitting lasers”, *SPIE Photonics Europe, Conf. on Semiconductor Lasers and Laser Dynamics VII*, Brussels, Belgium, Apr. 2016.
- [5] M. Daubenschütz and R. Michalzik, “Thermal parameter extraction from continuous-wave light-current-voltage data of VCSELs”, *European VCSEL Day 2016*, Darmstadt, Germany, June 2016.
- [6] K.J. Ebeling, “25 years of VCSEL research and development at Ulm University and Philips Photonics”, *25th International Semiconductor Laser Conf., ISLC 2016*, Kobe, Japan, Sep. 2016.
- [7] D. Heinz, M.F. Schneidereit, V. Devaki Murugesan, S. Bian, L. Wu, F. Huber, B. Hörbrand, S. Chakraborty, Y. Wu, T. Weil, K. Thonke, and F. Scholz, “Sensing the iron-load of ferritin biomolecules using GaInN quantum wells as optochemical transducers”, *International Workshop on Nitride Semiconductors, IWN2016*, Orlando, USA, Oct. 2016.
- [8] D. Heinz, M.F. Schneidereit, M. Spiess, S. Bian, L. Wu, F. Scholz, F. Huber, B. Hörbrand, K. Thonke, S. Chakraborty, Y. Wu, and T. Weil, “Biosensorik mit Halbleiter-Heterostrukturen”, *BioRegio-Workshop*, Ulm, Germany, Oct. 2016.
- [9] D. Heinz, M.F. Schneidereit, S. Bian, L. Wu, F. Scholz, F. Huber, B. Hörbrand, K. Thonke, S. Chakraborty, Y. Wu, and T. Weil, “Biochemical sensing based on the photoluminescence response of polar GaInN quantum wells”, *Sensor-Workshop*, Duisburg, Germany, Dec. 2016.
- [10] T. Meisch, M. Caliebe, M. Hocker, K. Thonke, and F. Scholz, “Semipolar GaInN-GaN quantum well structures grown on patterned sapphire wafers”, *PolarCon*, Stuttgart, Germany, Feb. 2016.
- [11] T. Pusch, M. Bou Sanayeh, M. Lindemann, N.C. Gerhardt, M.R. Hofmann, and R. Michalzik, “Birefringence tuning of VCSELs”, poster at *SPIE Photonics Europe, Conf. on Semiconductor Lasers and Laser Dynamics VII*, Brussels, Belgium, Apr. 2016.

- [12] O. Rettig, J.-P. Scholz, S. Bauer, K. Thonke, Y. Li, H. Qi, J. Biskupek, U. Kaiser, and F. Scholz, “Investigation of AlBGaN structures for UV-lighting”, Georgia Institute of Technology, Metz, France, Mar. 2016
- [13] O. Rettig, J.P. Scholz, S. Bauer, F. Scholz, K. Thonke, H. Qi, Y. Li, J. Biskupek, and U. Kaiser, “Investigation of epitaxially grown AlBN layers on AlN templates”, *European Materials Research Society, EMRS2016*, Warsaw, Poland, Sep. 2016.
- [14] O. Rettig, J.P. Scholz, S. Bauer, H. Qi, Y. Li, J. Biskupek, U. Kaiser, F. Scholz, and K. Thonke, “Boron containing AlGa_N layers for UV lighting”, *International Workshop on Nitride Semiconductors, IWN2016*, Orlando, USA, Oct. 2016.
- [15] O. Rettig, J.P. Scholz, S. Bauer, H. Qi, Y. Li, J. Biskupek, U. Kaiser, F. Scholz, and K. Thonke, “Investigation of crystal properties of epitaxially grown AlBN layers with boron content in the lower percentage regime”, *31th DGKK Workshop Epitaxy of III/V Semiconductor*, Duisburg, Germany, Dec. 2016.
- [16] M.F. Schneidereit, D. Heinz, F. Huber, S. Chakraborty, T. Sandner, F. Scholz, K. Thonke, and T. Weil, “(In)Ga_N nanostructures for optical biosensing”, poster at *Doktoranden-unter-sich-Seminar*, Bad Herrenalb, Germany, Oct. 2016.
- [17] M.F. Schneidereit, D. Heinz, O. Rettig, F. Huber, B. Hörbrand, S. Chakraborty, N. Naskar, F. Scholz, K. Thonke, and T. Weil, “Optimisation of (In)Ga_N quantum wells for optical (bio)chemical sensing: numerical and experimental convergence”, *31th DGKK Workshop Epitaxy of III/V Semiconductor*, Duisburg, Germany, Dec. 2016.
- [18] N.C. Gerhardt, M. Lindemann, T. Pusch, R. Michalzik, and M.R. Hofmann, “Birefringent vertical-cavity surface-emitting lasers: toward high-speed spin-lasers” (invited), *SPIE Photonics Europe, Conf. on Semiconductor Lasers and Laser Dynamics VII*, Brussels, Belgium, Apr. 2016.
- [19] N.C. Gerhardt, M. Lindemann, T. Pusch, R. Michalzik, and M.R. Hofmann, “High-frequency operation of spin vertical-cavity surface-emitting lasers: towards 100 GHz” (invited), *SPIE Optics + Photonics 2016, Conf. on Spintronics IX*, San Diego, CA, USA, Aug./Sep. 2016.
- [20] M. Lindemann, N.C. Gerhardt, M.R. Hofmann, T. Pusch, and R. Michalzik, “Influence of birefringence splitting on ultrafast polarization oscillations in VCSELs”, *SPIE Photonics West 2016, Conf. on Vertical-Cavity Surface-Emitting Lasers XX*, San Francisco, CA, USA, Feb. 2016.
- [21] M. Lindemann, T. Pusch, R. Michalzik, N.C. Gerhardt, and M.R. Hofmann, “Frequency tuning of polarization oscillations in spin-polarized vertical-cavity surface-emitting lasers”, *SPIE Photonics Europe, Conf. on Semiconductor Lasers and Laser Dynamics VII*, Brussels, Belgium, Apr. 2016.

- [22] M. Lindemann, N.C. Gerhardt, M.R. Hofmann, T. Pusch, and R. Michalzik, “Frequency tuning of polarization oscillations in spin-lasers”, poster at *SPIE Optics + Photonics 2016*, Conf. on *Spintronics IX*, San Diego, CA, USA, Aug./Sep. 2016.

Publications

- [1] S. Bader, P. Gerlach, and R. Michalzik, “VCSELs with optically controlled current confinement: experiments and analysis”, in *Semiconductor Lasers and Laser Dynamics VII*, K.P. Panajotov, M. Sciamanna, A.A. Valle, R. Michalzik (Eds.), Proc. SPIE 9892, pp. 989208-1–6, 2016.
- [2] S. Bader, P. Gerlach, and R. Michalzik, “Optically controlled current confinement in vertical-cavity surface-emitting lasers”, *IEEE Photon. Technol. Lett.*, vol. 28, pp. 1309–1312, 2016.
- [3] S. Bader, P. Gerlach, and R. Michalzik, “Oxide-free vertical-cavity lasers with optically self-controlled current confinement”, *SPIE Newsroom*, Sep. 13, 2016, 3 pages, DOI:10.1117/2.1201608.006556.
- [4] M. Caliebe, S. Tandukar, Z. Cheng, M. Hocker, Y. Han, T. Meisch, D. Heinz, F. Huber, S. Bauer, A. Plettl, C. Humphreys, K. Thonke, and Ferdinand Scholz, “Influence of trench period and depth on {MOVPE} grown GaN on patterned r-plane sapphire substrates”, *J. Cryst. Growth*, vol. 440, pp. 69–75, 2016.
- [5] M. Caliebe, Y. Han, M. Hocker, T. Meisch, C. Humphreys, K. Thonke, and F. Scholz, “Growth and coalescence studies of (11 $\bar{2}$ 2) oriented GaN on pre-structured sapphire substrates using marker layers”, *Phys. Status Solidi B*, vol. 253, pp. 46–53, 2016,
- [6] M. Daubenschütz and R. Michalzik, “Parameter extraction from temperature-dependent light–current–voltage data of vertical-cavity surface-emitting lasers”, in *Semiconductor Lasers and Laser Dynamics VII*, K.P. Panajotov, M. Sciamanna, A.A. Valle, R. Michalzik (Eds.), Proc. SPIE 9892, pp. 98920R-1–8, 2016.
- [7] R.A.R. Leute, D. Heinz, J. Wang, T. Meisch, M. Müller, G. Schmidt, S. Metzner, P. Veit, F. Bertram, J. Christen, M. Martens, T. Wernicke, M. Kneissl, S. Jenisch, S. Strehle, O. Rettig, K. Thonke, and F. Scholz, “Embedded GaN nanostripes on c-sapphire for DFB lasers with semipolar quantum wells”, *Phys. Status Solidi B*, vol. 253, pp. 180–185, 2016.
- [8] T. Meisch, R. Zeller, S. Schörner, K. Thonke, L. Kirste, T. Fuchs, and Ferdinand Scholz, “Doping behavior of (11 $\bar{2}$ 2)-GaN grown on patterned sapphire substrates”, *Phys. Status Solidi B*, vol. 253, pp. 164–168, 2016.
- [9] T. Pusch, M. Bou Sanayeh, M. Lindemann, N.C. Gerhardt, M.R. Hofmann, and R. Michalzik, “Birefringence tuning of VCSELs”, in *Semiconductor Lasers and Laser Dynamics VII*, K.P. Panajotov, M. Sciamanna, A.A. Valle, R. Michalzik (Eds.), Proc. SPIE 9892, pp. 989222-1–6, 2016.
- [10] F. Scholz, J. Koch, A. Frey, and A.C. Jones, “Organometallic source materials for III-V epitaxy”, *Reference Module in Materials Science and Materials Engineering*, pp. 1–6, Oxford: Elsevier, 2016. ?

- [11] F. Scholz, M. Caliebe, G. Gahramanova, D. Heinz, M. Klein, R.A.R. Leute, T. Meisch, J. Wang, M. Hocker, and K. Thonke, “Semipolar GaN-based heterostructures on foreign substrates”, *Phys. Status Solidi B*, vol. 253, pp. 13–22, 2016.
- [12] F. Scholz, T. Meisch, and K. Elkhoully, “Efficiency studies on semipolar GaInN-GaN quantum well structures”, *Phys. Status Solidi A*, vol. 213, pp. 3117–3121, 2016.
- [13] J. Wang, T. Meisch, F. Scholz, D. Heinz, and R. Zeller, “Internal quantum efficiency and carrier injection efficiency of c-plane, $\{10\bar{1}1\}$ and $\{11\bar{2}2\}$ InGaN/GaN-based light emitting diodes”, *Phys. Status Solidi B*, vol. 253, pp. 174–179, 2016.
- [14] T. Aschenbrenner, M. Schowalter, T. Mehrstens, K.Müller-Caspary, M. Fikry, D. Heinz, I. Tischer, M. Madel, K. Thonke, D. Hommel, F. Scholz, and A. Rosenauer, “Composition analysis of coaxially grown InGaN multi quantum wells using scanning transmission electron microscopy”, *J. Appl. Phys.*, vol. 119, pp. 175701-1–6, 2016.
- [15] E.R. Buß, P. Horenburg, U. Rossow, H. Bremers, T. Meisch, M. Caliebe, F. Scholz, and A. Hangleiter, “Non- and semipolar AlInN one-dimensionally lattice-matched to GaN for realization of relaxed buffer layers for strain engineering in optically active GaN-based devices”, *Phys. Status Solidi B*, vol. 253, pp. 84–92, 2016.
- [16] B. Corbett, Z. Quan, D.V. Dinh, G. Kozlowski, D. O’Mahony, M. Akhter, S. Schulz, P. Parbrook, P. Maaskant, M. Caliebe, M. Hocker, K. Thonke, F. Scholz, M. Pristovsek, Y. Han, C.J. Humphreys, F. Brunner, M. Weyers, T.M. Meyer, and L. Lymperakis, “Development of semipolar (11-22) LEDs on GaN templates”, H. Jeon, L.-W. Tu, M.R. Krames, M. Strassburg (Eds.), Proc. SPIE 9768, pp. 97681G-1–9, 2016.
- [17] B. Corbett, L. Lymperakis, F. Scholz, C. Humphreys, F. Brunner, and T. Meyer, “Scalable semipolar gallium nitride templates for high-speed LEDs”, *SPIE News Room*, June 3, 2016, 3 pages, DOI: 10.1117/2.1201605.006482.
- [18] N.C. Gerhardt, M. Lindemann, T. Pusch, R. Michalzik, and M.R. Hofmann, “Birefringent vertical-cavity surface-emitting lasers: toward high-speed spin-lasers” (invited), in *Semiconductor Lasers and Laser Dynamics VII*, K.P. Panajotov, M. Sciamanna, A.A. Valle, R. Michalzik (Eds.), Proc. SPIE 9892, pp. 989206-1–9, 2016.
- [19] N.C. Gerhardt, M. Lindemann, T. Pusch, R. Michalzik, and M.R. Hofmann, “High-frequency operation of spin vertical-cavity surface-emitting lasers: towards 100 GHz” (invited), in *Spintronics IX*, H.-J. Drouhin, J.-E. Wegrowe, M. Razeghi (Eds.), Proc. SPIE 9931, pp. 99310C-1–6, 2016.
- [20] Y. Han, M. Caliebe, H. Frederik, Q. Ramasse, M. Pristovsek, T. Zhu, F. Scholz, and C. Humphreys, “Toward defect-free semi-polar GaN templates on pre-structured sapphire”, *Phys. Status Solidi B*, vol. 253, pp. 834–839, 2016.
- [21] C.R. Head, A. Hein, A.P. Turnbull, M. Polanik, E.A. Shaw, T. Chen Sverre, P. Unger, and A.C. Tropper, “High-order dispersion in sub-200-fs pulsed VECSELS”, in *Vertical External Cavity Surface Emitting Lasers (VECSELS) VI*, K.G. Wilcox (Ed.), Proc. SPIE 9734, pp. 973408-1–10, 2016.

- [22] M. Hocker, I. Tischer, B. Neuschl, K. Thonke, M. Caliebe, M. Klein, and F. Scholz, “Stacking fault emission in GaN: Influence of n-type doping”, *J. Appl. Phys.*, vol. 119, pp. 185703-1–6, 2016.
- [23] M. Hocker, P. Maier, L. Jerg, I. Tischer, G. Neusser, C. Kranz, M. Pristovsek, C.J. Humphreys, R.A.R. Leute, D. Heinz, O. Rettig, F. Scholz, and K. Thonke, “Determination of axial and lateral exciton diffusion length in GaN by electron energy dependent cathodoluminescence”, *J. Appl. Phys.*, vol. 120, pp. 085703-1–6, 2016.
- [24] M. Knab, M. Hocker, T. Felser, I. Tischer, J. Wang, F. Scholz, and K. Thonke, “EBIC investigations on polar and semipolar InGaN LED structures”, *Phys. Status Solidi B*, vol. 253, pp. 126–132, 2016.
- [25] T. Langer, M. Klisch, F.A. Ketzler, H. Jönen, H. Bremers, U. Rossow, T. Meisch, F. Scholz, and A. Hangleiter, “Radiative and nonradiative recombination mechanisms in nonpolar and semipolar GaInN/GaN quantum wells”, *Phys. Status Solidi B*, vol. 253, pp. 133–139, 2016.
- [26] M. Lindemann, T. Pusch, R. Michalzik, N.C. Gerhardt, and M.R. Hofmann, “Frequency tuning of polarization oscillations: toward high-speed spin-lasers”, *Appl. Phys. Lett.*, vol. 108, pp. 042404-1–4, 2016.
- [27] M. Lindemann, N.C. Gerhardt, M.R. Hofmann, T. Pusch, and R. Michalzik, “Influence of birefringence splitting on ultrafast polarization oscillations in VCSELs”, in *Vertical-Cavity Surface-Emitting Lasers XX*, K.D. Choquette, J.K. Guenter (Eds.), Proc. SPIE 9766, pp. 97660L-1–7, 2016.
- [28] M. Lindemann, T. Pusch, R. Michalzik, N.C. Gerhardt, and M.R. Hofmann, “Frequency tuning of polarization oscillations in spin-polarized vertical-cavity surface-emitting lasers”, in *Semiconductor Lasers and Laser Dynamics VII*, K.P. Panajotov, M. Sciamanna, A.A. Valle, R. Michalzik (Eds.), Proc. SPIE 9892, pp. 989224-1–5, 2016.
- [29] M. Lindemann, N.C. Gerhardt, M.R. Hofmann, T. Pusch, and R. Michalzik, “Frequency tuning of polarization oscillations in spin-lasers”, in *Spintronics IX*, H.-J. Drouhin, J.-E. Wegrowe, M. Razeghi (Eds.), Proc. SPIE 9931, pp. 993149-1–6, 2016.
- [30] S. Metzner, F. Bertram, T. Hempel, T. Meisch, S. Schwaiger, F. Scholz, and J. Christen, “Direct microscopic correlation of real structure and optical properties of semipolar GaN on pre-patterned r-plane sapphire”, *Phys. Status Solidi B*, vol. 253, pp. 54–60, 2016.
- [31] M. Müller, G. Schmidt, S. Metzner, P. Veit, F. Bertram, R.A.R. Leute, D. Heinz, J. Wang, T. Meisch, F. Scholz, and J. Christen, “Nanoscale cathodoluminescence imaging of III-nitride-based LEDs with semipolar quantum wells in a scanning transmission electron microscope”, *Phys. Status Solidi B*, vol. 253, pp. 112–117, 2016.

- [32] Z. Quan, Q. Dinh, D.V. Dinh, S. Presa, B. Roycroft, A. Foley M. Akhter, D. O'Mahony, P.P. Maaskant, M. Caliebe, F. Scholz, P.J.J. Parbrook, and B. Corbett, "High Bandwidth Freestanding Semipolar (11-22) InGaN Light Emitting Diodes", *IEEE Photonics J.*, vol. 8, pp. 1601808-1–8, 2016.



ulm university universität
uulm

Ulm University
Institute of Optoelectronics
Albert-Einstein-Allee 45
89081 Ulm | Germany